# THE USE OF GEOSTATIONARY SATELLITE BASED RAINFALL ESTIMATION AND RAINFALL-RUNOFF MODELLING FOR REGIONAL FLASH FLOOD ASSESSMENT

Dwi Prabowo Yuga Suseno

Hokkaido University

2013

# THE USE OF GEOSTATIONARY SATELLITE BASED RAINFALL ESTIMATION AND RAINFALL-RUNOFF MODELLING FOR REGIONAL FLASH FLOOD ASSESSMENT

**[**静止衛星による観測データを用いた降雨推定手法と降雨流出モデルによる山地流域における突発的出水評価**]**


Dwi Prabowo Yuga Suseno

スセノ　ドウィ　プラボウォ　ユガ

*River and Watershed Engineering Laboratory*

Faculty of Engineering

Hokkaido University


A dissertation submitted to the Graduate School of Engineering of the Hokkaido University in partial fulfillment of the requirements for the degree of Doctor of Engineering

August 2013

*…Kaaturaken kagem swargi Bpk Mulyono & Ibu Sugini…*

اللهم اغفر لهم وارحمهم وعافهم واعف عنهم

*(Dedicated to my late father and mother)*

# ABSTRACT

The availability of rainfall triggered hazard information such as flash flood is crucial in the flood disaster management and mitigation. However, providing that information is mainly hampered by the shortage of data because of the sparse, uneven or absence the hydrological or meteorological observation. Remote sensing techniques that make frequent observations with continuous spatial coverage provide useful information for detecting the hydrometeorological phenomena such as rainfall and floods. This study aims to develop and evaluate geostationary satellite based rainfall estimation by considering cloud types and atmospheric environmental conditions. Furthermore, the satellite rainfall estimation is coupled with rainfall-runoff model for regional flash flood assessment.

First, a simple rainfall estimation method using geostationary satellite i.e. Multi-functional Transport Satellite (MTSAT) blended with Tropical Rainfall Measuring Mission (TRMM) 2A12 is performed for Java Island, Indonesia and its surrounding area. The blending process is conducted by developing statistical relationship between cloud top temperature from MTSAT 10.8μm channel ($T_{IR1}$) which is collocated with rainfall rate (RR) acquired by TRMM 2A12. Inter comparison with TRMM Multi Precipitation Analysis (TMPA) data product is conducted. Temporal validation result shows that TMPA demonstrated better statistical performance than TIR1 and RR statistical relationship model. However for the spatial correlation, $T_{IR1}$ and RR statistical relationship model shows reasonably better performance than TMPA.

Second, the rainfall estimation method basically uses an assumption the lower cloud top temperature is associated with heavier rainfall, particularly for convective cloud type. To fulfill such assumption, the statistical relationship is developed mainly for cumulonimbus (Cb) cloud type. A new two-dimensional threshold diagram (2D-THR) has been developed based on maximum likelihood cloud classification results, which can readily be applied for MTSAT split window datasets. The study area is Japan and its surrounding area. By integrating the cloud type classification especially by separating Cb cloud type from other cloud types can improve the TIR1 and RR statistical relationship, which is indicated by increasing correlation coefficient and the gradient of regression line. Therefore, underestimating rainfall intensity can be avoided by applying rainfall rate and cloud top temperature relationship that uses Cb cloud type only rather than using all cloud types. A good agreement between estimated and measured storm rainfall also has been demonstrated when use this approach.

The geostationary satellite based rainfall estimation then applied for characterizing the storm severity. The Hosking-Wallis Regional Frequency Analysis (HW-RFA) method is used to

define the frequency distribution of long-term hourly maximum rainfall over Hokkaido Island. HW-RFA indicates that Generalized Normal/Log Normal three parameters (GNO/LN3) is suitable to describe the frequency distribution of long-term hourly maximum rainfall over Hokkaido Island. A return period map during heavy rainfall event is generated by using MTSAT based rainfall estimation, based on the GNO/LN3 distribution. A comparison with AMeDAS return period of the same rainfall even demonstrates that that the return period information shown by MTSAT rainfall is comparable with AMeDAS rainfall return period. For assessing the return period of an extreme event in the area that observed rainfall is lacking, the use of geostationary satellite based is proved useful to overcome such problem.

Third, total Precipitable Water Vapor (PWV) as a product of Global Positioning System observation and atmospheric vertical instability were considered to represent the atmospheric environmental conditions during the development of TIR1 and RR statistical models. The results demonstrated that the models that considered the combination of total PWV and atmospheric vertical instability were relatively more sensitive to heavy rainfall than were the models that considered no atmospheric environmental conditions. Intercomparison results with the TRMM 3B42 rainfall estimation product confirmed that MTSAT-based rainfall estimations made by considering atmospheric environmental conditions were more accurate for estimating rainfall generated by Cb cloud.

Lastly, a regional flash flood assessment is conducted based on two rainfall-runoff models: (i) empirical regression model approach and (ii) physical based approach using land surface model. The empirical model uses the multiple regression approach to draw a relationship between the flash flood severity and hydrological, morphometrical and meteorological conditions. Particularly for flash flood severity related to hydrological condition the statistical relationship is strongly determined by initial soil moisture condition. The resulted empirical models shows that flash flood severity as the function of morphometrical factors can provide flash flood potential information. Moreover, flash flood severity as the function of hydrological and meteorological factors demonstrate more dynamic pattern since they are related to rainfall intensity distribution. The physical based approach for flash flood assessment had been conducted by implementing river flow simulation the minimal advance treatments of surface interaction and runoff (MATSIRO). The result indicates that the river flow simulated by MTSAT downscaled with relatively sparse rainfall observation is comparable with the river flow simulation using more dense rain observation network.

# 静止衛星による観測データを用いた降雨推定手法と降雨流出モデルによる山地流域における突発的出水評価

突発的出水をもたらす豪雨の早期探知は洪水による被害を低減させる上で不可欠であるが,山地流域では現地観測データが乏しいという現状にある．これに対してリモートセンシング技術の利用は高い時空間解像度での観測を可能とし，降雨流出機構を解明及び予測する上で有用な手段となり得る．本研究は静止衛星による観測データを用いた雲分類手法と大気の環境場を考慮した降雨強度推定手法を提案し，得られた降雨データと降雨流出モデルを併せた山地流域における突発的出水の危険度の評価を実施するものである．

まずMTSAT(Multi-functional Transport Satellite)と同じく人工衛星であるTRMM(Tropical Rainfall Measuring Mission) 2A12の観測データによる降雨強度の推定精度の評価をインドネシアのJava島と周辺地域を対象に実施した．ここで使用される降雨強度推定手法はMTSATによって観測される10.8μmの近赤外放射データが示す雲頂温度とTRMMによる降雨強度(TMPA; TRMM Multi Precipitation Analysis)の統計的関係を用いるものである．得られた結果の妥当性として，MTSATによる雲頂温度情報に基づく降雨データはTMPAと同程度の精度を有することがわかった．

豪雨は一般に雲頂高度が高くその温度が低い積乱雲によってもたらされる．そこで積乱雲に特化し，積乱雲のみの雲頂温度と降雨量の統計的関係から新たに降雨強度を推定する手法を開発した．積乱雲の抽出にはMTSATにより観測される2つの異なる波長帯を使用し，split window法と最尤法を組み合わせることによって雲分類ダイアグラムを作成し，積乱雲の抽出を可能とした．本手法によって抽出された積乱雲の雲頂温度と降雨量との統計的関係はすべての雲を扱った場合の統計的関係よりも高い相関を示すことが確認された．また，得られた降雨データを現地観測データと比較したところ高い一致が見られた．

上記で開発した積乱雲に特化した降雨強度推定手法を用いて豪雨の発生確率年の評価を行った．ここで使用したのはHosking & Wallisによって提案されているHW-RFA (Hosking and Wallis Regional Frequency Analysis)である.同手法を北海道に適用し，年最大時間降雨強度に着目した発生確率年評価を実施したところ，著者によって作成された降雨データとAMeDAS (Automated Meteorological Data Acquisition System)降雨データによる豪雨の発生確率年の空間分布は類似するものであった．この結果は現地観測データの乏しい流域において高い時空間スケールで豪雨の確率年評価が議論可能であり，その入力値として著者が開発した降雨強度推定手法による降雨データが有用であることを示すものである．

次に降雨強度の推定に関し，雲頂温度に加えGPS (Global Positioning System)観測によって得られる可降水量と領域気象モデルによる大気の鉛直不安定度の効果を加味した降雨強度推定手法を新たに開発した．その結果,可降水量と鉛直不安定度の大きさは豪雨を捉える上で不可欠な要素であり，雲頂温度に加えこれら2項目を考慮することによって，より高い精度で豪雨の検知が可能であることがTRMM (3B42)降雨データとの比較によって示された．

最後に著者によって開発された降雨強度推定手法を降雨流出モデルに適用することで山地流域を対象とした突発的出水の危険度の評価を実施した．降雨流出モデルは(i)水文，気象，地形等の流域特性により構成される経験的モデルと(ii)陸面過程モデルの2種類を対象とした．降雨イベントごとに総降雨量と損失雨量関係に着目した分析を行ったところ，突発的出水の危険度は流域が降雨直前に飽和状態に近い場合であれば地形特性によって説明されやすいとの結果が得られた．一方，水文気象要素によって決定される突発的出水危険度は降雨パターンに依存するため動的に振る舞う特徴を有する．一方，陸面過程モデルを用いた物理的アプローチに関しては植生による蒸発散やグリッド内の地形特性を考慮したMATSIRO (Minimal Advanced Treatments of Surface Interaction and RunOff)を石狩川流域に適用できるように修正し，利用可能とした．その結果，本研究において提案した降雨強度推定手法による降雨データをMATSIROに与えることで得られるピーク流量は現地観測による降雨データを使用した場合と高い一致が見られた.以上より，本研究は現地観測データの乏しい流域における突発的出水の評価を行う上でリモートセンシング技術の多角的及び高度利用の有用性を示した．

# ACKNOWLEGMENTS

Praise be to Allah SWT, the Cherisher and Sustainer of the Worlds.

I owe my deepest gratitude to many persons, who support me from the very beginning of my study. Since it is difficult to memorize all of them, I would like to apologize to any persons, I forget to mention.

First, I would like to express my deepest and sincere gratitude to my supervisor, Associate Prof. Dr. Tomohito J. Yamada for his supports, guidance and encouragements through out my study. I wish to express my sincere gratitude Prof. Norihiro Izumi as my co-supervisor and head of River and Watershed Engineering Laboratory (RWE Lab) for providing an opportunity to this study. I am also indebted to Dr. Hiroshi Hayasaka who gives me chance to study in Hokkaido University. I extend my sincere thanks to Prof. Takafumi Sugiyama, Prof. Yasuyuki Shimizu, Prof. Toshihiko Yamashita, Prof. Hiroyuki Tanaka, Prof. Hiroshi Yokota, Prof. Shunji Kanie, Prof. Toru Tamura, Prof. Takashi Nakatsuji, Dr. Ichiro Kimura and Dr. Yasunori Watanabe as the committee member. My appreciation goes to Dr. Yadu Pokhrel, Dr. Suichi Kure for their kind attentions and supports for my study.

I would like to express my sincere thanks for Ministry of Forestry Republic of Indonesia (my employee), particularly Watershed Management Office of Indragiri Rokan at Pekanbaru, Riau, that give me permission to pursue my doctoral degree. I indebted to some Geography Faculty members at Gadjah Mada University, Yogyakarta, Indonesia (Prof. Dr. Hartono, DESS, Dr. Projo Danudoro, M.Sc, Prof. Dr. Junun Sartohadi, M.Sc, Dr. Pramono Hadi, M.Sc, Dr. Suharyadi, M.Sc) and the Faculty of Geoinformation Science and Earth Observation members, University of Twente, Enschede, The Netherlands (Dr. Ben Maathuis, Dr. Christ Mannaerts).

My sincere gratitude goes to E3 (Dr. Werawan Menakul, Mifue Shimamura), International Affairs Office of Engineering member (Yuki Tsuji, Kyoko Kawamura), RWE Lab Secretary (Sayo Uyama, Numata Nozomi).

I extend my sincere thank for Ministry of Education, Culture, Sports, Science and Technology (MEXT) for financial support. My study also partially supported by the Research Program on Climate Change Adaptation, Ministry of Education, Culture, Sports, Science and Technology, Japan (RECCA/MEXT), the MEXT SOUSEI program (theme C-i-C) the Integrated Study Project on Hydro-Meteorological Prediction and Adaptation to Climate Change in Thailand (IMPAC-T), the Science and Technology Research Partnership for Sustainable Development, the JST-JICA, Japan and Core Research for Evolutional Science and Technology program (CREST/JST). My sincere thank goes to Hitachi Zosen Corporation for providing an immense number of reliable datasets of GPS precipitable water.

I am grateful to the past and present RWE Lab members: Takuya Wada, Yuta Nakayama, Junya Nagahara, Yoshihiro Hata, Aoki Akinori, Kouki Wachi, Dr. Atinkut, Daham, Hossein, Takenori Kouno, Jun Sasaki, Yamahara Kouki, Dr. Adriano, Intan, Shenouda, Jeramee, Haruka Kuse, Kensuke Naito, Takahiro Ohyama, Kazunori Takahashi, Taiki Fukushima, Watanabe Yamato, Aiko Tokugawa, Yoshikazu Kitano, Daisuke Kamada, Jahir Uddin, Dr. Murad Farukh.

My sincere thanks go to all Indonesian students and families who live in Sapporo city, for their friendliness and hospitality. I am sorry not to mention you by name; however I have to express my special thanks to Eko Siswoyo and Dr. Erianto Indra Putra who help me to open my way to study in Hokudai.

I would like to extent my sincere gratitude to my parents in law, my brothers and sister (Mas Bambang, Widi, Catur), my brothers and sisters in law (Mas Yudhi, Mbak Lela, Mbak Sri, Mas Nano, Mas Pram, Mbak Hesti, Mas Puja, Mbak Nining) for your constant support and *do'a*.

Last but not least, my sincerely grateful for my wife Endar for your patience, encouragement, trust and most of all your love. You leave your job for accompany and support me in Sapporo, I really appreciate it. My sincere thank also goes to my lovely daughters Assyifa and Harumi. I am very proud of both of you.

Dwi Prabowo Yuga Suseno

# TABLE OF CONTENTS

# LIST OF FIGURES

# LIST OF TABLES

# Chapter 1. GENERAL INTRODUCTION

## 1.1. BACKGROUND

Flash flood is a flood that characterized by very rapid rising and falling with little or no advance warning (NRC, 2005). This type of flood differs with the "ordinary" flood since it occurred when the river receives more water than it can handle, causing inundation of normally dry area. The term "flash" is related to the rapid response to the causative event or rapid time to peak i.e. the time need for water level of the river to reach the crest. The definition of rapid response time is the varying among researcher, however the acceptable maximum response time may be between maximum 6 up to 12 hours after the causative event (Geogarkakos, 1986; NRC, 2005; Hapuarachchi, 2011). Flash flood may occur due to intense rainfall over a relatively small area or by the sudden release of water such as dam breach or glacier outburst. Nevertheless, this study only focuses on the flash flood caused by excessive rainfall in natural catchments.

Even though high intensity rainfall is the main triggering factor, the flash flood also can be considered as hydrometeorological event i.e. the even that depends on both hydrological and meteorological factor (Doswell, 1993). The hydrological factors that influence flash flood include terrain slope, land use, vegetation and soil type. Moreover, the flash flood is also controlled by hydraulic processes at the river channel or stream subject to flooding (NRC, 2003). The hydraulic process is related to the basin scale relationship between channel morphology with flood response.

Flash floods are considered as convective rainfall triggered event that producing the most fatalities (Doswell, 2006). The early warning system has been being developed for improving preparedness for the catchments that prone to flash floods. The recent efforts include the use of flash flood warning based on rainfall threshold and soil moisture condition (Norbiato et al., 2008), and the use of ensemble hydro-meteorological simulation (Alfieri et al., 2012). Other researchers were trying to develop a method to provide more preventive flash flood information by assessing the area that vulnerable to flash flood (Yousef et al., 2010, Dawod et al., 2011, Kim and Choi, 2011; 2012). This approach is mostly suitable in term of infrastructure and land use planning.

The use of rainfall runoff model for estimating flash flood needs high quality of rainfall data as the input. The ideal way is to develop dense rain gauge network which is can show the temporal and spatial pattern in catchment scale. World Meteorological Organization (WMO) suggests inter-station spacing distance about 25 – 30 km for flat areas and about half of such distance for mountainous area (Haile, 2011). Since such requirement is difficult to fulfill in practice, mostly due to limitation of fund and accessibility, the use of rainfall radar is often used.

However the use of radar is considerably too expensive. Other problem of using radar is due to blocking signal especially in mountainous region.

Considering some problems of providing rainfall information for the region that lack of rainfall observation or even ungauged, the use of remote sensing shows a promising alternative. Levizani et al. (2002) and Kidd et al. (2011) presented a review of current status of rainfall retrieval from satellite. The review shows that many applications have been able to directly use satellite based rainfall estimation such as hydrological and water cycle, precipitation process studies, snowfall application and climate studies. As stated by Kidd et al. (2011), particularly for hydrological and water resources application, the effective use of satellite based rainfall estimation is very much dependent upon the type of application, the accuracy, spatial resolution, and latency of the estimates: different application have different data requirement. This may be one of the reasons, why satellite based rainfall estimations as well as their application is still ongoing in order to meet various demands.

This study is motivated by the difficulties for providing water related information particularly in the operational level; due to the scarcity of rainfall observation. In a certain case the use of satellite based rainfall estimation is the only source of rainfall data when the observational instrument is damaged because of the hazard. This study is attempt to develop a methodological framework by using geostationary satellite, especially Multi-functional Transport Satellite (MTSAT) is for convective rainfall estimation and combining it with ancillary information such as the cloud type and atmospheric environmental condition that sustain the convective process. Since the geostationary satellite based rainfall estimation is still rarely applied for flash flood study, this research try to couple the satellite based rainfall estimation with rainfall runoff model to characterize the severity of flash flood.

## 1.2. RESEARCH OBJECTIVES

The objective of this study is to develop and evaluate geostationary satellite based rainfall estimation by considering cloud types and atmospheric environmental condition and to combine it with rainfall-runoff model for regional flash flood assessment. Since the geostationary satellite provides the images about 5 km spatial resolution, it is not reasonable to provide very detail or local rainfall estimation, therefore the term of ‘regional’ is used. The term ‘flash flood assessment’ suggests that in this research the severity of flash flood are estimated and evaluated using satellite based rainfall estimation combined with rainfall-runoff model. The specific objectives of the study are:

1. To develop and evaluate the geostationary satellite based rainfall estimation by considering not only cloud top temperature but also cloud type (i.e. Cb cloud type) and atmospheric environmental conditions sustaining the convective cloud development (i.e. precipitable water vapor and atmospheric vertical instability).
2. To characterize rainfall severity using geostationary based rainfall estimation through regional frequency analysis of long-term histrorical maximum rainfall.
3. To develop and evaluate a statistical empirical model of flash flood severity as a function of hydrolocigal, morphometrical and meteorological condition of the catchments. The meteorological condition is represented by the geostationary satellite based rainfall estimation.
4. To evaluate the performance of the geostationary satellite based rainfall estimation compared with the other sources of rainfall as the forcing for flash flood simulation using land surface model.

## 1.3. STRUCTURE OF THE DISSERTATION

This dissertation comprises of 8 chapters which are outlined in Figure 1.1. In **Chapter 1,** the background of the research is presented. In this chapter, the research objectives are also stated.

In **Chapter 2,** the basic approach and assumption of geostationary satellite based rainfall estimation is introduced. Here the statistical relationship that is generated from collocated MTSAT IR1 cloud top temperature ($T_{IR1}$) and rainfall rate (RR) from TRMM 2A12 is applied and validated. The study is conducted in Java Island Indonesia.

In **Chapter 3,** the cloud type classification is developed for supporting the assumption of $T_{IR1}$ and RR based rainfall estimation which is the method is suitable only for cumulonimbus (Cb) cloud type. A new two-dimensional threshold diagram (2D-THR) has been developed based on maximum likelihood cloud classification results, which can readily be applied for Multi-functional Transport Satellite (MTSAT) split window datasets. The Cb cloud type derived from the classification is used for improving $T_{IR1}$ and RR based rainfall estimation.

In **Chapter 4**, the MTSAT based rainfall estimation by considering Cb cloud type is applied to characterize the storm severity. The Hosking and Wallis regional frequency analysis (HW-RFA) method is used to define the frequency distribution of long-term hourly maximum rainfall over Hokkaido Island. Characterization of severity of 24 August 2010 storm event has been performed over western part of Hokkaido Island, based on the regional frequency distribution and the MTSAT rainfall estimation.

In **Chapter 5**, more detail process of rainfall estimation by using MTSAT image is investigated. The atmospheric environmental conditions i.e. total precipitable water vapor (PWV) and atmospheric vertical instability are considered during the development of statistical models. Validations were performed by comparing the estimated values with the observed rainfall derived from the AMeDAS rain gauge network and the Tropical Rainfall Measuring Mission (TRMM) 3B42 rainfall estimation product.

In **Chapter 6** and **Chapter 7** the MTSAT based rainfall estimation is applied to assess the flash flood severity and magnitude by using two approaches of rainfall-runoff model i.e. empirical regression and physical based approach respectively. **Chapter 6** presents a multiple regression analysis to draw the relationship between flash flood severity and hydro-morpho-meteorological factors. **Chapter 7** demonstrates the use of physical based land surface model namely MATSIRO to simulate river flow for peak discharge estimation using MTSAT rainfall estimation driven data.

In **Chapter 8**, the main findings are summarized. The conclusions and recommendations are presented in this chapter.

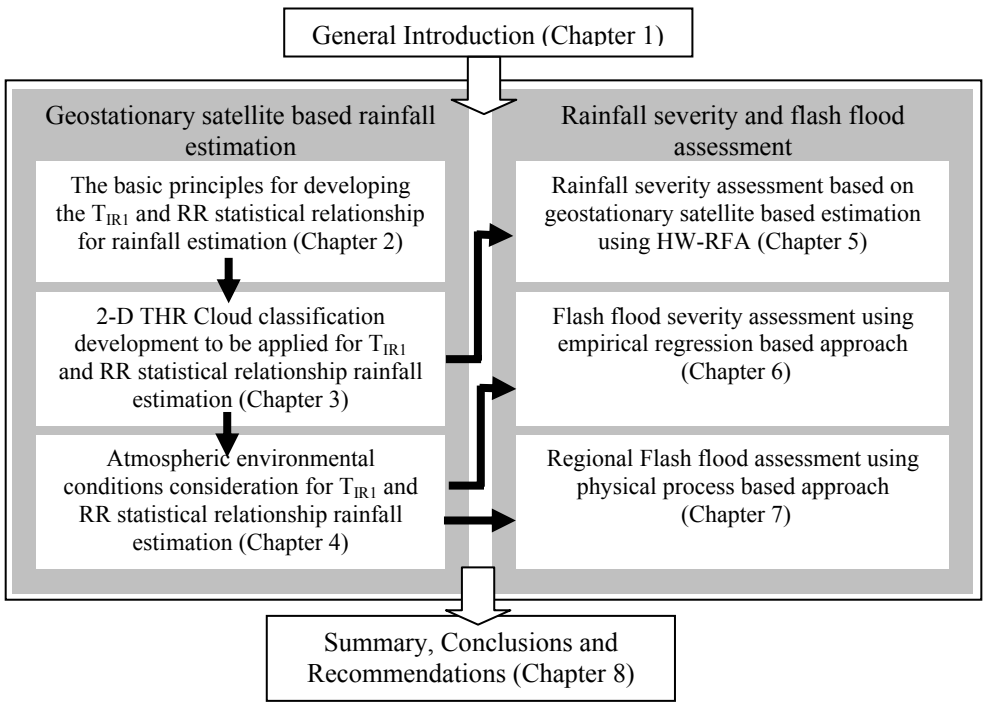


**Figure 1.1.** *Outline of the dissertation.*

# Chapter 2. GEOSTATIONARY SATELLITE BASED RAINFALL ESTIMATION AND VALIDATION

---

This chapter is based on: Suseno, Dwi Prabowo Yuga, T. J. Yamada, 2011, **Geostationary Satellite Based Rainfall Estimation and Validation: A Case Study of Java Island, Indonesia**, Journal of Japan Society of Civil Engineers, Ser. B1 (Hydraulic Engineering), Volume 67, Issue 4, pp. I_43-I_48

## Abstract

Near real time rainfall information is necessary for early warning of rainfall triggered hazard such as floods and landslides. Remote sensing based rainfall estimation has been considered to be used to fulfill that purpose. This study is addressed to use geostationary based rainfall estimation by using Multi Transport Satellite (MTSAT) data which is blended with Tropical Rainfall Measuring Mission (TRMM) 2A12 datasets in order to provide near real time rainfall information, especially for hazard study purposes over Java Island, Indonesia. The blending process is conducted by developing statistical relationship between cloud top temperature from MTSAT 10.8µm channel ($T_{IR1}$) which is collocated with rainfall rate (RR) acquired by TRMM 2A12. Comparison to TRMM Multi Precipitation Analysis (TMPA) datasets is performed. Spatial and temporal validation of those rainfall estimations is conducted by validating them with available rain gauge data during a rainy season in December 2007. Temporal validation result shows that TMPA demonstrated better statistical performance than $T_{IR1}$ and RR statistical relationship model. However for the spatial correlation, $T_{IR1}$ and RR statistical relationship model shows reasonably better performance than TMPA.


**Keywords:** MTSAT, TRMM 2A12, TMPA, rainfall estimation, validation

## 2.1. INTRODUCTION

Floods and landslides are noticed as two of natural hazards that repeatedly occurred during rainy seasons in Indonesia. Floods (e.g. inundation, flash flood, debris flow, etc) and landslide that triggered by severe storm have very serious impact to the loss both infrastructures and lives. As reported by SCTV (a private TV station in Indonesia) during December 2007, there were at least 21 of big floods events in 8 landslides events struck several different places in Java Island (SCTV 2008). Total casualties of the events for flood and landslide were 23 and 63 respectively and the events cause losses of thousand houses and infrastructures.

Many of the natural hazard casualties can be avoided if there is an early warning to the prone area due to the occurrence of successive high intensity of rainfall. The slow dissemination of measured rainfall information most likely is considered as serious obstacle in terms of the use of meteorological information for early warning purpose. It is because the limitation of meteorological infrastructure itself. Many of them are still using manual measuring and recording system instead of automatic measurement networks with telemetry system. Another drawback of rain gauges measurement is that they are limited in spatial coverage.

A different system of rainfall measurement that nearly real-time, covers wide area and depict spatial distribution of rainfall is necessary to implement. One of system that can be applied is satellite based rainfall estimation data products. There are three methods that can use for estimating rainfall from the satellite based upon type of observation i.e. (i) Visible and Infrared (VIS/IR) method; (ii) Passive and Active Microwave Method (PMW); and (iii) Multisensor Techniques Method (Kidd, et al., 2010). The VIS/IR method uses indirect approach for rainfall estimation, i.e. according to top surface cloud characteristics such as shape, brightness, temperature etc. Since the sensor is carried out by geostationary satellite, the global coverage of rainfall estimation can be provided. The PMW method uses more direct rainfall estimation. It utilizes interaction between hydrometeor and microwave such as scattering and emission. The limitation of this method is that observations are currently only available from low earth orbit satellite. It makes lower temporal resolution of PMW observation than VIS/IR method. The mutisensor techniques combine the advantages of VIS/IR and PMW methods. The principle of multisensor techniques is to adjust the IR using the other dataset such as radar, rain gauge or other satellite datasets (Kidd, et al., 2010). There are several ready to use satellite rainfall estimation products based on multisensor techniques such as TRMM Multi-satellite Precipitation Analysis (TMPA), Climate Prediction Morphing Method (CMORPH), Precipitation Estimation from Remotely Sensed Information using Artificial Neural Network Multispectral Analysis (PERSIANN-MSA), and Global Satellite Mapping of Precipitation (GSMaP) (Kidd, et al., 2010).

The datasets are mainly delivered via internet through their respective dedicated product web page location.

This study is addressed to perform rainfall estimation based on multisensor technique by blending Multi-functional Transport Satellite (MTSAT) and Tropical Rainfall Measuring Mission (TRMM) 2A12 dataset in order to provide near real time rainfall information, especially for hazard study purposes. MTSAT that captured the hemisphere in a quite high temporal resolution (1 hour) has good capability to monitor atmospheric condition such as rainfall by using its VIS/IR sensors. However, cloud is opaque in VIS/IR spectral bands, so rainfall estimation by using those of spectral bands are mainly based on the cloud top characteristics. In order to get more accurate estimation, the advantage of TRMM is accommodated. TRMM has more direct rainfall estimation due to its capability to penetrate the cloud and interact with hydrometeor.

Although there are several ready in use rainfall estimations freely available, the development of rainfall estimation that uses fine resolution satellite such as geostationary satellite dataset is still needed. The motivation of this study is to provide rainfall estimation for rainfall triggered hazard such as flash flood. Most of flash flood events occurred in small river basin with a drainage area of a few hundred square kilometers or less (NRC, 2005). Moreover flash flood is triggered by very intense and short duration rainfall (Dingman, 2002). Some flash flood events occurred in tropical regions such as Indonesia are triggered by isolated convective storm over small river basin. The current available satellite-based rainfall datasets that mainly cover global scale (i.e. 0.25° × 0.25° and 3 hours for TMPA) is considered relatively coarse resolution when it is used for flash flood early warning detection purposes. Another consideration is due to the indirect nature of the relationship between spectral information from satellite and corresponding rainfall that makes those of rainfall prediction area not universally applicable (Wardah et al., 2008).

There are two main objectives of this study. Firstly is to perform rainfall estimation based on ($T_{IR1}$) and RR statistical relationship. Secondly is to evaluate the performance of rainfall estimation and to compare with ready to use rainfall estimation TMPA dataset by validating both temporally and spatially with available rain gauge data.

## 2.2. THE STUDY AREA AND DATASETS

The study area is Java Island located on 5°S to 10°S and 95°E to 105°E (window size 5° × 10°). For the validation purpose due to limitation of time of study and the availability of measured

rainfall data, only southern part of Central Java i.e. Yogyakarta city and its surrounding is selected. The area of study and the validation area are presented in Figure 2.1.

The number of rainfall station situated in validation area is 22 automatic stations. Those of rainfall stations are operated by several different institutions i.e.: SABO Agency (Balai SABO) Yogyakarta, Public Work Agency of Progo Bogowonto Lukulo (Probolo Agency), Faculty of Geography, Gadjah Mada University and Agricultural Technology Research Agency (Balai Penelitian Teknologi Pertanian) of Yogyakarta.

The validation period is conducted during December 2007 (31 days). The rain gauge data is mainly delivered in 1 hourly average rainfall, thus in this case there are 744 data. The same number of MTSAT images is acquired from WebGMS-MTSAT/GMS (HIMAWARI) data processing on WWW, Earthquake Research Institute & Institute of Industrial Science, University of Tokyo. TMPA (also known as TRMM version 3B42) datasets are derived from http://mirador.gsfc.nasa.gov.

## 2.3. METHOD AND VALIDATION SCHEMES

### 2.3.1. The blending process through $T_{IR1}$ and RR statistical relationship

The method that is used in the current study mainly is adopted from the algorithm developed by Maathuis (Maathuis et al., 2006). The method has been chosen because it is relatively simple both in data need and process, affordable for non-meteorologist and low cost computing. The original method uses Meteosat Second Generation (MSG) and TRMM as data input. Since this study is conducted over Java Island that isn't covered by MSG, therefore MTSAT and TRMM are utilized as data input. Here, it assumed that the IR band (10.8 µm) of MSG is comparable to IR1 (10.3µm – 11.3µm) of MTSAT and the water vapor band (6.2µm) of MSG is comparable to IR3 (6.5µm – 7 µm) of MTSAT.

(a) (b)

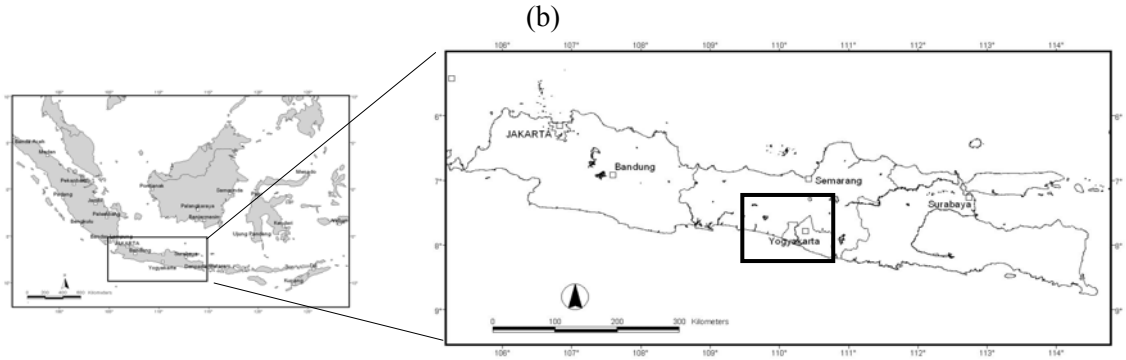


**Figure 2.1.** *(a) Study area which cover Java Island and (b) validation area that cover Yogyakarta and its surrounding area.*

The basic idea of $T_{IR1}$ and RR based rainfall estimation is to develop statistical relationship between cloud top temperature depicted by MTSAT IR1 datasets ($T_{IR1}$) and rain rate observed by TRMM 2A12 datasets (RR). For the convective cloud situation, the relationship between cloud top temperature and rain rate shows that the low cloud top temperature is associated with heavier rainfall (Kuligowski, 2003). A statistical regression should be developed to express that relationship. To draw such statistical relationship the exponential curve is used. It means that the rain rate is decreasing exponentially along the increasing of cloud top brightness temperature (Vicente et al., 1998). The developed statistical regression will be used to generate rainfall estimation based on MTSAT datasets.

The most important step during performing this method is how to get collocated image both temporally and spatially between MTSAT and TRMM dataset. It is a prerequisite in order to develop strong statistical relationship between cloud top temperature and rainfall rate. The ideal collocated image is those of MTSAT data and TRMM data that have the same acquisition time over the same area. In the real situation this ideal condition is difficult to fulfill. Actually, only the collocated images that have almost the same time of acquisition over the area can be selected. Because of the lag of acquisition time, a slightly discrepancy of cloud spatial distribution is depicted in collocated image.

In order to reduce such discrepancy, an averaging process for TRMM data based on the grouped MTSAT-IR cloud temperature (e.g. 0.5 K or 1 K equal range temperature) is performed (Maathuis et al., 2006). This process can increase the correlation coefficient of the relationship between cloud top temperature and rainfall rate. The discrepancy is tried to be reduced by limiting the coverage of collocated image during statistical relationship development. This process is performed to improve the original algorithm that used whole coverage as collocation window. The collocated window size that used by Heinemann et al. (2008) i.e. 5º × 5º to divide the whole domain window size into two smaller windows has been adopted. The relationship of both windows is examined by comparing the correlation coefficient. The best statistical relationship is chosen to estimate the rainfall of whole coverage area.

The last process for rainfall data generation is performed by the best regression equation based on MTSAT cloud temperature. The rainfall data generation process is only applied to the MTSAT cloud top temperature that considered as potential precipitating cloud. The potential precipitating cloud has been selected by the brightness temperature difference between IR1 and IR3 that is less than 11 K (Maathuis et al., 2006). Each regression function will valid to certain range of MTSAT image series. Figure 2.2 shows the schematic diagram of rainfall estimation using $T_{IR1}$ and RR statistical relationship used in this study.

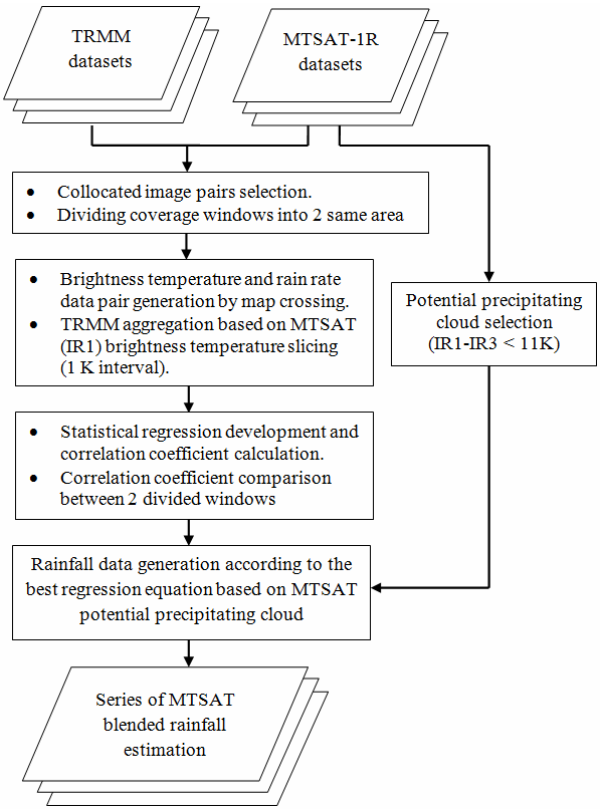


**Figure 2.2.** *Blending method between $T_{IR1}$ and RR derived from MTSAT and TRMM 2A12 respectively.*

### 2.3.2. Validation Schemes and Statistical Analysis

In order to measure the performance of $T_{IR1}$ and RR based rainfall estimation, a validation is performed by comparing it with rain gauge data both in temporally and spatially scales. As a comparison, the same validation process is also performed for the TMPA datasets.

Temporal validation is performed in point to pixel basis i.e. point rainfall data from rain gauge measurement and pixel based rainfall estimation from satellite. Hourly average and 3 hourly average rain gauge data are used to validate $T_{IR1}$ and RR based rainfall estimation and TMPA rainfall estimation respectively. Pixel information that contains rainfall estimation from satellite is retrieved according to the coordinate location of rainfall stations. For each rain gauge location, a pair of estimated and observed rainfall has been generated.

Statistical comparison has been performed for those of pair data. Some categorical statistics has been employed such as accuracy, bias score, Probability of Detection (POD), False Alarm

Ratio (FAR) and Critical Success Index (CSI) to evaluate the performance of rainfall estimation from satellites.

A dichotomous method is used to say ‘yes’ if rain$\neq$0 and to say ‘no’ if rain=0. There are four combinations possible when compare between yes/no of observed and yes/no of estimation (see Table 2.1).

- Hit – if both estimation and observed say ‘yes’
- Miss – if estimation said ‘no’ but observed say ‘yes’
- False alarm – if estimation said ‘yes’ but observed say ‘no’
- Correct negative – if both estimation and observed say ‘no’

The categorical statistic parameters are calculated according to the following equations (Ebert, 2007):

$$Accuracy = \frac{hits + correct\ negatives}{total} \tag{2.1}$$

$$Bias\ score = \frac{hits + false\ alarms}{hits + misses} \tag{2.2}$$

$$POD = \frac{hits}{hits + misses} \tag{2.3}$$

$$FAR = \frac{false\ alarms}{hits + false\ alarms} \tag{2.4}$$

$$CSI = \frac{hits}{hits + misses + false\ alarms} \tag{2.5}$$

**Table 2.1.** *Contingency table to summarize the number of hits, false alarms, misses and correct negative that is used to calculate categorical statistics.*

| | | Observed | | |
|---|---|---|---|---|
| | | Yes | No | Total |
| Estimated | Yes | *Hits* | *False Alarms* | *Estimated Yes* |
| | No | *Misses* | *Correct Negatives* | *Estimated No* |
| | Total | *Observed Yes* | *Observed No* | *Total* |

Spatial validation is performed by calculating spatial correlation both in pixel to point and pixel to pixel basis. Spatial correlation is defined as the correlation between estimated and observed rainfall with respect to their geographical locations. In this study the spatial correlation is investigated only for convective rainfall cases. For pixel to point validation, the spatial correlation between rainfall estimation from satellite and corresponding measured rainfall data is calculated. In terms of pixel to point validation there is a remaining problem which is related to the type of data itself. Rainfall observation is considered as point data type otherwise satellite based precipitation is area data type (measured as pixel area) (Grimes et al., 1999). In order to make comparable validation, a pixel to pixel based spatial correlation is conducted. It means that the pixel from satellite rainfall estimation is compared with the pixel (grid) of interpolated observed rainfall which has the same geo-reference. The interpolated observed rainfall is generated by using the block kriging interpolation method.

## 2.4. RESULTS AND DISCUSSIONS

### 2.4.1. Temporal validation

During the validation period, there are 36 collocated images have been identified. Some of them have 2 collocations in one day. The effect of limiting the coverage of collocated image is explained below. The correlation coefficient ($r^2$) of whole window coverage and those of two divided windows is calculated. The best correlation coefficient between two divided windows is selected and plotted against correlation coefficient derived from whole window. For all collocation events the plotting result is shown in Figure 2.3. According to Figure 2.3, it can be noticed that limiting window coverage can significantly improve the statistical relationship. It is indicated by increasing correlation coefficient, especially in the collocation date 13, 17 and 26b. The discrepancies that are identified in those of collocation times mainly are the rainfall which is still detected in TRMM but actually have dissipated in MTSAT image and/or vice versa. This result shows that the limiting window process is proven useful to reduce discrepancy by separating and rejecting it in one window and choose the other one that has less discrepancy.

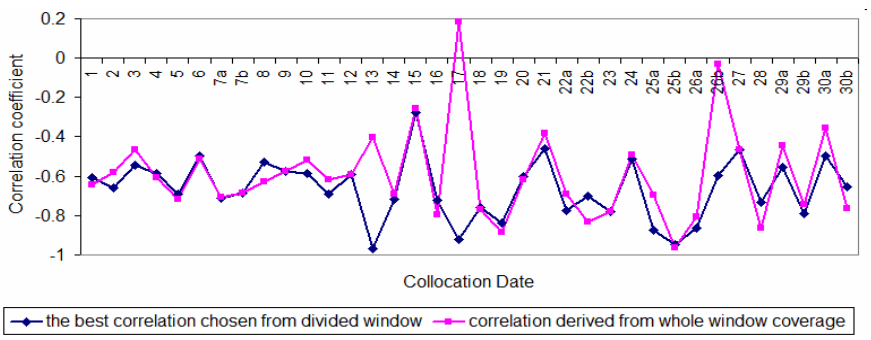


**Figure 2.3.** *Comparison of correlation coefficient of the collocated images.*

**Table 2.2.** *Summary of categorical statistic for $T_{IR1}$ and RR based rainfall estimation and TMPA.*

| Categorical statistic parameters | $T_{IR1}$ and RR based rainfall estimation | TMPA |
|---|---|---|
| Accuracy | 0.59 | 0.72 |
| bias score | 4.54 | 0.78 |
| POD | 0.83 | 0.49 |
| FAR | 0.79 | 0.33 |
| CSI | 0.20 | 0.38 |

In relation to temporal validation, the result is shown in Table 2.2. It can be examined that TMPA has higher accuracy than $T_{IR1}$ and RR based rainfall estimation. The result indicates that 72% of TMPA estimation is correct while $T_{IR1}$ and RR based rainfall estimation is only 59% correct. This condition is likely related to the probability of good collocation images that may be occurred during rainfall estimation process. TMPA has higher probability to have good collocation because it uses several PMW data compared with $T_{IR1}$ and RR based rainfall estimation that only use one PMW data.

According to bias score, it shows that $T_{IR1}$ and RR based rainfall estimation have a tendency to be overestimated and TMPA tend to be slightly underestimated. It indicates that potential precipitating cloud is more frequently detected in $T_{IR1}$ and RR based rainfall estimation than TMPA. This situation is consistent with high POD value. The FAR value of $T_{IR1}$ and RR based rainfall estimation is also quite high and it is indicated that many potential precipitating cloud detected by MTSAT images which are not producing rain. The CSIs of both $T_{IR1}$ and RR based rainfall estimation and TMPA are quite low i.e. only 20% and 38% (respectively) of 'rain' event both observed and/or estimated are correct. Based on those of statistical scores, it concludes that TMPA has better performance than $T_{IR1}$ and RR based rainfall estimation in terms of temporal validation.

### 2.4.2. Spatial validation

Two convective storms have been chosen as the case study for spatial validation. The first case is 16 December 2007 storm that consist of series of MTSAT images from 06:30 UTC - 15:30 UTC. The second is 18 December 2007 from 04:30 UTC - 12:30 UTC.

For the comparison purpose, series of TMPA data is also selected for the same time range of storm event. However, pixel to point validation such as performed in $T_{IR1}$ and RR based rainfall estimation spatial validation cannot be performed, due to the large size of TMPA's spatial resolution (0.25° × 0.25°). In this case the TMPA rainfall estimation is compared with the group

of rainfall station as average observation rather than individual station. The group of rainfall stations is defined according to the spatial resolution of TMPA. The centroid of corresponding TMPA's pixel has been considered as coordinate location of each group. Spatial correlation is calculated based on those average rainfall observation from group of stations and TMPA rainfall estimation, in the same coordinate location.

Based on those two convective storm cases, spatial correlations of both pixel to point and pixel to pixel are conducted. The result is presented in Table 2.3. Firstly, pixel to point spatial correlation of $T_{IR1}$ and RR based rainfall estimation and TMPA for both 16 December 2007 and 18 December 2007 convective storms is compared. The $T_{IR1}$ and RR based rainfall estimation spatial correlations for both storm cases are 0.36 and 0.33 respectively. Otherwise, the TMPA rainfall estimation gives the result 0.46 and -0.1 respectively. The low correlation can be readily explained due to spatial offset between cloud producing rain pixel and location of rainfall stations. Positive correlation indicated that spatial variation of the observed rainfall can be depicted by satellite image, conversely negative correlation shows that the observed rainfall distribution is not well represent by satellite image.

Those of results demonstrate that $T_{IR1}$ and RR based rainfall estimation can well represent the convective storms in both cases. Otherwise, TMPA can only represent convective storm distribution for the first case and failed to represent the second case.

Secondly, pixel to pixel spatial correlation to the same convective storm cases is compared. In order to make comparable results between $T_{IR1}$ and RR based rainfall estimation and TMPA validation, the block kriging interpolation and use the same block size as TMPA's spatial resolution is performed. The result confirmed that after spatial interpolation, observed rainfall can be well represented by both $T_{IR1}$ and RR based rainfall estimation and TMPA rainfall estimation.

**Table 2.3.** *Comparison of spatial correlation between MTSAT and TMPA for two convective rainfall cases in pixel to point and pixel to pixel basis.*

| | Pixel to point | Pixel to pixel |
|---|---|---|
| $T_{IR1}$ and RR based rainfall estimation | | |
| 16 December 2007 case | 0.36 | 0.50* |
| 18 December 2007 case | 0.33 | 0.61* |
| TMPA | | |
| 16 December 2007 case | 0.46 | 0.56 |
| 18 December 2007 case | -0.1 | 0.36 |

* = Correlation is significant at the 0.05 level (2-tailed).

The average of spatial correlation of $T_{IR1}$ and RR based rainfall estimation and TMPA from both two cases is calculated. The calculation results are 0.56 and 0.46 for $T_{IR1}$ and RR based rainfall estimation and TMPA respectively. It shows that in average $T_{IR1}$ and RR based rainfall estimation demonstrates better spatial representation of convective rainfall than TMPA.

The average value of spatial correlation of MTSAT (i.e. 0.56) has good agreement with the result of Ebert and Manton's study (Ebert and Manton, 1998) that for the instantaneous rainfall of mixed geostationary satellite and polar orbit satellite (IR-SSM/I) algorithms has correlation coefficient ranging from 0.49 to 0.55.

## 2.5. SUMMARY AND CONCLUSIONS

Regarding to the temporal validation, TMPA shows relatively better performance than $T_{IR1}$ and RR based rainfall estimation. It could be explained mainly because of TMPA algorithm developed based on various data inputs as well as complex algorithm. The relatively low statistical performance of $T_{IR1}$ and RR based rainfall estimation rainfall estimation compared to TMPA is considered as the limitation of this method. It might be because of the overestimate of potential precipitating cloud detected by $T_{IR1}$ and RR based rainfall estimation. For the further study, the more accurately potential precipitating cloud detection should be adopted. Furthermore, limiting collocated window method that already shows a promising result should be enhanced.

However for the spatial correlation, $T_{IR1}$ and RR based rainfall estimation is demonstrated better performance than TMPA. With regards to this potentiality, $T_{IR1}$ and RR based rainfall estimation algorithm is quite promising as an alternative method for providing rainfall data for ungauged remote area. It can be used also as an indirect approach for the rainfall triggered hazard early warning system. It is because $T_{IR1}$ and RR based rainfall estimation has shown quite good to represent spatial distribution of rainfall especially convective storm events, though the accuracy of rainfall detection should be increased. The convective storm is characterized by very intense rain in short duration (lasting less than 1 hour) and covers small area (Dingman, 2002). This type of rainfall has been considered as the causing factor of flash flood (Wardah et al., 2008). Based on this relation, MTSAT dataset that have good spatial and temporal resolution can be considered to be used for such kind of rainfall related hazard studies. Another consideration is that $T_{IR1}$ and RR based rainfall estimation is only need simple data input and processing and low cost computing. This consideration is beneficial in term of practical point of view.

# Chapter 3. REMOTE SENSING BASED CLOUD TYPE CLASSIFICATION FOR SUPPORTING RAINFALL ESTIMATION

---

This chapter is based on:

Suseno, Dwi Prabowo Yuga, T. J. Yamada, 2011, **The Use of Cloud Type Classification To Improve Geostationary Based Rainfall Estimation.** *9th International Symposium on Southeast Asian Water Environment*, Dec 1st-3rd 2011 Bangkok City, Thailand.

Suseno, Dwi Prabowo Yuga, T. J. Yamada, 2012, **Two-dimensional threshold-based cloud-type classification using MTSAT data**, *Remote Sensing Letters*, Vol. 3 Issue 8. pp 737-746.

## Abstract

A new two-dimensional threshold diagram (2D-THR) has been developed based on maximum likelihood cloud classification results, which can readily be applied for Multi-functional Transport Satellite (MTSAT) split window datasets. Since 2D-THR was trained using northern summer 2010 data for Japan and its surrounding area, it is typically suitable only for summer. Comparison of snapshot cloud-type distributions showed that 2D-THR images and the corresponding night-time microphysical colour composite images as well as 2D-THR and Japan Meteorological Agency (JMA) cloud-type images are in good agreement. A time series inter-comparison of the hourly 2D-THR cloud classification results with the JMA cloud type classification data product was performed by calculating spatial correlation of cloud percentage for 1° × 1° grid cells. For cumulonimbus, high-level, middle-level, and low-level clouds over tropical and subtropical areas in the northwestern Pacific Ocean region, the spatial correlation between 2D-THR and JMA is moderate. Thus, 2D-THR cloud-classification algorithm can be applied in both regions. Integrating the cloud type classification especially by separating Cumulonimbus (Cb) cloud type from other cloud types can improve the MTSAT 10.8μm cloud top temperature ($T_{IR1}$) and rainfall rate (RR) relationship, which is indicated by increasing correlation coefficient and the gradient of regression line. Moreover, underestimating rainfall intensity can be avoided by applying rainfall rate and cloud top temperature relationship that uses Cb cloud type only rather than using all cloud types. A good agreement between estimated and measured storm rainfall also has been demonstrated when use this approach.


**Keywords:** Cloud type classification, MTSAT, 2D threshold diagram, rainfall estimation

## 3.1. INTRODUCTION

In an early warning system of rainfall triggered hazard such as flood and landslide, storm rainfall data is key information. Storm rainfall data should be prepared as soon as possible in order to provide sufficient warning time. The use of measured rainfall data for early warning purpose sometimes is not enough because the rainfall event actually had been occurred so available times for warning become limited. The other problem is the distribution of the rain gauge sometimes too sparse, even ungauged in some remote places. In this regards the use remote sensing technology for rainfall estimation is a practical alternative to be applied to overcome those of problems.

One approach of using remote sensing for rainfall estimation is multisensor approach i.e. by developing the relationship between cloud properties data provided by satellite sensors and rainfall data measured by gauge or other satellite sensors in the same collocated time and space. A rainfall estimation study based on relationship between rainfall rate and satellite based cloud top brightness temperature and rainfall rate relationship ($T_{BB}$ and RR relationship hereinafter) had been conducted by employing MTSAT and Tropical Rainfall Measuring Mission (TRMM) datasets over Java Island, Indonesia (Suseno and Yamada, 2011a). The cloud top temperature is related to rainfall rate which lower cloud top temperature is associated with heavier rainfall. However this assumption is reasonable for convective cloud type such as Cumulonimbus (Cb) but poor for other cloud type such as Cirrus (Ci) that cold but light or no rain and stratiform clouds that warm but wet (Kuligowski, 2003). In order to fulfill this assumption cloud type information is necessary to be integrated in the multisensor rainfall estimation approach.

On the subject of cloud classification, there are several satellites and methods have been used and developed as well. The cloud type classification method generally can be categorized as supervised classification and unsupervised classification. Supervised classification uses specific areas in the satellite image that defined by analyst which represents homogenous example of earth object. These areas are commonly referred to as training sites because the spectral characteristics of these known areas are used to train the classification algorithm for eventual earth objects mapping of the remainder of the remote sensing image (Jensen, 2005). The benefit of using supervised classification is that analyst can control the categories or classes according their specific purpose. However this method is time consuming, especially during training area selection. On the purpose of early warning which speed processing time is necessary, this method is not practical. The unsupervised classification which uses simple process such as thresholding technique is more common to be used (Inoue, 1987; Lensky et al., 2003; Saunders, 1988). Threshold classification uses a specific or a range of spectral values as the boundary among the

classes of object. Threshold classification is considered as 'quick and dirty' method however the threshold value should be defined carefully in order to deliver reliable classification result. An investigation of the physical characteristics of the cloud usually is performed in order to define threshold value such as by examining the characteristics of brightness temperature difference (BTD) between 11 and 12 µm (Inoue, 1987), the radiance and BTD with precipitation rain data (Inoue et al., 2000), and microstructure and precipitation potential (Lensky et al., 2002).

The spectral response of ice and water cloud is shown in Figure 3.1. It can be observe that on the channel 10.8µm (IR1) and 11µm (IR2), ice cloud have larger absorption than water cloud, therefore cirrus cloud which contains ice is easily distinguished with the other cloud type. Moreover, the large difference between IR1 and IR2 (BTD12) is also good indicator for distinguishing between optically thick cloud and optically thin cloud (Inoue, 1989). The 3.75µm channel (IR4) shows different spectral characteristic during day and night acquisition because in the daytime the reflectance is dominant in comparison with IR1 and IR2, otherwise in the night time the infrared radiation is observed (JMA, 2002). With this regards, the time acquisition between day time and night time during cloud type interpretation is considered since BTD14 in the color composite image is used.

The objectives of this study have two folds, firstly to develop a threshold based classification method by examining the results of supervised cloud types classification. Since there is no threshold diagram that specifically to be applied for MTSAT, the focus of this study is to develop a new two-dimensional (2D) threshold diagram based on IR1 and BTD IR1 minus IR2 (BTD12) of MTSAT satellite sensors. Secondly is to integrate the threshold based cloud type classification result for developing the $T_{BB}$ and RR relationship. By separating cloud type during statistical relationship development, it assumed that it can improve the quality of $T_{BB}$ and RR relationship. For the purpose of rainfall estimation, a common $T_{BB}$ and RR relationship will be developed instead of using individual TBB and RR relationship of each storm rainfall cases.

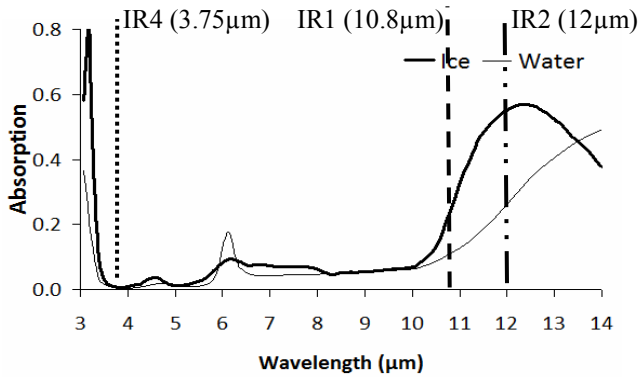


**Figure 3.1.** *Spectral characteristics of ice and water cloud (Kerkmann, 2004)*

## 3.2. STUDY AREA AND DATA

The domain for developing the new threshold cloud-type classification covers Japan and its surrounding area (30°N–50°N and 120°E–150°E). The validation area covers northwestern Pacific Ocean (0°–52° N and 114° E–160° E). The validation area was larger than the development area because the possibility of applying the new threshold in a tropical region was considered to be examined. The MTSAT images for the northern summer i.e. June, July, August, and September (JJAS) for 2009 and 2010 is acquired. The images used are freely downloadable from the websites of Institute of Industrial Science, University of Tokyo (Takeuchi et al. 2010) and Kochi University Weather Home (Kochi University 2011). MTSAT 2R has been operational since 1st July 2010 and it has replaced MTSAT 1. Consequently, the MTSAT 1 for JJAS 2009 and June 2010 and MTSAT 2R for July to September 2010 are utilized. However, due to the same specifications of visible and IR sensors for both MTSAT 1 and 2R, it is assumed that there is no difference in the spectral characteristics of the images. In the study region, the spatial resolution of MTSAT data is ~5 × ~5 km. Moreover, MTSAT has a temporal resolution of 1 hour and has five spectral channels that are centered at 0.725 µm (Visible), 10.8 µm (IR1), 12.0 µm (IR2), 6.75 µm (IR3), and 3.75 µm (IR4).

The Japan Meteorological Agency cloud-type classification data product (hereafter JMA) was utilized for the inter-comparison. The spatial and temporal resolutions of the JMA are 0.25° × 0.25° (~25 km × ~25 km) and 1 hour, respectively. JMA uses MTSAT images as well as additional information in their cloud type classification algorithm. There are two main processing steps for classifying the raw image pixel, namely stratification and discrimination. In the first step, a dynamic threshold is employed to slice the IR1 image by using the vertical temperature profile of the atmosphere at 400-hPa and 600-hPa levels; the temperature profile is derived from meteorological reanalysis data. In the second step, for the determination of more specific cloud type, especially for the lower level clouds, the reflectance information from visible and IR brightness temperatures as well as IR channel difference, for example, IR1 - IR2 and IR1 - IR3, has been employed (JMA 2007).

## 3.3. METHODS

### 3.3.1. The development of 2D-THR based cloud type classification.

A threshold boundary for cloud type classes are developed; this boundary was represented in a two-dimensional threshold diagram (hereafter 2D-THR) of IR1 brightness temperature ($T_{IR1}$)

vs. the brightness temperature difference between IR1 and IR2 ($\Delta T_{IR1-IR2}$). Here, the result of supervised cloud-type classification is used to adjust the threshold boundary among cloud types. The cloud type clusters derived from the supervised cloud-type classification then were plotted by using their mean centers in a $T_{IR1}$ vs. $\Delta T_{IR1-IR2}$ scatterplot.

The development of new a threshold began with selecting images that were used for cloud-type analysis by supervised multispectral classification. Eight classes were considered for cloud-type analysis in this study. These were Cb, mature Cb (MCb), thick cirrus (TkCi), thin cirrus (TiCi), middle-level cloud (MC), low-level cloud (LC), clear land area, and clear sea area. Images that clearly depicted these cloud classes were selected. The 41 scenes of images as a representation of each month during the JJAS 2010 period had been selected. Of these, 11, 9, 11, and 10 scenes represented June, July, August, and September, respectively. It was assumed that since the images for JJAS 2010 were used, the resulting threshold diagram would be valid specifically for the summer season.

A false color image composite called Night Microphysical color scheme (Lensky and Rosenfeld, 2008) was used as the background image for identification of the cloud types during training area selection. Some visual cloud properties such as texture, organizational pattern, edge definition, size, and individual shape (Conway 1997) were also considered.

Two types of image classification algorithms, namely, maximum likelihood (MAX) and multilayer perceptron neural network (NN) were adopted for multispectral supervised classification. The performances of these algorithms were compared by using the same input bands and training sample areas during the classification process.

A map-to-map comparison was conducted to determine the agreement between MAX vs. JMA and NN vs. JMA by using the kappa coefficient of agreement ($K_{hat}$). $K_{hat} > 0.8$ represents strong agreement; $0.4 < K_{hat} < 0.8$ represents moderate agreement; and $K_{hat} < 0.4$ represents poor agreement (Jensen 2005). A reclassification and resampling procedure helped compare the data in terms of the cloud classes and spatial reference. $K_{hat}$ values were calculated for the 41 pairs of resampled images of MAX vs. JMA cloud-type and NN vs. JMA cloud-type. Figure 3.2 shows a graphical comparison of the $K_{hat}$ values of these image pairs. The average $K_{hat}$ for MAX vs. JMA cloud type and NN vs. JMA cloud type are 0.44 and 0.42, respectively. These values indicate moderate agreement between the supervised classification result and JMA cloud type. The results confirm that MAX has slightly better agreement than NN; therefore, the MAX cloud classification results were decided to be used to train the 2D-THR.

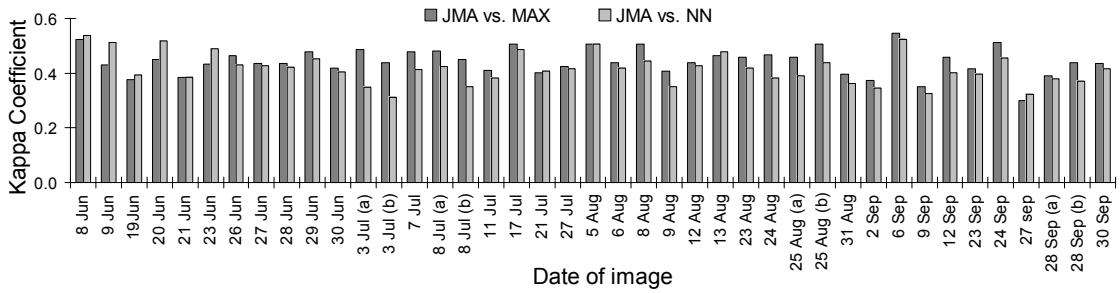


**Figure 3.2.** *Comparison of Khat values between JMA vs. MAX and JMA vs. NN for selected images during JJAS 2010.*

On the basis of MAX cloud classification results, the cloud-type clusters was generated by plotting the $T_{IR1}$ and $\Delta T_{IR1\text{-}IR2}$ of corresponding cloud types derived from 41 classified images. However, it proved difficult to delineate the border of each cloud-type cluster for defining the threshold boundary value from such cloud-type scatterplots, because of the overlapping of the cloud-type clusters. To overcome this problem, the original scatter plot has been modified by plotting only the mean centre of the cloud cluster, instead of all points. The mean centre of the cloud cluster was calculated for every cloud type by using the equation (Rogerson 2006):

$$X_c = \sum_{i=1}^{n} w_i T_{\mathrm{IR1}} \Big/ \sum_{i=1}^{n} w_i ; \quad Y_c = \sum_{i=1}^{n} w_i \Delta T_{\mathrm{IR1\text{-}IR2}} \Big/ \sum_{i=1}^{n} w_i \tag{3.1}$$

where $X_c$ and $Y_c$ are the coordinates of the mean centre of the cluster of cloud-type c. Further, wi is the weight of point i, i.e., the position of $T_{IR1}$ and $\Delta T_{IR1\text{-}IR2}$ in the scatterplot, n is number of points. The weight was calculated by dividing the frequency of occurrence of point i by the total frequency of occurrence of all points.

This process can simplify the cloud-type scatterplot distribution because currently it only consists of 41 points representing the mean centers of each cloud type (Figure 3.3a). Here, the grouping of cloud-type cluster can be more easily evaluated. An adjustment process was performed by tuning the boundary values of the diagram and comparing the 2D-THR classified images using current threshold values with the corresponding MAX images for the 41 cases. Several iterations of the adjustment process were conducted until at least moderate agreement with most of the MAX images was realized. From 41 comparisons between 2D-THR and MAX images, there are 38 image pairs that satisfied the conditions $K_{hat} > 0.4$. The final 2D-THR threshold boundary is shown in Figure 3.3b. This 2D-THR can be used as a look-up table by comparing the combination of values of $T_{IR1}$ and $\Delta T_{IR1\text{-}IR2}$ for the same pixel location with the diagram to get the cloud-type image.

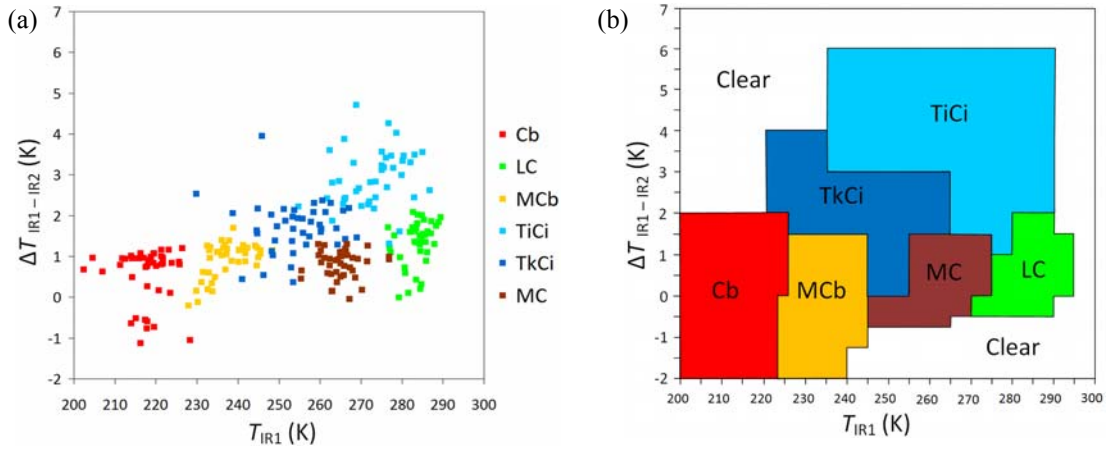


**Figure 3.3.** *(a) A scatter plot of mean centre of each cloud type derived from MAX classification results; (b) 2D-THR for cloud-type classification by using $T_{IR1}$ and $\Delta T_{IR1-IR2}$ of MTSAT 1R.*

Before applying 2D-THR for retrieving the cloud type, the cloud pixels were identified by using the IR1 channel. The cloud-pixels screening relations derived by Choi and Hoi (2009) was utilized. However, a modification was done to such relations since it was utilized only TIR for day and night-time cloud detection by following relations:

$$(T_{IR1}^{clr} - T_{IR}) > \delta_{IR} \qquad (3.2)$$

where $T_{IR1}^{clr}$ and $T_{IR1}$ are the IR1 clear-sky brightness temperature and $T_{10.8}$ total-sky brightness temperature, respectively. The IR1 clear-sky value is the maximum value of all IR1 images for August 2010.

The equation 3.2 has been applied to the previous 41 scenes to get the binary images represent cloudy and non cloudy area. The value of $\delta_{IR}$ given by Choi and Hoi (2009) was utilized as the initial value. The $\delta_{IR}$ was tuned by visually comparing the cloud binary images with the cloud features depicted by the corresponding night microphysical colour composite images. The adjusted value of $\delta_{IR}$ was 20 K for detecting cloud over land and 7K over sea. The value was higher than that specified by Choi and Hoi (2009) i.e. 8K for land and 3.5K for sea. It was most probably due to different area of coverage which influenced the value of IR1 clear-sky.

### 3.3.2. Validation of 2D-THR based cloud type classification.

The ideal way of validating the cloud-type classification result is to compare the data with actual weather observations. Owing to the lack of observation data, the 2D-THR was compared with the JMA product. Since both data sets are basically the result of estimation with their own

uncertainty, in this case the geographical relationship of cloud-type occurrence represented by both data sets was simply compared. The spatial correlation to show such spatial relationships between 2D-THR and JMA cloud classification was utilized. Within a 1° × 1° grid cell for respective 2D-THR and JMA images, the number of pixels for every cloud type was counted. The original resolution of both corresponding cloud classifications during this process was preserved. The cloud-type percentage was calculated for each grid cell by dividing the count of number of cloud types by the total number of cloud pixels within the grid area. Thus, a cloud percentage map was generated from 2D-THR and JMA images for each cloud type, and the correlation coefficient was calculated accordingly (Rogerson 2006). However, since 2D-THR is based on a split window channel, it has limitations when a more detailed classification scheme such as that in JMA is used. Hence, 2D-THR uses a simpler cloud-type classification than JMA. Therefore, the classification scheme of 2D-THR and JMA has to be reclassified for them to be comparable with the new classifications shown in Table 3.1. TiCi and TkCi in the 2D-THR classification scheme were reclassified as high-level cloud (HC), thus Stratocumulus, Cumulus, Stratus/Fog in the JMA classification scheme were reclassified as LC in the new reclassified classes.

### 3.3.3. Integration of 2D-THR based cloud type classification into statistical based rainfall estimation.

Integration of cloud type classes into the development process of $T_{BB}$ and RR relationship is performed by considering the Cb cloud type. Pairs of collocated data between MTSAT IR1 and rainfall rate derived from 1-hourly measured rainfall are selected for every storm events indicated by the Cb cloud occurrence. The hourly rainfall event that has coincident time with MTSAT image time acquisition was chosen. Since the measured rainfall is observed as point data, so it is necessary to change the domain from point data becomes grid data format through spatial interpolation, in order to perform grid overlay with MTSAT image.

**Table 3.1.** *Reclassification of 2D-THR and JMA cloud-type classifications*

| 2D-THR | JMA | New reclassified classes |
|---|---|---|
| Clear (land and sea) | Clear | Clear |
| Cb | Cb | Cb |
| MCb | Dense Cloud | HC |
| TiCi, TkCi | HC | HC |
| MC | MC | MC |
| LC | Stratocumulus, Cumulus, Stratus/Fog | LC |

For this purpose the Block Kriging method was utilized to perform such spatial interpolation. Pairs of collocated pixel that represent cloud top temperature from MTSAT IR1 ($T_{IR1}$) and rainfall rate (RR) data from interpolated rainfall map is acquired. This pair of datasets is used to calculate $T_{IR1}$ and RR relationship by using modified exponential regression model. The effect of cloud type consideration has been investigated during $T_{IR1}$ and RR relationship development by comparing the gradient of regression line as well as its correlation coefficient that developed by including all cloud type and that consider only for Cb cloud type. Based on the pairs of $T_{IR1}$ and RR datasets for all storm events, a common $T_{IR1}$ and RR relationship is developed and to be used for rainfall estimation purpose. A spatial validation process is also conducted by comparing estimated and measured rainfall for several storm rainfalls over Japan land area.

## 3.4. RESULTS AND DISCUSSION

### 3.4.1. The 2D-THR based cloud type classification result and its validation.

Several uncertainties associated with the adjustment process of 2D-THR threshold boundary probably influence the accuracy of the cloud-type classification result. Some mean centers of certain classes are omitted because they are included in the adjacent class; this has been observed in the case of the area around 225 K < $T_{IR1}$ < 230 K and $\Delta T_{IR1-IR2}$ < -0.5 K; 225 K < $T_{IR1}$ < 230 K and 0.5 K < $\Delta T_{IR1-IR2}$ < 1.5 K; and 275 K < $T_{IR1}$ < 280 K and 1 K < $\Delta T_{IR1-IR2}$ < 2 K. The same adjustment process was also performed to adjust the area which lack of mean centre of cloud type such as the area corresponding to 290 K < $T_{IR1}$ < 295 K and 0 K < $\Delta T_{IR1-IR2}$ < 1.5 K, and 245 K < $T_{IR1}$ < 255 K and -0.5 K < $\Delta T_{IR1-IR2}$ < 0 K. For the outer boundary of the 2D-THR, extrapolation was based on the outer boundary cluster of cloudy pixels in the $T_{IR1}$ and $\Delta T_{IR1-IR2}$ scatterplot. Another uncertainty also should be notified, in terms of defining the cloudy pixels according to Choi and Hoi (2009) where the modification of δIR was intended to somewhat reduce the distribution of some fraction of clouds for several image cases especially LC.

A snapshot of the cloud-type classification results obtained using the 2D-THR algorithm for 2 August 2009 at 02:30 UTC is shown in Figure 3.4a, along with the corresponding night-time microphysical color composite image (Figure 3.4b).

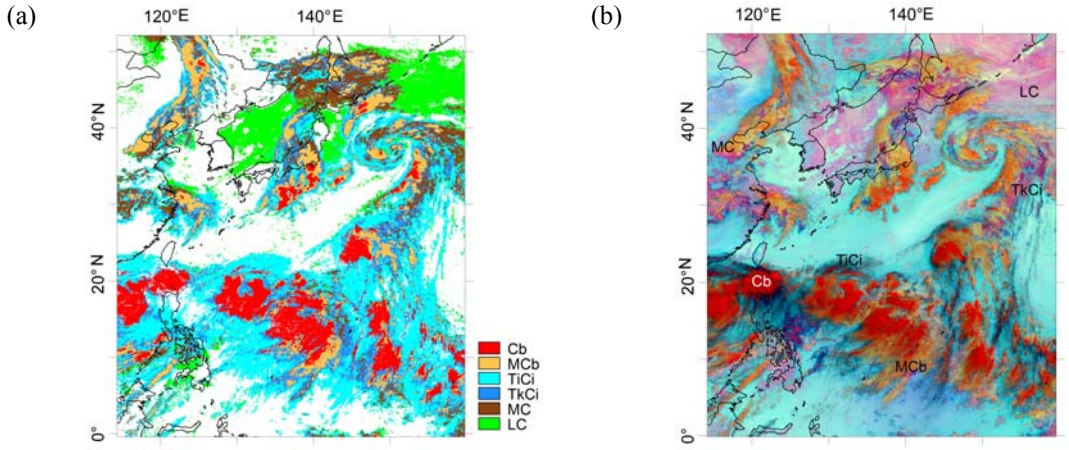


**Figure 3.4.** *(a) Cloud-type classification result obtained using 2D-THR algorithm and (b) its corresponding night-time microphysical color composite for 2 August 2009 at 02:30 UTC.*

In Figure 3.4b, the Cb and MCb that respectively shown in red and dark orange are accurately portrayed in the cloud-type classification image (Figure 3.4a). The distribution of TiCi and TkCi depicted in dark blue and violet as well as MC represented in yellow to orange also reasonably matches with cloud-type image. However, LC shown in pale pink seems to be partially portrayed in the cloud-type image.

Figure 3.5 shows the inter-comparison between 2D-THR and JMA cloud type images for the same period as in Figure 3.4. However, 2D-THR is resampled into the same spatial resolution as JMA and both are reclassified according to the same cloud classes as shown in Table 3.1. It can be observed that 2D-THR shows a larger cloud distribution area for Cb and a smaller cloud distribution area for LC than JMA. However, for HC and MC, the cloud distribution areas seem comparable.

The time series inter-comparison of hourly 2D-THR images and the JMA cloud classification was also performed for the JJAS 2009 period by comparing the spatial correlation of cloud-type percentage. Since the 2D-THR is developed for the northern summer in subtropical regions, the possibility of applying this method to tropical regions is examined. Therefore, the validation area is divided into tropical and subtropical regions and compared the validation results accordingly. The spatial correlation of cloud-type percentage was calculated after completing the reclassification and aggregation processes. The calculation results of tropical region shows that the average values of the spatial correlation are moderate, i.e. 0.64, 0.56, 0.47, and 0.55 for Cb, HC, MC, and LC, respectively.

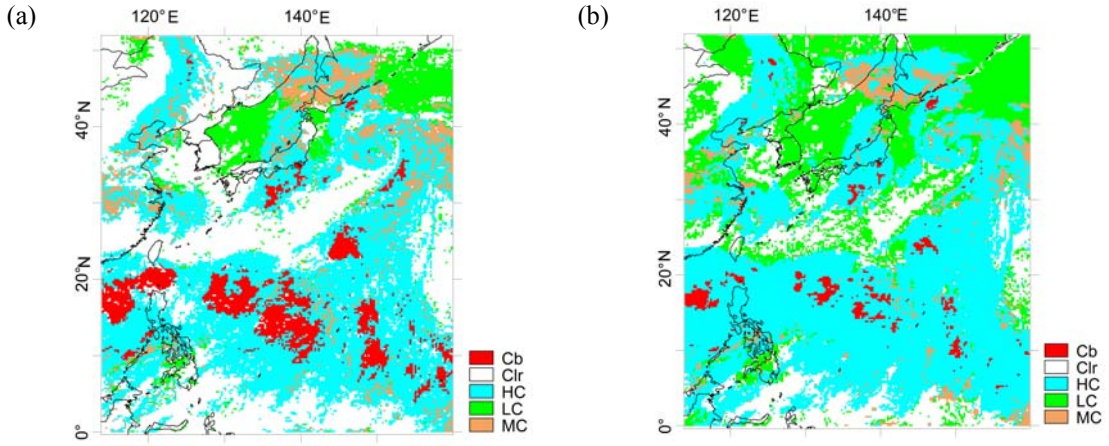


**Figure 3.5.** *Inter-comparison of the reclassified cloud type classification between (a) 2D-THR cloud type classification result and (b) the JMA product for 2 August 2009 02:30 UTC. 2D-THR is resampled into the same spatial resolution as JMA.*

Similar moderate spatial correlations are also seen for subtropical regions, i.e. 0.54, 0.71, 0.55, and 0.59 for Cb, HC, MC, and LC, respectively. Since the spatial correlation expressed the geographical relationship of the frequency of occurrence of the cloud type, these results demonstrate that the distribution of cloud type represented by 2D-THR is reasonably comparable for tropical and subtropical regions. This suggests that 2D-THR can be applied in both areas.

Figure 3.6 shows the hourly variations in the spatial correlations of Cb, HC, MC, and LC cloud percentage for tropical and subtropical regions. As already mentioned in section 3, during the calculation of cloud percentage, the original resolution of 2D-THR and JMA is preserved. Since 2D-THR has higher spatial resolution than JMA, it can represent local or isolated cloud better than JMA. This means that for certain times, 2D-THR and JMA representations of local or isolated clouds may differ. This is probably a contributing factor to the very high fluctuation of spatial correlation of cloud percentage as is observed for all cloud types in mid-July and in September. It can be observed that the spatial correlation in both tropical and subtropical regions is strongly influenced by a diurnal pattern of cloud percentage such as that clearly shown by HC, MC and LC in both tropical and subtropical regions. Detailed inspection of the figures demonstrates that the variation in diurnal patterns among cloud types sometimes has the opposite pattern because of the multi-layer effect of clouds. When the cloud percentage of a higher level cloud increases, it reduces the cloud percentage of the lower level cloud since the higher level cloud blocks the lower cloud level; therefore, the spatial correlation tends to decrease.

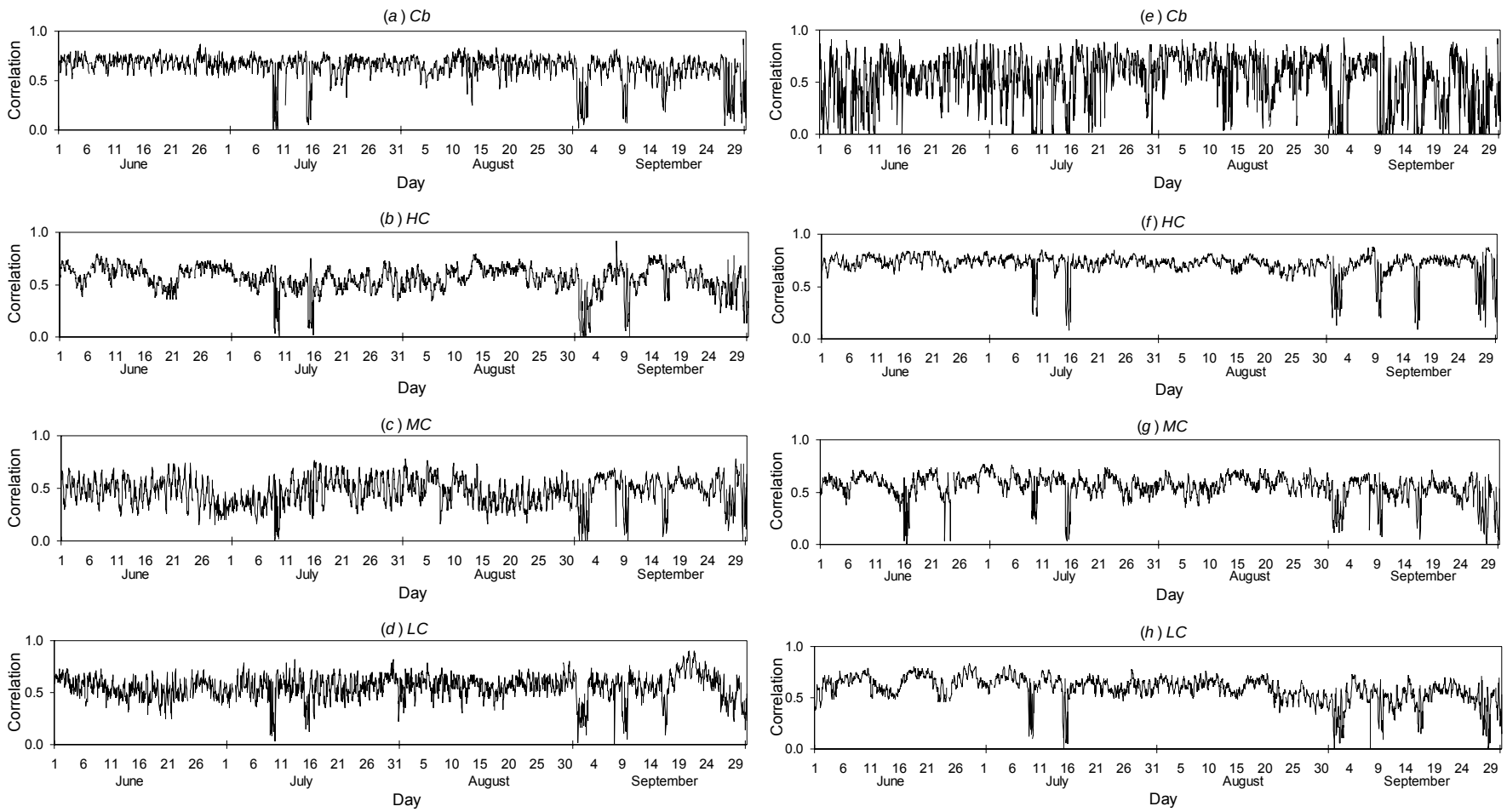


**Figure 3.6**. *Hourly variation in the spatial correlation of Cb ((a) and (e)), HC ((b) and (f)), MC ((c) and (g)) and LC ((d) and (h)) percentage between 2D-THR and JMA cloud classification for tropical region ((a)–(d)) and subtropical region ((e)–(h)) during June, July, August and September 2009.*

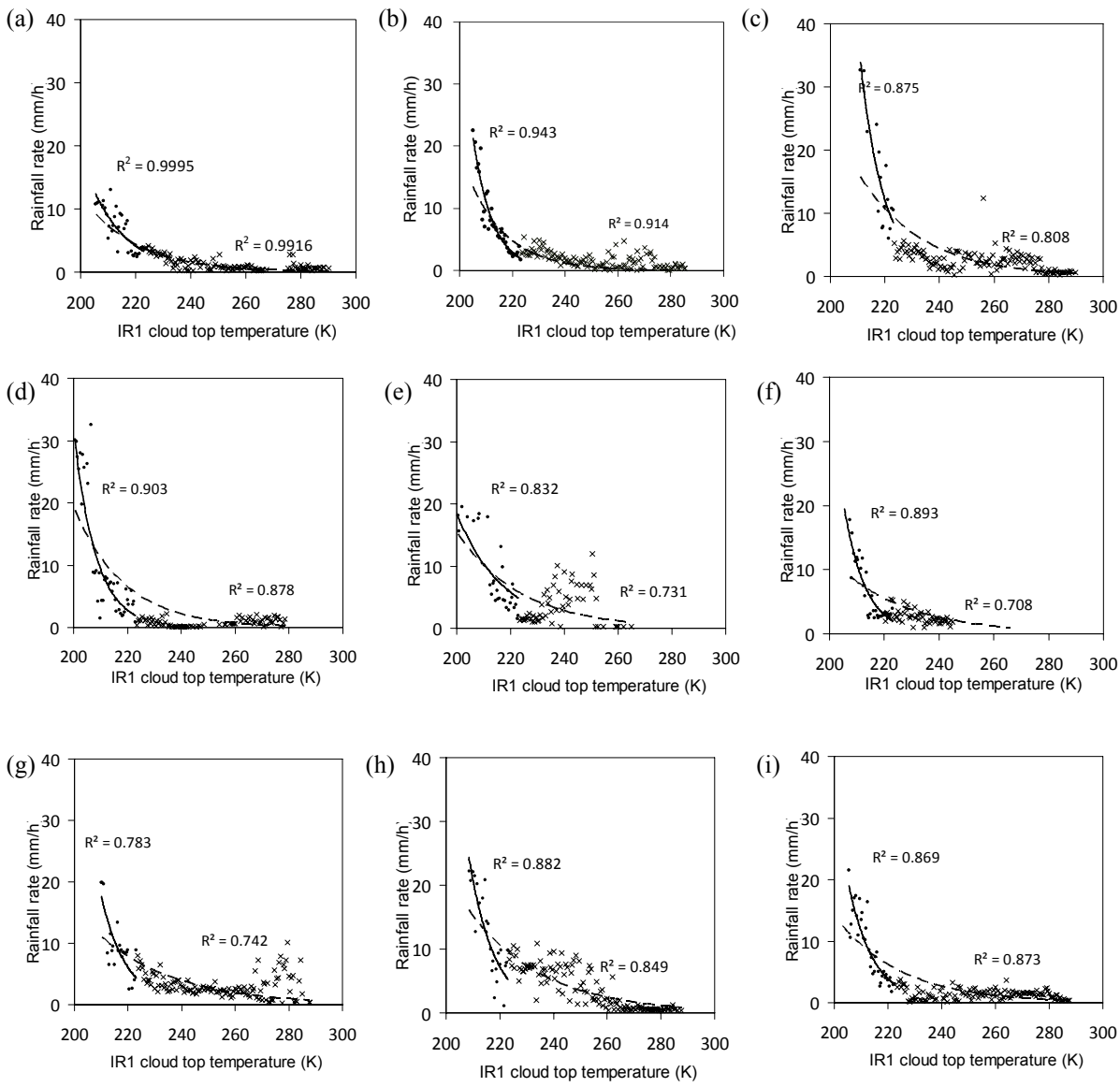


**Figure 3.7.** *Comparison of statistical regression of Tb and RR for several storm rainfall events by considering only Cb cloud (solid regression line) and by including all type of clouds in June 2010.*

### 3.4.2. Implementation of cloud type classification for statistical based rainfall estimation.

The $T_{BB}$ and RR relationship is developed for each storm cases during June – September 2010 over Japan land area. The searching radius of 25 km and 10 × 10 block size for Block Kriging interpolation of point measured rainfall is used. Figure 3.7a to 3.7i show the comparison of the regression line that developed by including all cloud type and those consider only for Cb cloud type, from respective several storm cases during June 2010 i.e. 15 June 2010 (05:00 UTC), 16 June 2010 (16:00 UTC), 20 June 2010 (06:00 UTC), 22 June 2010 (12:00 UTC), 25 June 2010

(10:00 UTC), 26 June 2010 (03:00 UTC), 27 June 2010 (10:00 UTC), 28 June 2010 (07:00 UTC) and 29 June 2010 (01:00 UTC).

The regression line comparison shows that the gradient of regression lines which include all cloud type is smaller than those used Cb only. The correlation is also generally increasing for regression which is developed only by Cb. Since the low cloud top temperature correspond to high rainfall rate (storm event), the small gradient of regression line look likes to deliver under estimation of estimated rainfall. Therefore by using Cb cloud type only during $T_{IR1}$ and RR relationship development this under estimation can be avoided.

## 3.5. SUMMARY AND CONCLUSIONS

A new 2D-THR cloud-classification algorithm has been developed; it was trained using MAX classification results for Japan and its surrounding area. The cloud-type classification boundary was defined by adjusting the threshold value of the distribution of mean centre of the cloud-type clusters in the $T_{IR1}$ and $\Delta T_{IR1-IR2}$ scatter plot. Images for northern summer (JJAS) 2009 were used for developing the 2D-THR; therefore, this diagram is typically suitable for classifying clouds during the summer. During the adjustment process, the mean centers of certain classes were omitted because they were included in an adjacent class. This may be considered as the main uncertainty of this method. The presence of some areas in the 2D-THR that lack of mean centers of cloud clusters suggests that 2D-THR should be trained by using more MAX images.

However, visual inter-comparison of a snapshot image for 2 August 2009 02:30 UTC between a 2D-THR image and its corresponding night-time microphysical color composite image, shows that most of cloud types identified in the color composite image were well represented in the2D-THR image. Inter-comparison of the JMA image and 2D-THR for the same period also proves good visual agreement between the two.

The cloud percentages for JMA and 2D-THR during JJAS 2009 over tropical and subtropical regions were spatially correlated. The results showed that the geographical distribution of the frequency of occurrence of each cloud type is moderately represented by 2D-THR. It suggests that 2D-THR can be reasonably applied for tropical and subtropical regions. 2D-THR has higher spatial resolution than JMA; hence, it can represent local or isolated cloud better than JMA. However, its cloud-type representation is different. The graphical comparison of the spatial correlation of cloud percentage during JJAS 2009 demonstrates very high fluctuation of spatial correlation for certain times; this fluctuation is most probably caused by different

representations of the local cloud type. The graph also showed opposite patterns of diurnal variation among the cloud types because of a multilayer cloud effect.

Integrating the cloud type classification especially by separating Cb cloud type from other cloud types can improve the $T_{IR1}$ and RR relationship as well as rainfall estimation, which is indicated by increasing correlation coefficient and the gradient of regression line. Moreover, underestimating rainfall intensity can be avoided by applying $T_{IR1}$ and RR relationship that uses Cb cloud type only rather than using all cloud types.

# Chapter 4. THE USE OF GEOSTATIONARY BASED RAINFALL ESTIMATION FOR CHARACTERIZING STORM SEVERITY

---

This chapter is based on: Suseno, Dwi Prabowo Yuga, T. J. Yamada, 2012, **The use of geostationary based rainfall estimation for characterizing strom severity**, *Journal of Japan Society of Civil Engineers*, Ser. B1 (Hydraulic Engineering), Volume 68, Issue 4, pp. I_175-I_180

## Abstract

This study deals with the use of geostationary satellite based rainfall estimation for characterizing storm severity. The objectives of this study are to estimate storm rainfall intensity by using Multi-functional Transport Satellite (MTSAT) blended with C-band rainfall radar data and to show the severity of the identified storm rainfall intensity by representing its return period map. A regional frequency analysis (RFA) method developed by Hosking and Wallis (1997) is used to define the frequency distribution of long-term hourly maximum rainfall over Hokkaido Island. RFA indicates that Generalized Normal/Log Normal Three Parameters (GNO/LN3) is suitable to describe the frequency distribution of long-term hourly maximum rainfall over Hokkaido Island. Based on that frequency distribution, characterization of severity of 23 August 2010 storm event has been performed over western part of Hokkaido Island using MTSAT rainfall estimation. This comparison demonstrates that that the return period information shown by MTSAT rainfall is comparable with AMeDAS rainfall return period. For assessing the return period of an extreme event in the area that observed rainfall is lacking, the use of geostationary satellite based is proved useful to overcome such problem.


**Key Words:** MTSAT, C-band radar, Rainfall estimation, Regional Frequency Analysis

## 4.1. INTRODUCTION

Evaluation of post extreme flood event is important regarding to disaster prevention and mitigation. Such evaluation can be accomplished by characterizing the severity of flood event such as by performing frequency analysis to quantify its return period. The flood's return period serves as the information for designing flood mitigation or flood control structures. However, the problem arises when there is no discharge available that corresponds to the event due to the damage of river measurement gauge caused by flash flood itself. To overcome such problem, rainfall frequency estimates are often used to describe the characteristics of flood events by calculating the return period of the greatest point rainfall intensity within the storm that is considered as the return period of the storm (Nobiarto et al., 2003). However, the characterization flood by rainfall information sometimes is hampered by the limited number of rain gauge. Therefore, combining point measured rain gauge data with spatially distributed rainfall estimation is of great advantage.

Meteorological satellite remote sensing technology plays an important role in providing rainfall information. The global coverage of the satellite makes its suitable for providing data for the regions, which lack rain gauge measurement. Moreover, satellite remote sensing has regular and repetitive data acquisition, which gives an advantage for environmental monitoring purpose.The use of satellite remote sensing is also motivated by the occurrence of devastating hazard, triggered by severe rainfall events such as flash flood. Autoestimator followed by Hydroestimator is geostationary satellite infrared based extreme rainfall algorithm that has been operationally used for flash flood monitoring in the United States (Vicente et al., 1998).

Long-term rainfall record from point measurement by rain gauge is used to describe the frequency distribution of the location of gauge stations. Regional frequency analysis (RFA) such as developed by Hosking and Wallis (Hosking and Wallis, 1997) is mainly used to estimate the regional frequency distribution over a defined region. The appropriate extreme frequency distribution is used to assess the return period of the current extreme event that can be spatially monitored by remote sensing rainfall estimation. Some researchers have been using radar and satellite rainfall information from Tropical Rainfall Measuring Mission (TRMM) (Nobiarto et al., 2003; Edreny et al., 2009; Awadallah et al., 2011). The return period information is very useful for characterizing the severity of extreme event such as storm (Nobiarto et al., 2003).

This chapter deals with the use of observed rainfall long-term historical data for generating regional frequency distribution which is eventually coupled with near-real time geostationary satellite based rainfall estimation for characterizing storm severity. The objectives are threefold:

(i) to estimate storm rainfall by using Multi-functional Transport Satellite (MTSAT) blended with C-band rainfall radar; (ii) to analyze the regional frequency hourly maximum rainfall; (iii) to show the severity of the identified storm rainfall by representing its return period map according to the regional frequency distribution.

## 4.2. STUDY AREA AND DATA

The study area is the whole Japan and its surrounding area where the coordinate boundary is between 30°N to 50°S and 120°E to 150°E (window size 20° × 30°). The time period between June–September 2010 is used in this study.

MTSAT data combined with C-band radar are employed to perform rainfall estimation. MTSAT images of the study area, covering study period were downloaded from website WebGMS-MTSAT/GMS (HIMAWARI) data processing on WWW, Earthquake Research Institute & Institute of Industrial Science, University of Tokyo (http://webgms.iis.u-tokyo.ac.jp).

The rainfall dataset of the same time period was derived from rain gauge as well as C-band radar (4 – 8 GHz frequency) acquired by Automated Meteorological Data Acquisition System (AMeDAS). The temporal resolution of MTSAT and C-band radar is 1 hour and 10 minutes respectively. Figure 4.1 shows the coverage of rainfall estimation by using MTSAT and C-band radar.

For the RFA purpose a long-term record of maximum yearly rainfall data over Hokkaido Island is used. Here, the hourly rainfall data collected from 137 AMeDAS rainfall stations over Hokkaido Island during the period 1980 – 2010 is employed except for year 1989 and 2002 (28 years in total).

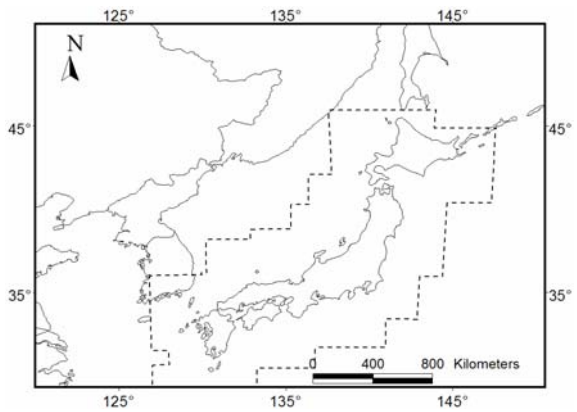


**Figure 4.1.** *The study area shows Japan area and its surrounding. The dashed line is AMeDAS C-band radar network coverage boundary.*

## 4.3. METHODS

The methodology of this study contains two main parts; the first satellite rainfall estimation by using MTSAT satellite datasets and the second regional frequency analysis by using Hosking and Wallis method (1997). Figure 4.2 shows the brief flow chart of the study and next section is the explanation of such diagram.

### 4.3.1. Satellite rainfall estimation

The satellite rainfall estimation by using geostationary satellite is based on an indirect relationship between cloud top temperature depicted by infrared (IR-10.8 µm) channel and rainfall rate (RR) derived by another devices. Misra et. al. uses IR data from Indian Satellite (INSAT-1D) and rainfall intensity form rain gauge measurement to show the IR and RR relationship (Misra et al., 2001).

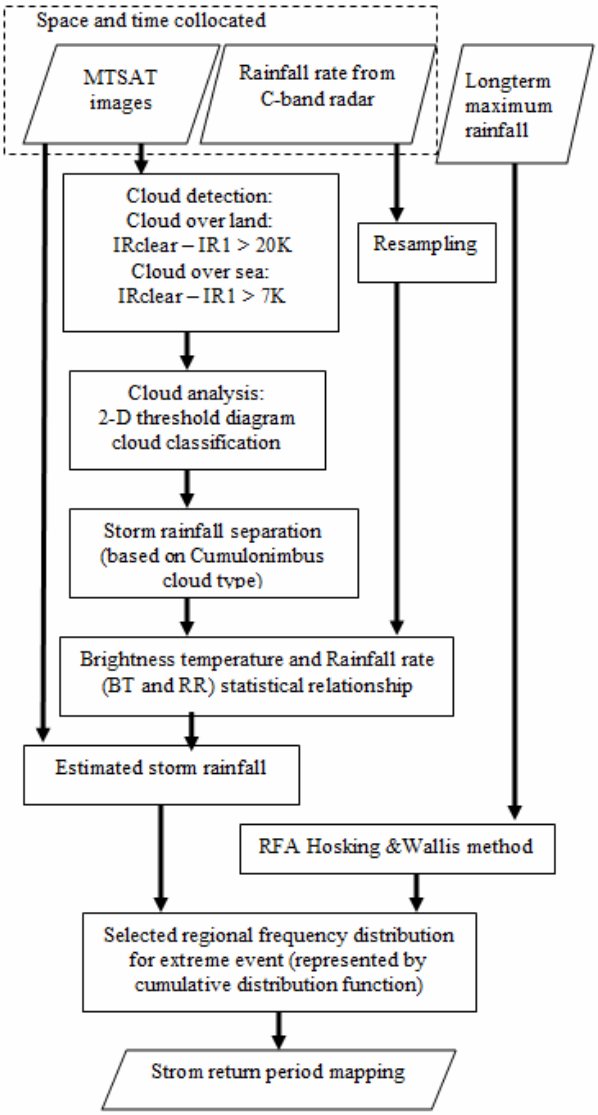


**Figure 4.2.** *MTSAT based rainfall estimation and return period mapping methodology used in this study.*

The combination of IR data from GOES image with rainfall radar is used by Autoestimator for storm rainfall estimation (Vicente et al., 1998). The other research used the combination of both IR and RR from satellite information such as MSG with TRMM (Kinoti et al., 2010). In this study the MTSAT IR channel 1 (IR1) dataset and C-band rainfall radar is used to derive cloud top brightness temperature and rainfall rate information respectively. Furthermore, the cloud type is used as additional information which is included in the rainfall estimation process.

The relation uses an assumption where the colder temperature corresponds to heavier rainfall. However, this assumption is reasonable only for convective cloud type and relatively unreliable for other cloud types such as cirrus (cold but light or no rain) and Stratiform clouds (warm but wet) (Kuligowski, 2003). In this regard, cloud type classification is necessary to be performed to identify the distribution of convective storms rainfall (Suseno and Yamada, 2012b).

The 2-dimensional (2-D) threshold diagram cloud type classification that based on MTSAT split window is used to conduct cloud type classification (Suseno and Yamada, 2012b). The C-band radar information that collocated at the same space and time with MTSAT image had been acquired. Based on collocated MTSAT IR1 and C-band rainfall radar, a pair of brightness temperature and rainfall rate (hereinafter $T_{IR1}$ and RR) dataset can be generated. A regression line can be developed to represent the statistical relationship between $T_{IR1}$ and RR for storm rainfall estimation.

Some pairs of $T_{IR1}$ and RR is developed according to the several storm events during the period of June – September 2010 and draw an average $T_{IR1}$ and RR regression line. The rainfall estimation associated with such statistical relationship then will be validated by using rain gauge measurement. Spatial validation by calculating spatial correlation will be performed for a selected storm event.

### 4.3.2. Regional Frequency Analysis

Frequency analysis is the estimation of how often the specified event will occur. This is a tool for determining design rainfall or design discharge in a certain return period for the purpose of drainage work and structure. In the context of disaster management, frequency analysis is used for assessing the return period of an extreme event. The conventional frequency analysis usually uses data derived from single station (e.g., one rain gauge or one river gauge). If there are many stations which are distributed within a suitably defined region, regional frequency analysis (RFA) should be used instead of the conventional frequency analysis. In this study, the RFA method developed by Hosking and Wallis (hereinafter HW-RFA) is utilized.

The first step of HW-RFA is data screening. The purpose of screening the data is to eliminate the gross error and inconsistencies and to check whether the data are homogeneous (stationary) over time. Generally the hydrometeorological data is available in small size of sample, therefore in HW-RFA the concept of L-moment is introduced. L moment are based on probability-weighted moment (PWM). The rth PWM, βr is defined as

$$\begin{aligned}\beta_r &\equiv E\{X.[F_X(X)]^r\} \\ &= \int_{-\infty}^{\infty} x.[F_x(x)]^r.f_x(x).dx\end{aligned} \tag{4.1}$$

where $F_x$ is cumulative distribution function (CDF) and $f_x$ is probability distribution function (PDF).

The first four moment are computed as

$$\lambda_1 = \beta_0 \tag{4.2}$$

$$\lambda_2 = 2.\beta_1 - \beta_0 \tag{4.3}$$

$$\lambda_3 = 6.\beta_1 - 6.\beta_1 + \beta_0 \tag{4.4}$$

$$\lambda_4 = 20.\beta_3 - 30.\beta_1 + 12.\beta_1 - \beta_0 \tag{4.5}$$

where $\lambda_1$ is the first moment (mean), $\lambda_2$ is the second moment (variance), $\lambda_3$ is the third moment (skewness) and $\lambda_4$ is the fourth moment (kurtosis). Some dimensionless ratios can also be defined as ratio of L-moment that are analogous to the coefficient of variation, skewness and kurtosis as following

$$L-coefficient\ of\ \mathrm{var}iation\ \ (LCv):\ \tau_2 \equiv \frac{\lambda_2}{\lambda_1} \tag{4.6}$$

$$L-coefficient\ of\ skewness\ (LCs):\ \tau_3 \equiv \frac{\lambda_3}{\lambda_2} \tag{4.7}$$

$$L-coefficient\ of\ kurtosis\ (LCk):\ \tau_4 \equiv \frac{\lambda_4}{\lambda_2} \tag{4.8}$$

For screening the data, the discordancy measure ($D_i$) is used. The $D_i$ is defined by:

$$D_i = \frac{1}{3}(u_i - \bar{u})^T S^{-1}(u_i - \bar{u}) \tag{4.9}$$

where $u_i$ is the vector of L-moments i.e. L-coefficient of variation (LCv), L-coefficient of skewness (LCs) and L-coefficient of kurtosis (LCk) for a site *i*. S is defined by

$$S = (N_s - 1)^{-1}\sum_{i=1}^{N_s}(u_i - \bar{u})(u_i - \bar{u})^T \tag{4.10}$$

$$\bar{u} = N_s^{-1}\sum_{i=1}^{N_s} u_i \tag{4.11}$$

where $N_s$ is the number of sites in the group. A site is denoted as discordant if $D_i > 3$.

The next step is the identification of homogeneous region. Homogeneous region is considered as a set of sites whose frequency distributions are considered to be approximately the same. This 'region' is the fundamental unit of RFA. A heterogeneity measured is called H-statistic which is defined as follow

$$H = \frac{(V - \mu_v)}{\sigma_v} \tag{4.12}$$

where $\mu_v$ is mean of simulation, $\sigma_v$ is standard deviation of simulation and V is observed dispersion which are measured as to LCv scatter, LCv-LCs and LCv-LCk, therefore three heterogeneity measures called $H_1$, $H_2$ and $H_3$ that corresponds to LCv scatter, LCv-LCs and LCv-LCk respectively. However $H_1$ is commonly used. In general a region is declared 'acceptably homogeneous' if $H_1 < 1$, 'possibly heterogeneous' if $1 \leq H_1 < 2$, and definitely heterogeneous' if $H_1 > 2$.

An appropriate frequency distribution is chosen by inspecting the goodness of fit between LCk versus LCs for various commonly used distributions duration with the corresponding relation obtained from the at site and regional data. This process is performed by using the Z-statistic as well as graphical method (LCs and LCk diagram).

Once an appropriate frequency distribution is selected, the distribution parameters such as shape, location and scaled can be calculated and the CDF; $F_x$ can be defined. The exceedance probability of an extreme event; x can be calculated based on the CDF and eventually the return period (RP) is calculated as

$$RP = \frac{1}{1 - F_x} \tag{4.13}$$

## 4.4. RESULTS AND DISCUSSIONS

### 4.4.1. Rainfall estimation based on BT and RR statistical relationship

During the period June – September 2010, heavy rainfall event cases was selected by inspecting both rain gauge measurement data as well as MTSAT image to select storm rainfall events. According to the inspection, it was notified that storm events strongly correspond to the

distributed rainfall which is more than 30 mm $h^{-1}$. Based on such criterion, 20 storm events were selected. For each event the $T_{IR1}$ and RR pairs is developed by using MTSAT and C-band radar and draw the statistical regression. In this study a modified exponential model is used to represent the statistical relationship. Furthermore, the events that show strong correlation between $T_{IR1}$ and RR are reselected. Finally 10 storm events that have correlation coefficient ranging from 0.73 – 0.92 are obtained. According to those 10 storm events, an average $T_{IR1}$ and RR relationship is generated by using modified exponential regression model. The model is expressed by the following equation:

$$RR=0.0000061\exp(3052.27/ T_{IR1}) \quad (r^2=0.7) \tag{4.14}$$

where RR is estimated rainfall and $T_{IR1}$ is brightness temperature from MTSAT IR1. Figure 4.3 shows the regression lines of average $T_{IR1}$ and RR relationship as well as the error bars. From that figure, it can be observed that the deviation of rainfall rate became larger for lower cloud top temperature, due to small number of sample in the current event. The average deviation is about 7.7 mm $h^{-1}$, however there are several cases which have quite large deviation. By using the regression equation, the rainfall estimation based on $T_{IR1}$ can be performed. Figure 4.4a shows an example case of rainfall estimation result over Kyushu Island for a rainfall case on 22 June 2010 at 11:30 UTC. A validation has also been conducted by comparing rainfall estimation with measured rainfall over the same time and target region. Some point rain-gauge measurement had been spatially interpolated by using Block Kriging method and the result is presented in Figure 4.4b.

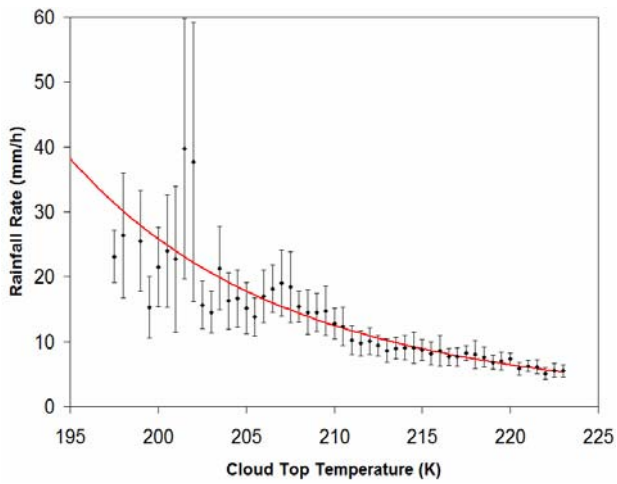


**Figure 4.3.** *Cloud top brightness temperature and rainfall rate statistical relationship of storm rainfall events during June – September 2010 over Japan and its surrounding.*

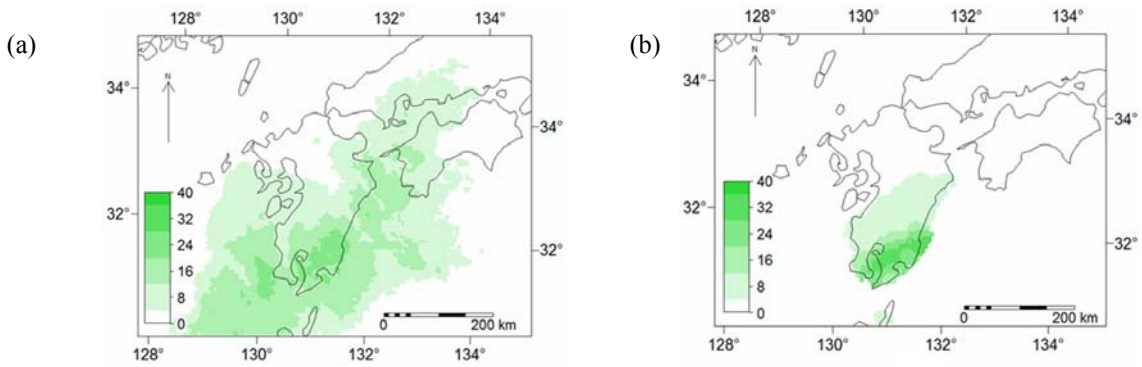


**Figure 4.4.** *(a) Strom rainfall estimation distributions over Kyushu Island on 22 June 2010 at 11:30UTC; (b) rainfall distribution at the same location and time derived by spatial interpolation of point rain gauge measurement.*

Both Figure 4.4a and Figure 4.4b show the comparison of rainfall estimation result with the measured rainfall (for land area). The spatial correlation is 0.79 and it confirms a good agreement between estimated and measured rainfall. Even though according to Figure 4.4a, it can be observed that there are some location in the Kyushu Island where rainfall has been estimated, but actually there are no rain as shown for the same location in Figure 4.4b.

### 4.4.2. RFA of Hokkaido Island

The average value of long-term 1-hour maximum yearly rainfall is calculated for each station. Therefore, these values are interpolated by using inverse distance weight method for Hokkaido Island that is shown in Figure 4.5a.

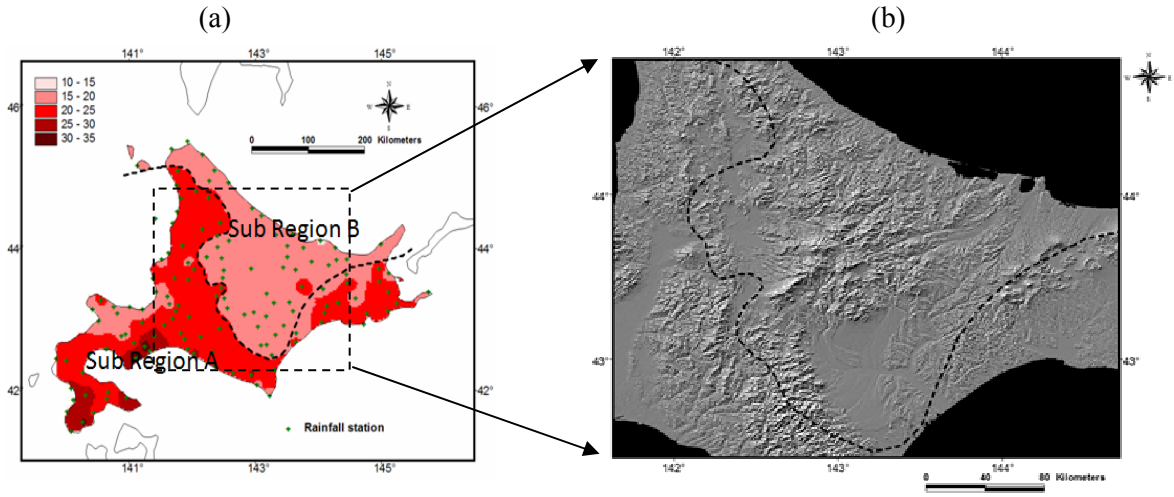


**Figure 4.5.** *(a) Interpolation map of average of long-term maximum yearly rainfall (1-hour duration) by IDW method; (b) shaded relief map represents the topography of Hokkaido Island. The dashed line shows the boundary of the western region (Sub Region A) and eastern region (Sub Region B).*

The distribution of this 1-hour long-term average maximum rainfall seems to be influenced by the topography since the western part has higher maximum rainfall than the eastern part which is clearly divided by the topography (see Figure 4.5b). The western and eastern region is denoted by sub region A and B respectively. These sub-regions are considered as 'the region' for RFA. According to the figure, it is clearly shown that western region (sub region A) of Hokkaido Island is more prone to heavy rainfall that the eastern region (sub region B).

The result of screening data shows that there are 4 and 1 stations in western and eastern region respectively which are discordant (see Figure 4.6). The heterogeneity measure confirms that the $H_1$ –statistic are -1.53 and -1.89 for western and eastern region respectively. Those of $H_1$ values are less than 1 which means both sub regions is acceptably homogeneous.

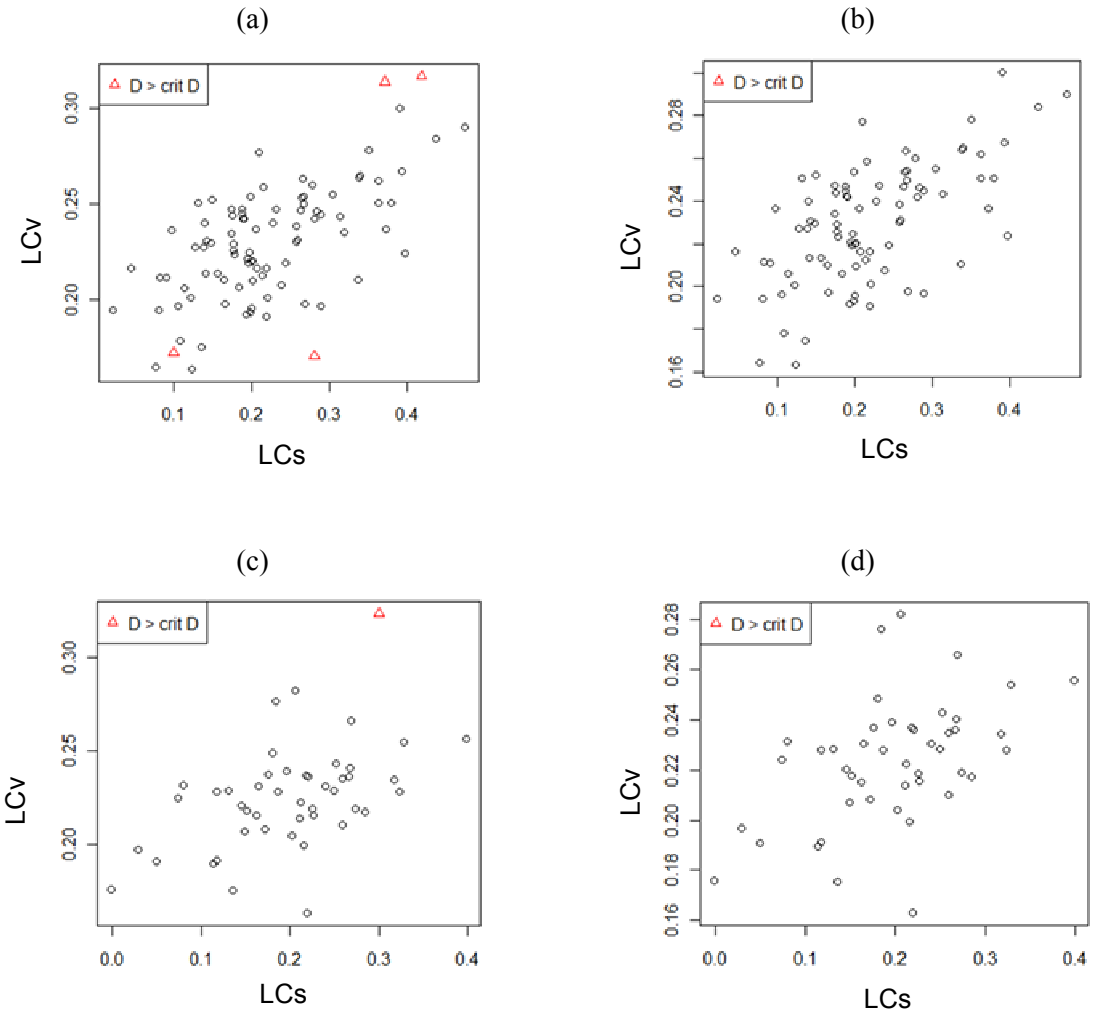


**Figure 4.6.** *(a) and (c) discordancy diagram for western and eastern region respectively which represent discordant stations (D > 3) (denoted by red triangle). (b) and (d) discordancy diagram for western and eastern region respectively after removing discordant stations which are use for determining frequency distribution.*

Choice of frequency distribution is conducted by calculating Z-statistic for five candidate of three parameters frequency distribution i.e. Generalize Logistic (GLO), Generalize Extreme Value (GEV), Generalize Normal (GNO) or Log Normal-three parameters (LN3), Log Pearson III (PE3) and Generalize Pareto (GPA). The Z-statistics value of those frequency distribution for sub region A and B is shown in Table 4.1. Considering the fit of distribution is satisfactory if $|Z| < 1.64$, it confirms that GNO/PE3 distribution is suitable for both region A and B (see the bold value in Table 4.1). Figure 4.7a and Figure 4.7b show the identification of regional frequency distribution using HW-RFA moment ratio LCs/LCk diagram for western and eastern region. The red dots denote the position of the value of regional LCs LCk for the respective regions.

The parameters $\gamma$ (shape), $\mu$ (location), $\sigma$ (scale) of GNO/PE3 distribution are calculated for western and eastern region of Hokkaido Island. The result are -0.45243, 0.91105, 0.37342 and -0.40589, 0.92181, 0.36963 for western and eastern region respectively and those parameters are used to develop CDF as shown in Figure 4.8.

**Table 4.1.** *MTSAT based rainfall estimation and return period mapping methodology used in this study.*

| Frequency Distribution | Sub Region A | Sub Region B |
|---|---|---|
| GLO | 6.10 | 3.56 |
| GEV | 2.10 | 0.34 |
| GNO/LN3 | **0.86** | **-0.35** |
| PE3 | -1.54 | -1.84 |
| GPA | -7.31 | -6.96 |

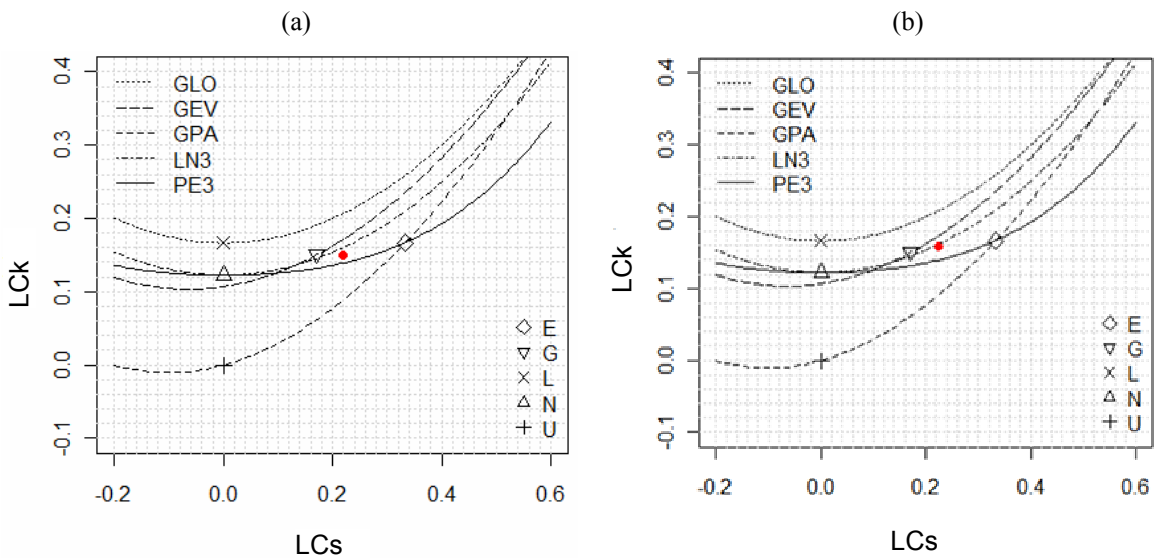


**Figure 4.7.** *Identification of regional frequency distribution using HW-RFA moment ratio LCs LCk diagram for (a) western region and (b) eastern region of Hokkaido Island.*

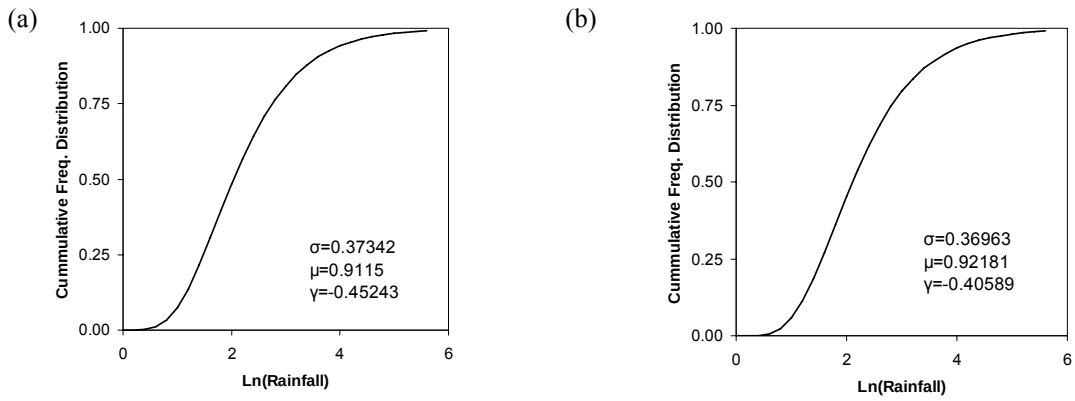


**Figure 4.8.** *Cumulative distribution function of GNO/LN3 distribution for (a) Sub Region A and (b) Sub Region B.*

### 4.4.3. Strom severity characterization by return period mapping

On 23-24 August 2010, it was reported that a storm event attacked the centre of Hokkaido Island from midnight until early morning (Yamada et.al., 2012). The amount of rainfall reported by The Sapporo District Meteorological Observatory is 42 mm $h^{-1}$. The heavy rainfall over Ishikari river basin caused floods and landslides in several places. Two people were reported to have died in this disaster. This rainfall is known as line-shape rain bands (LRB), due to its specific spatial distribution of rainfall which makes an elongated line configuration over certain region Figure 4.9 shows the LRB over Hokkaido island which is configured from 3-hour average rainfall intensity derived by C-band AMeDAS rainfall radar on 24 August 2010 at 01:30 – 04:30 UTC. That figure clearly shows a horizontally elongated rain band in the middle of Hokkaido Island which the heaviest rain is centered on the island.

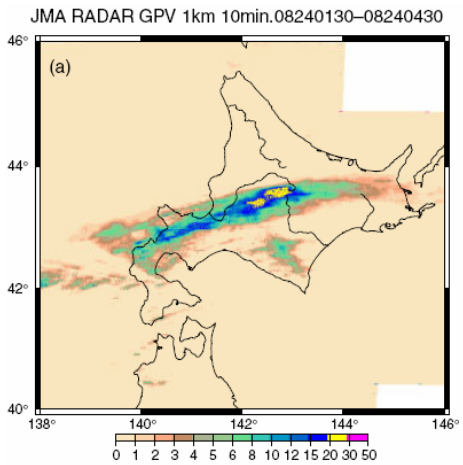


**Figure 4.9.** *Spatial distribution of 3-hour average rainfall intensity (mm/h) from derived from C-band AMeDAS rainfall radar over Hokkaido Island on 24 August 2010 at 01:30 – 04:30 UTC (Yamada et al., 2012).*

(a) (b)

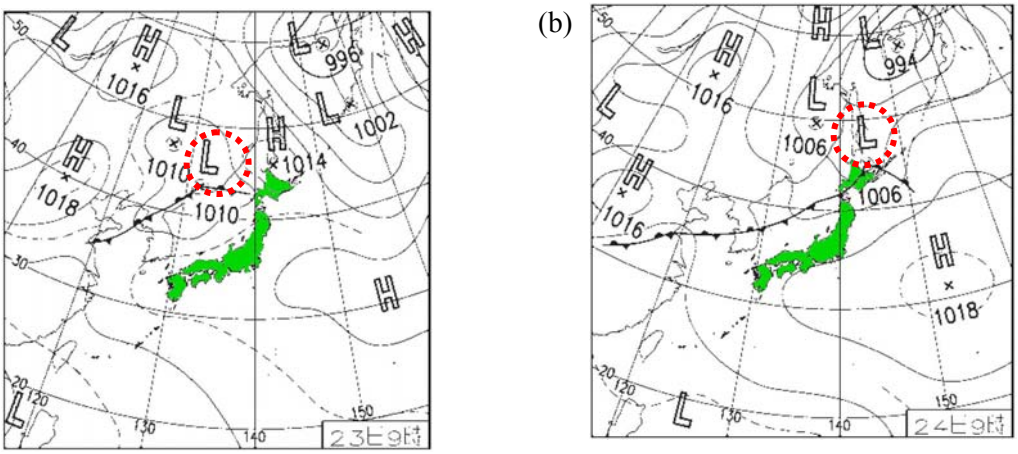


**Figure 4.10.** *Daily weather map that showing frontal system over Japan and its surrounding area on (a) 23 August 2010 and (b) 24 August 2010 (JMA, 2010).*

Figure 4.10 shows the weather chart over Japan and its surrounding area corresponds with the heavy rainfall event over Hokkaido Island during 23 and 24 August 2010. There is a frontal system which cold and warm front occludes. It is caused atmospheric vertical instability that generates some Cb clouds along the frontal line. A low pressure system is also appeared that move toward the northern Hokkaido, caused a severe rainfall in the middle of island.

By using the GNO/LN3 distribution that has already chosen, the return period of such storm can be characterized. Figure 4.11a and 4.11c show spatial distribution of estimated rainfall derived by $T_{IR1}$ and RR relationship and AMeDAS interpolated Hokkaido Island respectively. The highest rainfall estimated over Hokkaido region is about 17 mm $h^{-1}$. Furthermore return period map is generated for this rainfall data, based on the GNO/LN3 cumulative distribution function. The calculated return period for MTSAT estimated rainfall and AMeDAS interpolated rainfall are presented in Figure 4.11b and 4.11d respectively. It shows that the maximum return period for MTSAT estimated rainfall and AMeDAS interpolated rainfall is 5 year and 3 year which corresponds with the maximum estimated rainfall. Though slightly higher, however it suggest that MTSAT rainfall is reasonably feasible for showing the return period information.

The observed rainfall has an advantage of long-term record which is suitable for estimating frequency distribution of extreme events despite they are acquired by relatively uneven station network since the density of station network remain a problem particularly in a remote mountainous region. For assessing the return period of an extreme event in such area, the use of geostationary satellite based is proved useful to overcome such problem. The high repetitive data acquisition is the other advantage of MTSAT which is suitable for monitoring of severity of the rainfall event.

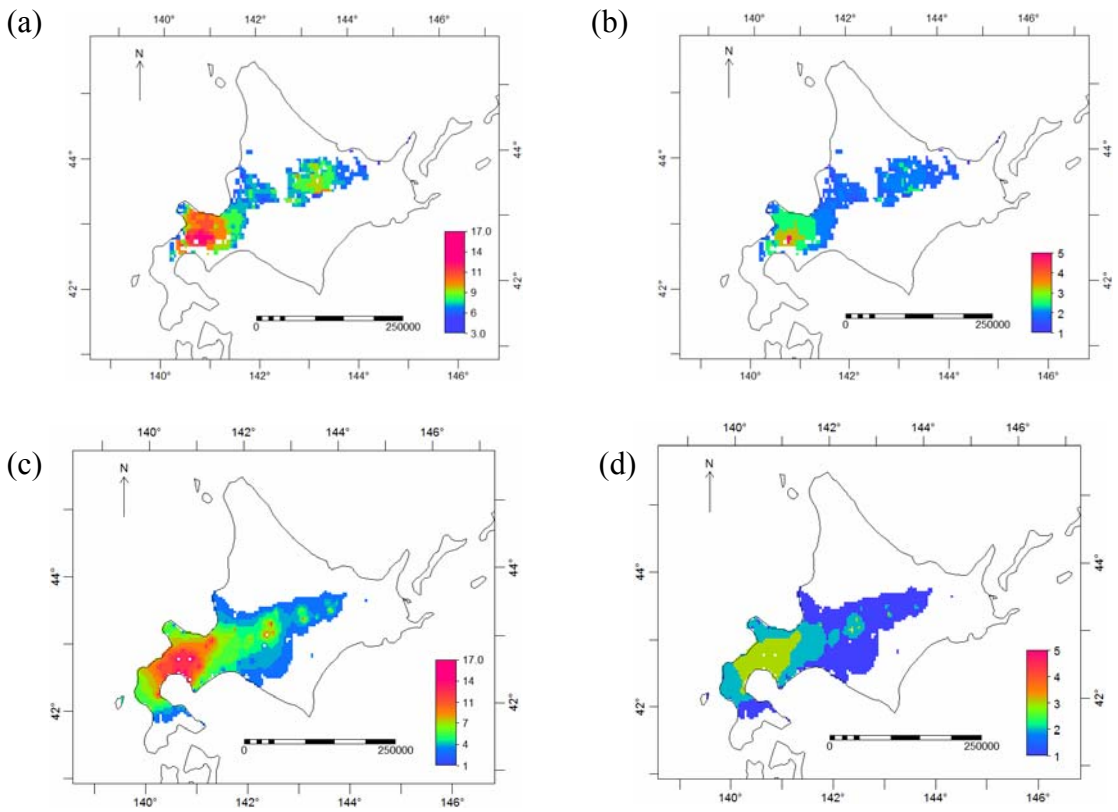


**Figure 4.11.** *(a) MTSAT rainfall estimation over Hokkaido on 23 August 2010 at 20:30UTC (b) return period map (in year) for corresponding storm rainfall event. (c) AMeDAS interpolated rainfall Hokkaido on 23 August 2010 at 20:00UTC (d) return period map (in year) for corresponding storm rainfall event.*

## 4.5. SUMMARY AND CONCLUSIONS

In this study, the rainfall estimation is conducted for Japan area and its surrounding by using $T_{IR1}$ and RR relationship. Those $T_{IR1}$ and RR are derived from MTSAT IR1 and C-band rainfall radar respectively. Storm severity analysis is performed in western part of Hokkaido Island especially during the 23 August 2010 storm event. The $T_{IR1}$ and RR relationship shows the deviation of RR became larger for lower $T_{IR1}$. The average deviation is about 7.7 mm $h^{-1}$, therefore a calibration analysis is need for future work. However a validation over Kyushu Island rainfall case shows promising result.

The RFA result indicates that GNO/LN3 distribution is suitable to describe the frequency distribution of maximum rainfall event in two sub regions in Hokkaido Island. For the heavy rainfall event on 23 August 2010 at 20:30 UTC, it shows that the maximum return period for

MTSAT estimated rainfall and AMeDAS interpolated rainfall is 5 year and 3 year which corresponds with the maximum estimated rainfall.

The observed rainfall has an advantage of long-term record which is suitable for estimating frequency distribution of extreme events despite they are acquired by relatively uneven station network since the density of station network remain a problem particularly in a remote mountainous region. For assessing the return period of an extreme event in such area, the use of geostationary satellite based is proved useful to overcome such problem. The high repetitive data acquisition is the other advantage of MTSAT which is suitable for monitoring of severity of the rainfall event.

# Chapter 5. INTEGRATION OF ATMOSPHERIC ENVIRONMENTAL CONDITIONS INTO GEOSTATIONARY SATELLITE BASED RAINFALL ESTIMATION

---

This chapter is based on: Suseno, Dwi Prabowo Yuga, T. J. Yamada, 2013, **The role of precipitable water vapor and atmospheric stability index in the statistically-based rainfall estimation using MTSAT data**, *Journal of Hydrometeorology* (accepted).

# Abstract

A rainfall estimation method was developed based on the statistical relationships between cloud top temperature and rainfall rates acquired by both the 10.8 μm channel of the Multi-functional Transport Satellite (MTSAT) series and the Automated Meteorological Data Acquisition System (AMeDAS) C-band radar, respectively. The method focused on cumulonimbus (Cb) clouds and was developed in the period of June–September 2010 and 2011, over the landmass of Japan and its surrounding area. Total precipitable water vapor (PWV) and atmospheric vertical instability were considered to represent the atmospheric environmental conditions during the development of statistical models. Validations were performed by comparing the estimated values with the observed rainfall derived from the AMeDAS rain gauge network and the Tropical Rainfall Measuring Mission (TRMM) 3B42 rainfall estimation product. The results demonstrated that the models that considered the combination of total PWV and atmospheric vertical instability were relatively more sensitive to heavy rainfall than were the models that considered no atmospheric environmental conditions. The use of such combined information indicated a reasonable improvement, especially in terms of the correlation between estimated and observed rainfall. Intercomparison results with the TRMM 3B42 confirmed that MTSAT-based rainfall estimations made by considering atmospheric environmental conditions were more accurate for estimating rainfall generated by Cb cloud.


**Keywords:** MTSAT, rainfall estimation, Precipitable Water Vapor, Atmospheric vertical instability

## 5.1. INTRODUCTION

Geostationary satellites make frequent observations with continuous spatial coverage, providing useful information for rainfall monitoring and the early warning of storms (Feidas et al. 2001; Wardah et al. 2003). Thermal infrared data (TIR) centered at 10.8 μm are commonly used to detect cloud top temperature for use in rainfall estimation (Haile et al. 2010). Lower temperatures are assumed to correspond to relatively cold and thick clouds, which tend to produce high rainfall intensity (Kuligowski, 2003). However, clouds are essentially opaque to TIR, which cannot reveal the vertical profile of clouds that produce rainfall. To complement TIR data, microwave (MW)-based rainfall estimations are used, as MW has the ability to penetrate clouds and allows the measurement of aspects of the hydrometeor field. Several well-known algorithms have advantages when using complementary information in TIR and MW data, such as the Precipitation Estimation from Remotely Sensed Information using Artificial Neural Networks (PERSIANN; Sorooshian et al. 2000) and the Tropical Rainfall Measuring Mission (TRMM) 3B42 (Huffman et al. 2007). These products are easily accessible through their dedicated server via the Internet and can be used for water resource management purposes. However, the products are mainly delivered at 0.25° and 3 hourly spatial and temporal resolutions, respectively, which are relatively too coarse for certain hydrological applications such as the detection of flash floods in small ungauged catchments. The aim of this study was to develop a rainfall estimation method based on a combination of TIR and MW that can be applied for the monitoring of flash floods; hence, rainfall information with high temporal resolution is necessary.

To combine TIR and MW for rainfall estimation, a statistical model that represents the relationship between them is commonly implemented (Vicente et al. 1998; Haile et al. 2010; Kinoti et al. 2010). Rainfall estimation using a TIR and MW statistical model as a function of TIR is considered to be suitable for convective clouds, but not suitable for non-convective clouds (Kuligowski 2003). For separating convective and non-convective clouds, cloud classification data should be considered during the development of the TIR and MW statistical model (Suseno and Yamada, 2012b). However, the use of a single statistical model for the estimation of rainfall is limited due to the variety of physical processes associated with rainfall generation, which eventually influence the relationship between cloud top temperature and rainfall rates (Vicente et al. 1998). According to Doswell et al. (1996), deep moist convection normally occurs during the warm season, when high moisture content is possible and buoyant instability promotes strong upward vertical motions. In this study, PWV and atmospheric vertical instability, which are both related to the development of deep convective cloud, were investigated. The objectives of the study were to assess how a combination of total PWV and atmospheric vertical instability conditions improves TIR-based rainfall estimations using a statistical model by focusing on Cb

cloud systems and to validate the estimated rainfall by comparison with observed rainfall during convective storm rainfall events.

## 5.2. STUDY AREA AND MATERIALS

The study area was Japan and its surrounding area between 30–50°N and 120–150°E (window size 20° × 30°). The two time periods examined were June–September of 2010 and 2011. The collocated data pairs (i.e., obtained in the same geographical area during the same time periods) of TIR and MW were used to develop a statistical model for the estimation of rainfall. TIR images were acquired from the Multi-functional Transport Satellite (MTSAT), particularly from the 10.8 μm channel ($T_{IR1}$). The MW-based rainfall rate observations were derived from the Automated Meteorological Data Acquisition System (AMeDAS) C-band radar data (RR). The 12.0-μm MTSAT image channel ($T_{IR2}$) was used in conjunction with $T_{IR1}$ to develop a cloud-type classification system and cloud height images. In the study region, the spatial resolution of MTSAT data was approximately 5 × 5 km. The temporal resolutions of the MTSAT and C-band radar data were 1 hour and 10 minutes, respectively.

Relative humidity derived from rawinsonde data is suitable to represent the moisture factor and was used by Vicente et al. (1998). However, such data have limitations in their spatial and temporal sampling. Therefore, a PWV estimated from ground-based GPS networks to represent the total PWV is used. These data can offer spatiotemporal improvements in moisture observation when compared with radiosonde observations (Iwabuchi et al. 2006). GPS-PWV data are point-based measurements that represent the total atmospheric water vapor contained in a vertical column of unit area. GPS-PWV data have a temporal resolution of 10 minutes and is acquired by more than 1,200 stations giving a mean spacing of about 17 km across the land area of Japan.

To represent atmospheric vertical instability, the Showalter Stability Index (SSI) was used. The SSI is calculated based on vertical temperature profile information provided by a mesoscale model from the Japan Meteorological Agency (JMA; Saito et al. 2006). These data have a 3-hour temporal resolution and are provided at 00, 03, 06, 09, 12, 15, 18, and 21 UTC. The spatial resolution of these data sets is approximately 0.1°.

For validation purposes, the estimated rainfall is compared with hourly AMeDAS observed rainfall data. The TRMM 3B42 rainfall estimation data product (Huffman et al. 2007) that has a spatial and temporal resolution of 0.25° × 0.25° and 3 hours, respectively, was also used as a reference for performing an intercomparison with the rainfall estimation result.

## 5.3. METHODS

### 5.3.1. Parallax correction for geostationary satellite image

To retrieve the rainfall from TIR, statistical relationships between the cloud top temperature and rainfall rates derived from $T_{IR1}$ and RR, respectively, were developed. To determine a collocated data pair between $T_{IR1}$ and RR, because the AMeDAS C-band radar has a 10-minute temporal resolution, instantaneous rainfall data from the 30th minute of the AMeDAS C-band radar were selected. Here, $T_{IR1}$ is only extracted for Cb cloud systems. A cloud classification method developed by Suseno and Yamada (2012b) was employed to discriminate Cb from other cloud types. This cloud classification method uses an upper threshold in two-dimensional spectral spaces ($T_{IR1}$ vs. $\Delta T_{IR1-IR2}$) to define the Cb cloud type, i.e., 2 K for $\Delta T_{IR1-IR2}$ and 225 K for $T_{IR1}$. Consequently the statistical model developed can be used only for $T_{IR1} < 225$ K.

Before developing the statistical relationships, a parallax correction must be performed on the MTSAT images (both $T_{IR1}$ and $T_{IR2}$). The parallax correction procedures used by Vicente et al. (2002) is employed. The principle of this algorithm is to relocate the apparent position of the cloud on the Earth based on the cloud height at its correct geographical location, relative to the MTSAT satellite height and position. The cloud height information was estimated from the MTSAT images according to a method developed by Hamada et al. (2010). The cloud height estimation method also utilized $T_{IR1}$ vs. $\Delta T_{IR1-IR2}$ spectral space, trained by CloudSat. The parallax-corrected MTSAT images that resulted from this process were used to generate further statistical relationships including rainfall retrieval processes.

### 5.3.2. Statistical model development by considering atmospheric conditions

The $T_{IR1}$ and RR statistical relationships differ depending on the availability of precipitable water vapor and the atmospheric vertical instability during the development of convective clouds. Several atmospheric situations were considered to investigate the characteristics of the $T_{IR1}$ and RR statistical relationships: i.e., considering only water vapor availability (PWV); considering only atmospheric vertical instability (SSI); and considering a combination of water vapor availability and atmospheric vertical instability (CMB). The $T_{IR1}$ and RR statistical relationships obtained under these conditions were evaluated by comparing them with the $T_{IR1}$ and RR statistical relationships without considering any atmospheric environmental conditions (ORG).

The $T_{IR1}$ and RR data pairs were acquired from the collocated images to create a modified exponential model, which was formulated as follows:

$$RR = a\, e^{b/T_{IR1}} \tag{5.1}$$

where a and b are the regression coefficients and e is the natural log. The parallax correction described above was performed mainly to define the correct geographic location of the clouds. However, offset errors due to time and navigation differences between MTSAT and AMeDAS C-band radar still remain. Temporal averaging was applied to minimize the effect of such offset errors on rainfall estimation. Temporal averaging was applied to RR for equal $T_{IR1}$ classes with one degree Kelvin intervals. For each $T_{IR1}$ class interval, the RR was averaged and assigned to the corresponding $T_{IR1}$ to match the MTSAT data (Vicente et al. 1998; Kinoti et al. 2010).

Twenty-eight convective systems over the land area of Japan during the period of June–September 2010 and June–August 2011 were recognized by visually inspecting the $T_{IR1}$ image, followed by a cloud classification using the 2D-THR algorithm. Furthermore, the GPS-PWV and SSI that represented the atmospheric environmental situations corresponding with those convective storm events were obtained based on those with the closest acquisition time to the collocated $T_{IR1}$ image. The instantaneous GPS-PWV data at the 30th minute acquisition were chosen, whereas the SSI data at 3-hourly intervals that were the closest to the collocated $T_{IR1}$ image were utilized. A resampling procedure was conducted for GPS-PWV and SSI data using the same georeference as the $T_{IR1}$ image to ensure that the maps spatially matched each other.

The level at which the total PWV as well as atmospheric vertical instability influenced the rainfall intensity to the greatest extent was identified. Figures 5.1a and 5.1b show a frequency histogram of the accumulated number of Cb pixels that produced high rainfall rates (>20 mm $h^{-1}$) against the GPS-PWV and SSI levels, respectively, from the 28 storm cases over the land area of Japan. Two peaks are observed around 55 mm and 61 mm, which are where the highest rainfall intensity occurred under these PWV conditions. A threshold value around 58 mm was determined to separate the PWV condition that most influenced high-intensity rainfall. A similar analysis for SSI was performed to identify the value for which SSI most contributed to high rainfall intensity. Figure 5.1b shows that high rainfall intensity mostly occurred for an SSI around +2. Here, an SSI ≤ +2 is considered to be a relatively unstable condition that produces convective storms. To discriminate atmospheric situations that eventually influence the characteristic $T_{IR1}$ and RR statistical relationships, a value of 58 mm for GPS-PWV and +2 for SSI are proposed as threshold values.

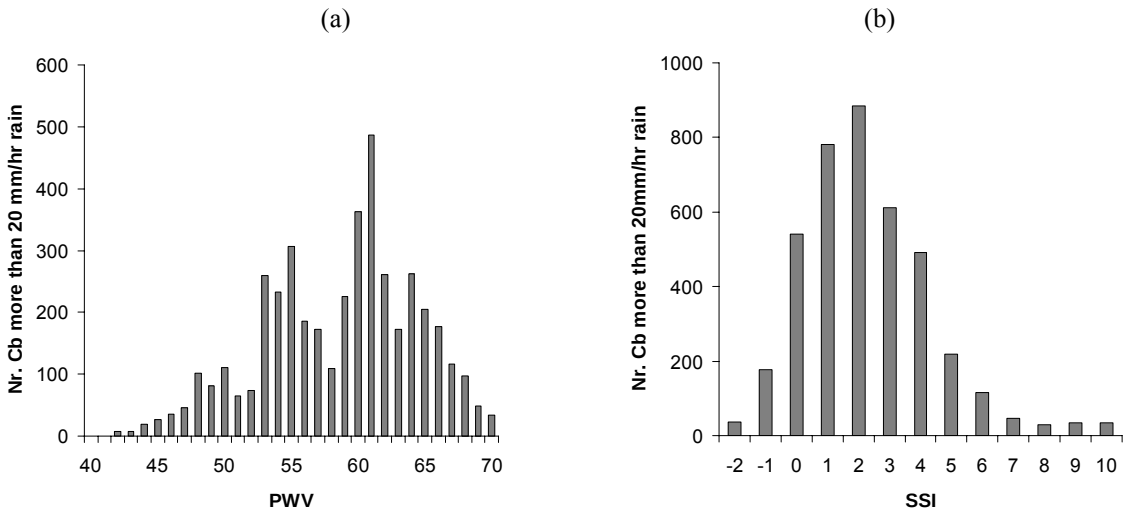


**Figure 5.1.** *Histogram showing the frequency of Cb pixels that produce high rainfall intensity (>20 mm $h^{-1}$) according to (a) GPS-PWV levels and (b) SSI levels.*

Eight modified exponential models were developed according to $T_{IR1}$ and RR data pairs, which were discriminated based on predefined atmospheric environmental situations: i.e., models that consider only PWV and SSI, namely PWV1 (GPS-PWV ≥ 58 mm), PWV2 (GPS-PWV < 58 mm), SSI1 (SSI ≤ +2), and SSI2 (SSI > +2), and models that combine GPS-PWV and SSI, namely CMB1 (GPS-PWV ≥ 58 mm and SSI ≤ +2), CMB2 (GPS-PWV < 58 mm and SSI ≤ +2), CMB3 (GPS-PWV ≥ 58 mm and SSI > +2), and CMB4 (GPS-PWV < 58 mm and SSI > +2). For purposes of comparison, one model (ORG) that did not consider any environmental variable was also generated.

The estimated rainfall was calculated based on $T_{IR1}$ by applying a suitable $T_{IR1}$ and RR statistical model matched with the current atmospheric environmental situation. Rainfall estimations made by considering and not considering atmospheric environmental conditions were measured by comparing them with observed rainfall on a pixel-to-pixel basis in a window box 1°×1° in size. An incompatible spatial domain exists between rainfall observations (obtained as point data) and satellite-based precipitation records (captured as grid data), and therefore, the point-based rainfall observations were transformed into the area domain by using an inverse distance weighting interpolation (Haile 2010). The averaging process during interpolation also minimizes the geolocation error.

The estimation of the rainfall was evaluated by statistical tests, i.e., the correlation coefficient (r), bias and root mean square error (RMSE), which are defined as follows (Ebert 2007):

$$r = \frac{\sum_{i=1}^{N}(E_i - \overline{E})(O_i - \overline{O})}{\sqrt{\sum_{i=1}^{N}(E_i - \overline{E})}\sqrt{\sum_{i=1}^{N}(O_i - \overline{O})}} \qquad \text{(perfect score: 1)} \qquad (5.2)$$

$$\text{Bias} = \frac{1}{N}\sum_{i=1}^{N}(E_i - O_i) \qquad \text{(perfect score: 0)} \qquad (5.3)$$

$$\text{RME} = \sqrt{\frac{1}{N}\sum_{i=1}^{N}(E_i - O_i)^2} \qquad \text{(perfect score: 0)} \qquad (5.4)$$

where $E_i$ and $O_i$ are the estimated and observed rainfall of $i^{th}$ data, $\overline{E}$ and $\overline{O}$ are the average values of the estimated and observed rainfall, and N is the number of data points recorded during the period that a Cb was detected.

An intercomparison between the statistical models and the TRMM 3B42 data sets was also conducted. TRMM 3B42 provides the best estimates of precipitation in each grid box for each observation time (Huffman et al. 2007). Because it was delivered at 3-hour temporal resolution, the instantaneous MTSAT estimated rainfall that was closest to the TRMM 3B42 was chosen for this comparison. A process of resampling into TRMM 3B42 (spatial resolution 0.25° × 0.25°) was performed to ensure that they were spatially comparable to the estimated rainfall data sets. By considering TRMM 3B42, not only convective rainfall but also all other types of rainfall could be observed. The comparison was performed only for the resampled MTSAT pixels that contained 100% Cb cloud type.

## 5.4. RESULTS AND DISCUSSION

An example of $T_{IR1}$ on 29 June 2010 at 01:32 UTC over part of Kyushu Island, Japan (see the box area in Figure 5.2a) before and after parallax correction is shown in Figures 5.2b and 5.2c, respectively. The figures represent the distribution of cloud top temperature values, while the white gaps in between the pixels in the parallax corrected image represent the distance of cloud displacement. The collocated AMeDAS C-band radar data (black dots) are overlaid onto them. The $T_{IR1}$ before the parallax correction (see the dashed yellow area in Figure 5.2b) indicates the presence of some relatively warmer cloud pixels that correspond with relatively high rainfall rates (denoted by relatively larger black dots).

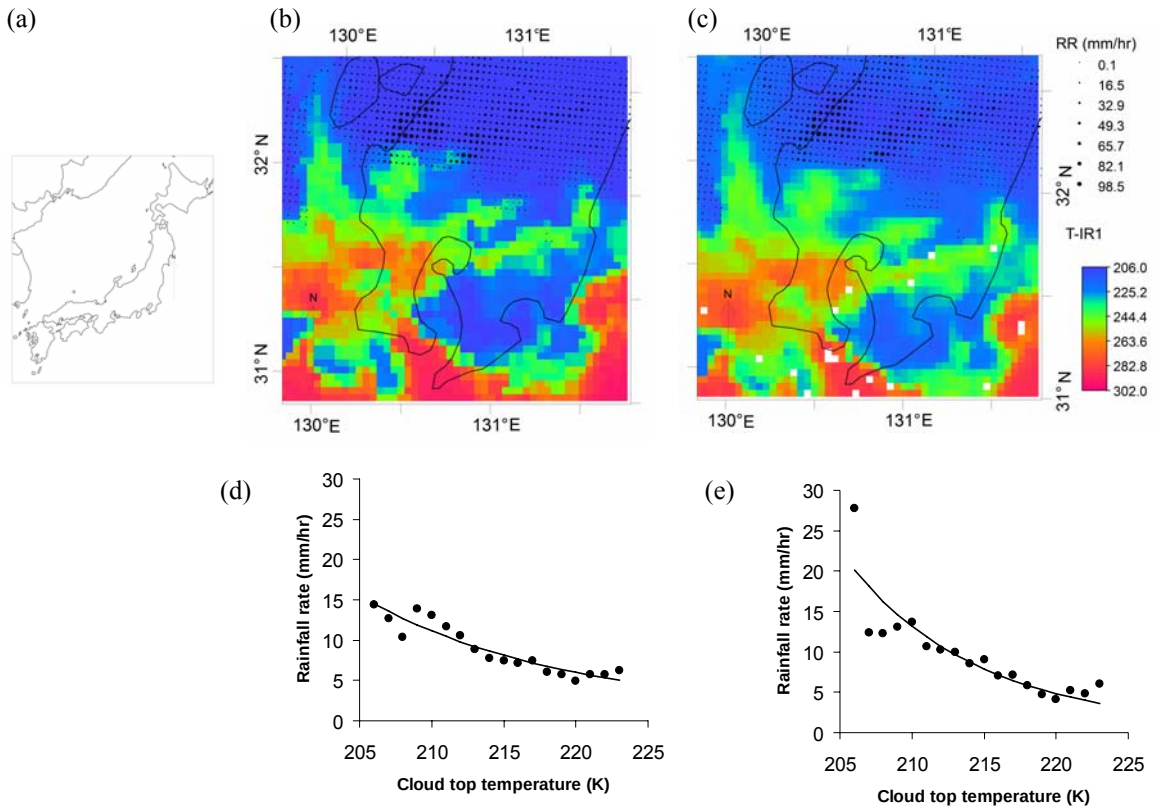


**Figure 5.2.** *(a) An example of the parallax correction on MTSAT IR1 data over part of Kyushu Island, Japan, from 29 June 2010 at 01:32 UTC, (b) a MTSAT IR1 image before parallax correction, and (c) a MTSAT IR1 image after parallax correction. The small black dots over the images are rainfall rates observed by AMeDAS C-band radar. The graphs under the figures represent the statistical relationship of cloud top temperature and rainfall rates used to produce the collocated MTSAT IR1 images and C-band radar rainfall rate values (d) before and (e) after parallax correction.*

Furthermore, after applying the parallax correction (see the dashed yellow area in Figure 5.2c), the location of these warm pixels is shifted and replaced by the adjacent colder pixels. Those colder cloud pixels are closely matched with the corresponding high rainfall rates. This confirms the assumption that the lowest cloud top temperature is associated with higher rainfall rates. This is also indicated by the statistical relationship between $T_{IR1}$ before and after the parallax correction with RR, as shown in Figures 5.2d and 5.2e, respectively. Although these figures confirm the assumption, the image without the parallax correction fails to capture relatively high rainfall rates that should correspond with lower cloud top temperatures.

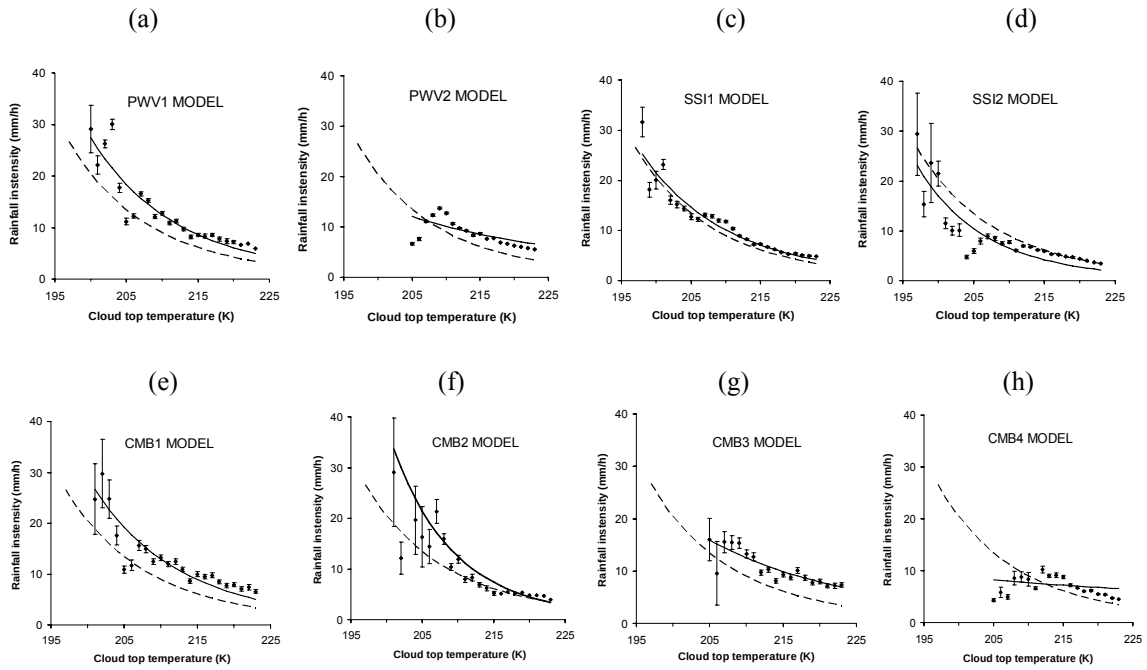


**Figure 5.3.** *The modified exponential regression models corresponding to different atmospheric environmental conditions: (a) PWV1, (b) PWV2, (c) SSI1, (d) SSI2, (e) CMB1, (f) CMB2, (g) CMB3, and (h) CMB4 (solid line) compared to the model without considering atmospheric environmental conditions (ORG; dashed line).*

Figure 5.3a to 5.3h show modified exponential regression curves for different atmospheric environmental conditions. The regression line obtained by the model that considers total PWV or atmospheric vertical instability as well as their combination (solid line) is plotted together with the model without considering atmospheric conditions (dashed line). The scattered points shown in Figure 5.3a to 5.3h are the average rainfall rates for every 1 K cloud top temperature interval. The error bar for each point represents the 95% confidence interval (CI) which is estimated using

$$\mathrm{CI} = \overline{\mathrm{R}} \pm \left(1.96 \frac{\sigma}{\sqrt{\mathrm{n}}}\right) \tag{5.5}$$

where $\overline{\mathrm{R}}$ and $\sigma$ are the mean and standard deviation of the C-band radar rainfall rates at each 1-K temperature interval, respectively, and n is the number of data points at each temperature interval (Haile 2010). The confidence intervals become relatively wider for low cloud top temperature values. Wider confidence intervals are most probably due to rare storm events that correspond to low cloud top temperature during the study periods. This situation produces only a few data points for lower cloud top temperature values compared with the higher temperature values.

According to Figure 5.3a, a high rainfall rate can be produced only by relatively high PWV conditions (≥58 mm) at $T_{IR1}$ around 200 K. For the relatively low PWV conditions (<58 mm) shown in Figure 5.3b, the model can only estimate a lower rainfall intensity up to a cloud top temperature around 205 K. This implies that total PWV contributes strongly to the generation of high rainfall rates.

Figure 5.3c and 5.3d show the regression curves generated by relatively unstable (SSI < +2) and stable (SSI > +2) atmospheric situations, respectively. Both regression curves almost coincide with the regression curve for the situation without consideration of atmospheric conditions. However, by examining Figure 5.3d more carefully, it can be seen that some heavy rainfall events occur under relatively stable atmospheric conditions. Even though the number of such events is small (indicated by the wide confidence interval), they influence the shape of the regression line. One of the reasons for this condition is the limitations in spatial and temporal resolution of SSI. A relatively coarse spatial resolution would lead to an SSI that does not adequately separate the high and low rainfall rates corresponding to the atmospheric vertical instability conditions. A low temporal resolution results in spatial shifting between rainfall and the SSI because of the time discrepancy during data acquisition. Figure 3e to 3h show the regression curves for the situation where total PWV and atmospheric vertical instability are combined. The figures indicate that the specific situation for combined total PWV and atmospheric vertical instability can be represented by different regression curves.

Before moving to the next stage (i.e., to measure the performance of MTSAT rainfall estimation by comparing the results with observed rainfall), a cross-correlation analysis was conducted to determine the lag time between them. The grid values at the coordinate locations of station no.74181 (33°33’59”N and 133°32’48”E) and station no. 87321(32°13’52”N and 131°9’2”E) were extracted from hourly estimated and observed rainfall data during the period of 16–20 September 2011. Figure 5.4a and 5.4b show the cross-correlograms of estimated rainfall (colored bars) and observed rainfall for both locations. These figures indicate a 1-hour time lag between estimated and observed rainfall, which implies that the rainfall detected by satellite could be observed as real rainfall by a rain gauge after 1 hour.

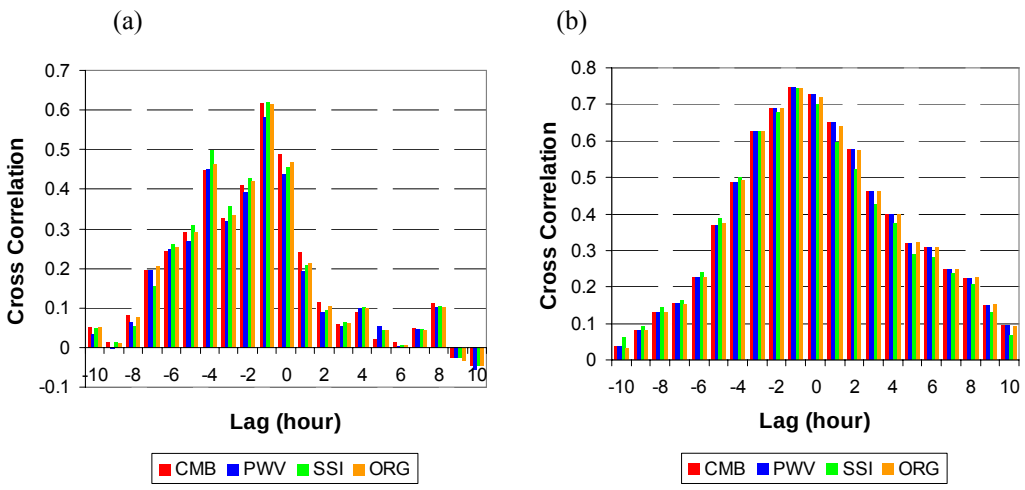


**Figure 5.4.** *Cross-correlograms of estimated and observed rainfall for (a) station no. 74181 and (b) station no. 87321. In both cases, the maximum correlation occurs at a time lag of negative 1-hour.*

The performance of the statistical models was tested in three case studies: (1) 22 June 2010 at 06:30–13:30 UTC over Kyushu Island (beginning of summer; hereinafter case A); (2) 24 August 2011 at 15:32–21:32 UTC over Nara Prefecture (middle of summer; hereinafter case B); and (3) 19–20 September 2011 at 17:32–05:32 UTC over Kyushu Island (end of summer; hereinafter case C). The locations of these three case studies are shown in Figure 5.5a.

To show the difference among statistical models, a snapshot of the rainfall during the peak of a heavy rainfall event on 22 June 2010 at 11:30 UTC over Kyushu Island Japan (case A) was estimated using the model without consideration of any atmospheric conditions (Figure 5.5b), the model considering only PWV (Figure 5.5c), the model considering only SSI (Figure 5.5d), and the model considering both PWV and SSI (Figure 5.5e). As explained above, there was a 1-hour time lag between estimated rainfall and observed rainfall; therefore, the estimated rainfall results were compared with interpolated observed rainfall (Figure 5.5f) for the following hour (i.e., 12:30 UTC). Compared with the observed rainfall, MTSAT rainfall estimations did not represent local strong rainfall events very well, even though in the wider spatial domain, they provided a reasonable representation of the spatial distribution of rainfall.

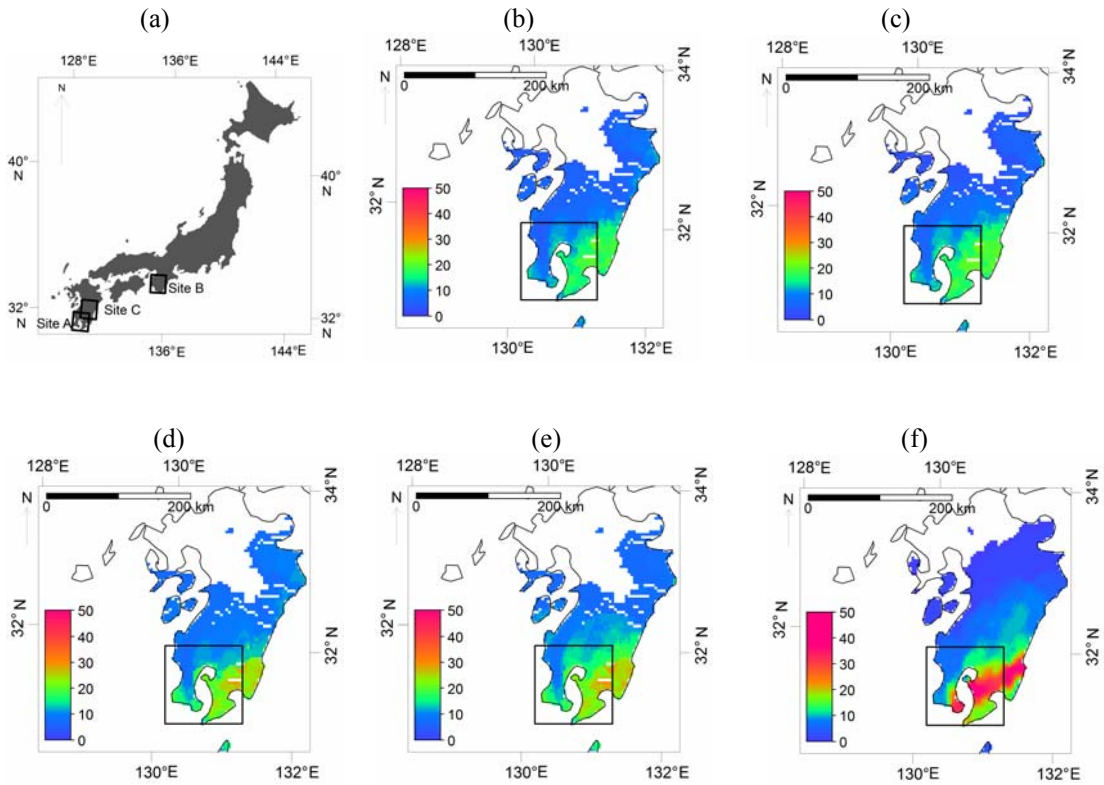


**Figure 5.5.** *(a) Location of case studies. Snapshoot of heavy rainfall event distribution from 22 June 2010 at 11:30 UTC over Kyushu Island, Japan; (b) Estimated rainfall without considering atmospheric environmental condition (ORG); (c) considering only atmospheric vertical instability (SSI); (d) considering only precipitable water vapor(PWV); (e) considering both atmospheric vertical instability and precipitable water vapor (CMB); and (f) observed rainfall (OBS).*

This situation is confirmed by Figure 5.6a– 5.6d, which show 1-hourly scatterplots of observed rainfall vs. MTSAT rainfall estimations without considering the atmospheric environmental conditions, considering only the PWV, considering only the SSI, and considering both PWV and SSI for case A. For rainfall >30 mm $h^{-1}$, MTSAT rainfall estimations fail to represent such high rainfall rates. However, compared with the ORG model, a consideration of the atmospheric environmental information, particularly the combination of SSI and PWV, could enhance the estimated rainfall. It can be seen in Figure 5.6a, 5.6e, and 5.6i that the maximum estimated rainfall is around 20 mm h-1. Therefore it can be increased up to around 25 mm h-1, as shown by Figure 5.6d, 5.6h, and 5.6l. This indicates that the use of combinations of atmospheric conditions is more sensitive for detecting the high rainfall rates produced by low cloud top temperatures.

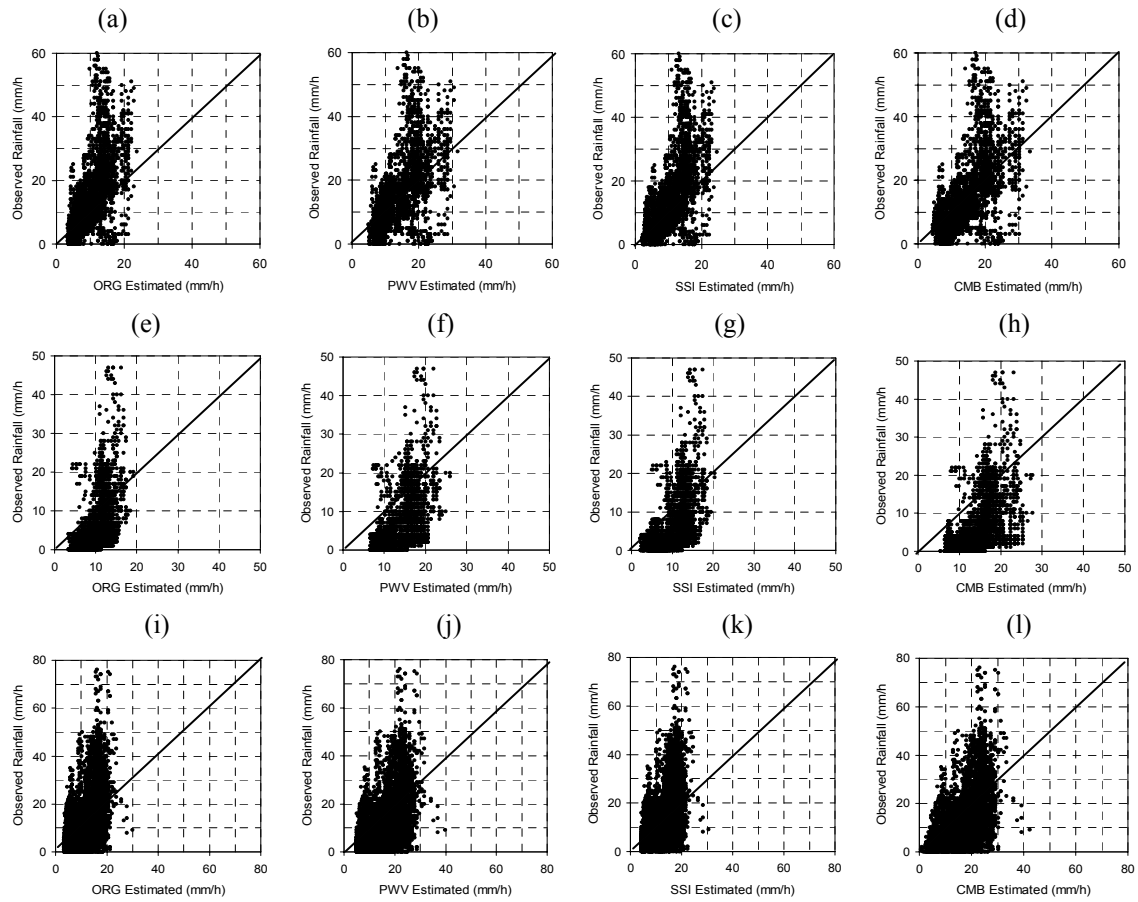


**Figure 5.6.** *Scatterplot of 1-hourly observed rainfall vs. MTSAT rainfall estimation without considering atmospheric environmental condition ((a),(e),(i)), considering only PWV ((b),(f),(j)), considering only SSI ((c),(g),(k)), and considering both PWV and SSI ((d),(h),(l)), for case A ((a) – (d)), case B ((e) – (h)), and case C ((i) – (l)).*

Table 5.1 describes the statistical performance between the model considering atmospheric environmental conditions and the model that does not consider the atmospheric environmental conditions. The figures were calculated by considering the 1-hour time lag between the estimated and observed rainfall. The table indicates that in terms of bias and RMSE, the use of atmospheric environmental conditions for rainfall estimation does not produce a meaningful improvement when compared to the model that does not consider any atmospheric environmental conditions. However, the model that considers the combination of total PWV and atmospheric vertical instability demonstrates a reasonable improvement in terms of correlation. This improvement in performance in terms of correlation supported the observation that combinations of parameters are more sensitive in detecting high rainfall rates produced by low cloud top temperatures, as explained in the paragraph above.

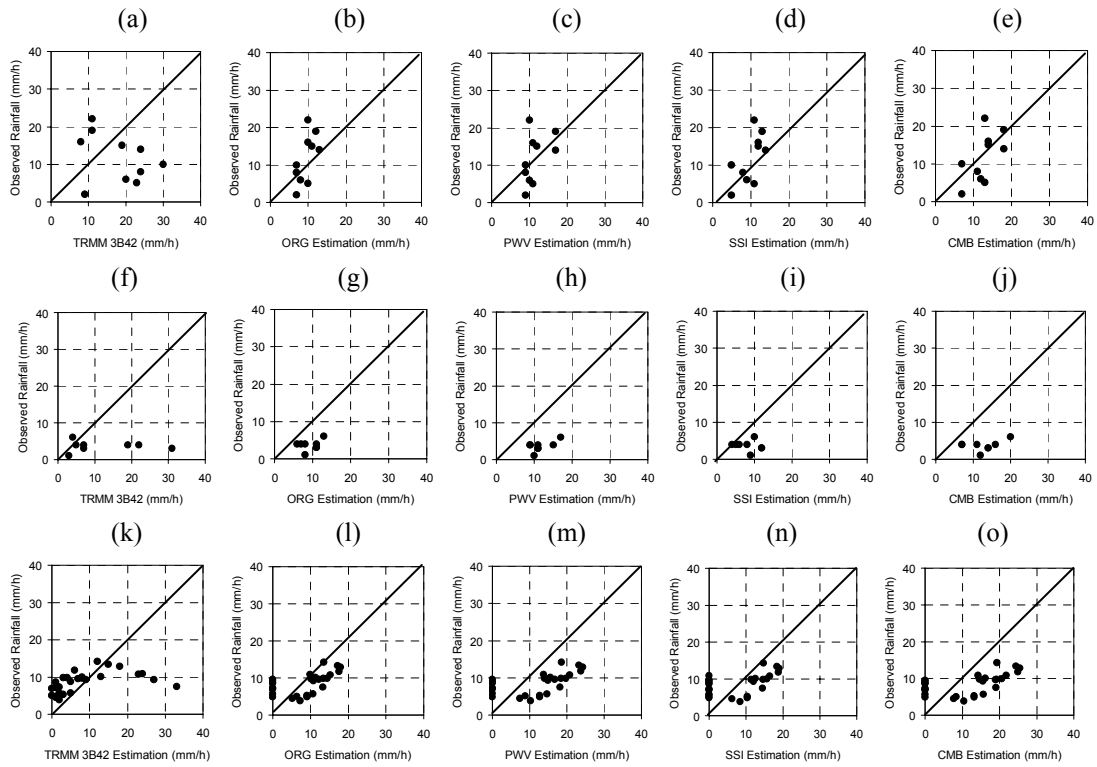


**Figure 5.7.** *Scatterplot of 3-hourly observed rainfall vs. TRMM 3B42 ((a),(f),(k)), MTSAT rainfall estimation without considering atmospheric environmental condition ((b),(g),(l)), considering only PWV ((c),(h),(m)), considering only SSI ((d),(i),(n)), and considering both PWV and SSI ((e),(j),(o)), for case A ((a) – (e)), case B ((f) – (j)), and case C ((k) – (o)).*

The results of an intercomparison between the MTSAT rainfall estimation and the TRMM 3B42 data product for cases A, B, and C is presented in Figures 5.7(a)–(e), 7(f)–(j)) and 5.7(k)–(o), respectively. Their statistical performance is described in Table 5.2. As shown in Figure 5.7a, 5.7f, and 5.7k, the scatterplots indicate that the TRMM 3B42 data product was more scattered than MTSAT rainfall estimations for case A and was overestimated to a larger extent for cases B and C. These conditions were confirmed by the lower correlations than those for the MTSAT rainfall estimations (see Table 5.2). The bias and RMSE of TRMM 3B42 are also larger than the MTSAT rainfall estimations, except for case C. These results suggest that MTSAT rainfall estimations perform better than the TRMM 3B42 data product.

***Table 5.1.*** *Comparison of $T_{IR1}$ and RR statistical model by considering total PWV and atmospheric vertical instability (CMB, PWV and SSI) and the model without considering total PWV and atmospheric vertical instability (ORG) for case A, case B and case C. Bold-faced numbers show best statistical results.*

| | Case A | | | | Case B | | | | Case C | | | |
|---|---|---|---|---|---|---|---|---|---|---|---|---|
| | Sample Size | Cor | Bias (mm $h^{-1}$) | RMS (mm $h^{-1}$) | Sample Size | Cor | Bias (mm $h^{-1}$) | RMS (mm $h^{-1}$) | Sample Size | Cor | Bias (mm $h^{-1}$) | RMS (mm $h^{-1}$) |
| CMB | 3588 | **0.66** | 1.0 | **8.6** | 4758 | 0.54 | 7.8 | 9.4 | 8975 | 0.54 | 4.6 | 9.9 |
| PWV | 3588 | **0.66** | **0.2** | **8.6** | 4758 | 0.51 | 4.7 | **7.0** | 10484 | 0.51 | 5.7 | 10.8 |
| SSI | 3588 | 0.65 | -2.4 | 9.2 | 4758 | **0.61** | 7.3 | 8.7 | 8475 | **0.61** | 0.9 | **8.9** |
| ORG | 3588 | 0.65 | -3.0 | 9.5 | 4758 | 0.48 | **5.0** | 7.2 | 10484 | 0.51 | **0.8** | 9.5 |

***Table 5.2.*** *Comparison of MTSAT IR1 based rainfall estimation both considering and without considering total PWV and atmospheric vertical instability and TRMM 3B42 rainfall estimation product for case A, case B and case C. MTSAT-CMB, MTSAT-PWV and MTSAT-SSI respectively refers to MTSAT IR1 based rainfall estimation by considering combination of PWV and SSI, PWV only and SSI only. MTSAT-ORG refers to MTSAT IR1 based rainfall estimation without considering any atmospheric environmental condition. Bold-faced numbers show best statistical results.*

| | Case A | | | | Case B | | | | Case C | | | |
|---|---|---|---|---|---|---|---|---|---|---|---|---|
| | Sample Size | Cor | Bias (mm $h^{-1}$) | RMS (mm $h^{-1}$) | Sample Size | Cor | Bias (mm $h^{-1}$) | RMS (mm $h^{-1}$) | Sample Size | Cor | Bias (mm $h^{-1}$) | RMS (mm $h^{-1}$) |
| MTSAT-CMB | 10 | 0.62 | 1.0 | 5.0 | 8 | 0.32 | 9.0 | 9.8 | 28 | **0.55** | 3.1 | 8.4 |
| MTSAT-PWV | 10 | 0.48 | **-0.2** | 5.4 | 8 | **0.60** | 8.0 | 8.3 | 28 | 0.54 | 2.6 | 7.8 |
| MTSAT-SSI | 10 | **0.65** | -1.7 | **5.1** | 8 | -0.21 | **4.6** | **5.7** | 28 | 0.52 | -1.2 | 6.4 |
| MTSAT-ORG | 10 | 0.64 | -2.2 | 5.6 | 8 | 0.34 | 5.8 | 6.2 | 28 | **0.55** | -0.4 | **-5.3** |
| TRMM 3B42 | 10 | -0.33 | 6.2 | 12.6 | 8 | -0.02 | 8.6 | 13.1 | 28 | 0.51 | **-0.1** | 7.8 |

## 5.5. SUMMARY AND CONCLUSIONS

A method of rainfall estimation based on the statistical relationships between $T_{IR1}$ and RR was developed for heavy rainfall generated by convective cloud in Japan and the surrounding area. $T_{IR1}$ and RR data were acquired from MTSAT IR1 and AMeDAS C-band radar, respectively, for the periods of June–September 2010 and 2011. A parallax error correction was performed for the MTSAT data sets. To differentiate between convective and non-convective cloud, the 2D-THR cloud classification algorithm was applied to the parallax-corrected MTSAT data sets. The total PWV and atmospheric vertical instability conditions during the convection process, which influence the $T_{IR1}$ and RR statistical relationships, were investigated. These atmospheric environmental conditions were represented by GPS-PWV and SSI, respectively. Values of 58 mm for GPS-PWV and +2 for SSI were proposed as thresholds for discriminating such atmospheric environmental conditions. Eight modified exponential models were developed according to $T_{IR1}$ and RR data pairs, which were discriminated based on predefined atmospheric environmental situations: i.e., models that considered only PWV and SSI, namely PWV1 (GPS-PWV ≥ 58 mm), PWV2 (GPS-PWV < 58 mm), SSI1 (SSI ≤ +2), and SSI2 (SSI > +2), and models that combined GPS-PWV and SSI, namely CMB1 (GPS-PWV ≥ 58 mm and SSI ≤ +2), CMB2 (GPS-PWV < 58 mm and SSI ≤ +2), CMB3 (GPS-PWV ≥ 58 mm and SSI > +2), and CMB4 (GPS-PWV < 58 mm and SSI > +2). One model, namely ORG, which did not consider GPS-PWV and SSI, was also generated.

Several different regression curves for the statistical relationships of $T_{IR1}$ and RR were produced, especially by combining PWV and SSI conditions. Due to the occurrence of rare storm events that corresponded to low cloud top temperatures during this study period, the confidence intervals of the statistical model became relatively wider for low cloud top temperature values. Based on those regression curves the rainfall estimation is conducted based on cloud top temperature by considering specific atmospheric environmental conditions.

When compared with the model that did not consider any atmospheric environmental conditions, the use of atmospheric environmental conditions for making rainfall estimations enhanced the accuracy of rainfall estimation, particularly when using the model that considered a combination of total PWV and atmospheric vertical instability, and eventually improved the performance, particularly in terms of correlation. However MTSAT rainfall estimation was not successful in representing local heavy rainfall events, even though it performed reasonably well when predicting the rainfall spatial distribution at a wider spatial domain.

The intercomparison results between MTSAT IR1-based rainfall estimations and the TRMM 3B42 data product demonstrated that MTSAT IR1-based rainfall estimations either considering or not considering total PWV and atmospheric vertical instability, produced a reasonably better performance than the TRMM 3B42 data product.

Because of the limitation of the number of samples that were used in this study, the full variety of physical processes associated with convective rainfall generation may not have been included. Therefore, more samples should be included in the development and validation of statistical models to reach a more definite conclusion.

# Chapter 6. EMPIRICAL REGRESSION BASED RAINFALL-RUNOFF MODEL FOR FLASH FLOODS SEVERITY ASSESSMENT

---

Prepared for publication

# Abstract

Flash floods are one of the most dangerous hazards that are difficult to forecast. Therefore, identification of flash flood prone catchments is important for their risk reduction and mitigation. The catchments that potential in producing flash floods are represented by their relative flash flood severity. Flash floods are considered severe when they have relative high magnitude and high rising hydrograph gradient. This study intends to use some hydrological, morphometrical and meteorological factors to characterize flash flood severity and develop some empirical models to draw the relationship among them. 16 gauged sub-catchments in western Hokkaido region have been delineated. The highest discharge within June to October in each year that has time to peak discharge less than 12 hours is identified and selected as the flash flood event during the period of 1998 – 2009. The flash floods severity is analyzed for each sub-catchments based on hydrograph analysis. The hydrological, morphometrical and meteorological condition of those catchments are identified. The step-wise multiple regression analysis demonstrates that the land use contributing area is dominant factor related to flash flood severity in Ishikari river basin, particularly under initially wet soil moisture condition. For the morphometrical parameters the prominent parameters are those related to basin shape (i.e. elongation ratio) and topography (i.e. relief ratio and melton's ruggedness number). For the meteorological parameter, the rainfall intensity is utilized to assess the flash flood severity. The implementation of the empirical models at Toyohira basin shows that FI as the function of morphometrical factors can provide flash flood potential information. Moreover, FI as the function of hydrological and meteorological factors demonstrate more dynamic pattern since they are related to rainfall intensity distribution.


**Key Words:** Flash flood, severity index, multiple regression analysis

## 6.1. INTRODUCTION

The sudden and destructive nature of flash floods make they considered as one of the most dangerous hazards. The flash floods, when compared to normal floods are characterized by quite rapid rises and falls with little or no advance warning. These types of floods are resulted from very intense rainfall over a relatively small area (NRC, 2005). Flash floods are also difficult to forecast because the task is not only to forecast the occurrence of the events but also their magnitude should be anticipated (Doswell et al., 1996).

Several efforts to reduce the flash floods risk is by identifying the potential of flash floods occurrence in particular ungauged catchments have been performed by some researchers. Yousef et al. (2010) was conducting a morphometrical analysis to estimate flash flood risk levels in an arid environment. Angilierri (2010) also analyze various morphometrical characteristic over some catchments area in order to evaluate flash flood hazard. Both studies have made use some sources of spatial data which are mainly derived from topographic map and satellite imagery to identify the morphological features. The results of those studies show that they can initiate appropriate measures to mitigate the potential hazard in the area.

In this study, flash floods is considered as the output of a catchment system that are determined by not only by hydraulic processes related to the morphology of stream but also meteorological and hydrological factor such as slope, land use, geology (NRC, 2005). The flash floods are mostly triggered by severe convective storm that typically developed under unstable atmospheric condition, modulated by the hydrological condition and sometimes amplified by the catchment's morphology and network structure. Because flash floods are resulted as the response of the catchments to the rainfall that is controlled by the hydrological and morphologic factors, thus they can be used as the proxies to determined flash flood hazard potential.

Beven and Kirkby (1979) mentioned that for the humid and temperate basin, the runoff generation mechanism is mainly influenced by: (i) rainfall intensity that exceed infiltration or storage capacity on a variable area; and (ii) rainfall that directly fall in channel and completely saturated soil. In this study the variable area that contributes to runoff is assumed to influence the flash flood severity index. A combined various land surface condition (i.e. land use, surface permeability and slope steepness) and rainfall intensity in a catchment is considered as variable contributing area. The soil saturation condition is identified according to initial soil moisture condition by using simple water balance calculation.

The catchments that potential in producing flash floods can be represented by their relative flash flood severity index. Hydrograph analysis approach is usually used to identify the flash flood severity (Bashkar et al., 2000; Kim et al., 2001, 2012). Flash floods are considered severe when they have relative high magnitude and high rising hydrograph gradient. Since the flash flood severity index is mainly characterized by hydrograph analysis, consequently this analysis only applicable for the gauged catchments. On the other hands, many of catchments are still ungauged especially which those are situated in remote mountainous region.

This research intends to use some hydrological, morphometrical and meteorological factors to characterize flash flood severity. By understanding the relationship between those factors and flash flood severity, an empirical model can be developed and utilized to assess the flash flood severity in ungauged catchment. Therefore, the objectives of this study include (i) to characterize some hydrological, morphometrical and meteorological factors of the catchment (hereinafter hydro-morpho-meteorological) that influence the flash flood severity index; (ii) to evaluate the hydrological variable contributing area related to flash flood severity index by considering initial soil moisture condition; (iii) to develop a statistical model, that can be used to predict relative severity of flash flood in ungauged catchments.

## 6.2. THE STUDY AREA AND DATASETS

The study area is western Hokkaido region (the grey shaded area in Figure 6.1a), which is separated from the eastern part of the island by mountainous range. According to regional frequency analysis both areas have homogenous characteristic in term of the distribution of long-term average hourly maximum rainfall. However, the western Hokkaido region is more prone for rainfall triggered hazards since it has higher long-term average hourly maximum rainfall that ranging from 15–35 mm $hr^{-1}$ (Suseno and Yamada, 2012a).

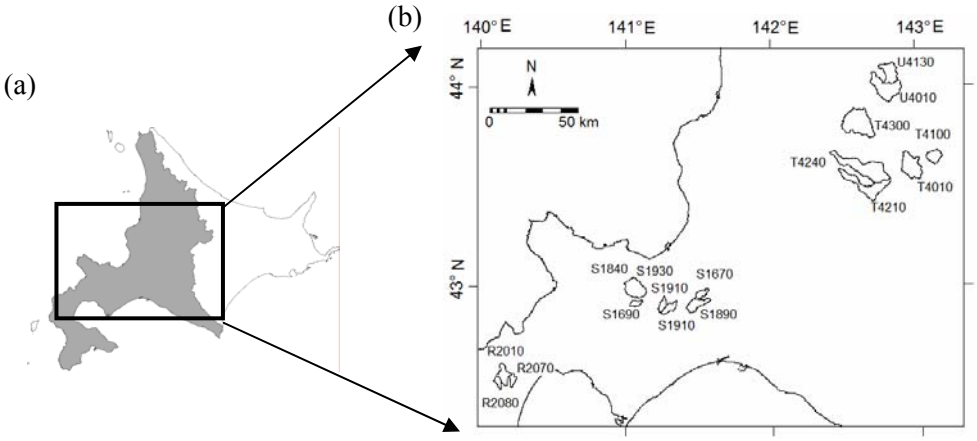


**Figure 6.1.** *(a) Western Hokkaido region (grey-shaded area) as the study area; (b) locations of selected 16 catchments in the study area.*

This area is mostly dominated by sedimentary rocks and volcanic rocks. Sedimentary rock includes mudstone, alteration mudstone and sandstone, gravel, sand and clay. The volcanic rocks generally consist of andesitic rocks, volcanic breccia and tuff breccia. The terrain of study area is characterized mainly by small relief mountain, rugged mountain, flat alluvial valley, large undulating hill. The dominant land use in the western Hokkaido region is forest, agricultural land including paddy fields, wasteland and settlements.

The DEM is used for terrain analysis, automatic catchment delineation and morphometrical parameters extraction. Some hydrological parameters of the catchments such as landuse and geology are derived from thematic maps provided by National Land Numerical Information, Ministry of Land, Infrastructure, Transport and Tourism (MLIT) (http://nlftp.mlit.go.jp/ksj-e/index.html). The rainfall and discharge data are retrieved from Water Information System of MLIT (www1.river.go.jp).

## 6.3. METHODS

### 6.3.1. Flash flood severity identification

Bhaskar et. al. proposed the flash flood severity using flash flood index that is calculated based on some characteristics of observed hydrograph such as the rising curve gradient (K), the flood magnitude ratio (M) and flood response time (T) (Bhaskar et al., 2000). A relative severity factors RK, RM and RT of those respective parameters then quantified as an ordinal score. The relative severity, RF is defined as the average of those three relative parameters. This method then modified by Kim and Choi (2011; 2012) that used rainfall-runoff model output instead of observed hydrograph. Since RK and RT represent similar characteristic which is shorter flood response time can be associated with steep rising of flood hydrograph, so they only consider RK and RM for calculating RF. Below is some equations used for quantifying flash flood severity used by Bhaskar et.al and Kim and Choi, which used in this study. The observed hydrograph is analyzed to identify hydrograph parameters, K and M. However, a modification is also made which is instead of using long-term average of discharge as proposed by Bhaskar et.al, the initial discharge, $Q_o$ for calculating M is used.

$$K = \frac{\ln(Q_p / Q_o)}{T} \tag{6.1}$$

$$RK = \frac{K_i}{K_{\max}} \tag{6.2}$$

$$M = \frac{Q_p}{Q_o} \tag{6.3}$$

$$RM = \frac{M_i}{M_{\max}} \tag{6.4}$$

$$FI = \frac{RK + RM}{2} \tag{6.5}$$

where $Q_p$, $Q_o$: peak and initial discharge; T: time to peak; RK: relative rising curve gradient; $K_i$: rising curve gradient for flood event –i; $K_{max}$: maximum rising curve gradient. RM: relative flood magnitude; $M_i$ : flood magnitude for flood event –i; $M_{max}$ : maximum flood magnitude; FI : flash flood severity index.

### 6.3.2. Hydrological Characterization

The hydrological characteristics of the catchments determine the way of interaction between the rainfall and land surface. They can direct the rainwater into the soil layer or let them run off the surface (Seyhan, 1976; NRC, 2005). In this study, several hydrological parameters of the catchments are considered i.e. slope steepness, aspect of catchment, surface permeability and landuse. However for the purpose for characterizing the hydrological factors related to flash flood severity, the soil moisture condition is also taking into account.

The estimation of soil moisture condition is following the method proposed by Yamada which is performed by plotting total rainfall vs. total loss rainfall for some flood events (Kure and Yamada, 2004). A simplified hydrological water balance such as introduced by Viessman et al. (1972) can utilized to calculate the total loss rainfall, which is defined by

$$P - R = \Delta S \tag{6.6}$$

where, P is rainfall, R is surface runoff and ΔS is storage which refers to surface or sub surface storage. For a short-term water balance system such as hourly time scale, the storage can be considered as soil moisture. In this study the term of “total rainfall loss” is used instead of soil moisture storage since it calculated by subtracting direct runoff depth from the rainfall. Both rainfall and direct runoff depth can be derived from rain gauge and river gauge observation respectively. The direct runoff depth is derived by using base flow separation technique from the stream flow hydrograph. A scatter plot is drawn from total rainfall loss which is associated with total rainfall in the same rainfall event. By using this scatter plot the initial soil moisture condition can be identified. For the same amount of total rainfall the soil moisture is considered initially wet when the total rainfall loss is smaller than that initially dry soil moisture condition. It is because it is assumed that in the initially dry soil moisture condition the soil moisture capacity become larger so as to more total rainfall become loss (infiltrated or evapotranspirated).

The concept of variable contributing area proposed by Betson (1964, as cited in Beven and Kirkby (1979)) mentioned that runoff will be produced when the rainfall exceed infiltration or soil storage on variable area of near-saturated soil. This situation makes the infiltration capacity and soil moisture status is vary in horizontal distribution, and caused downslope flow of water. However, in this study a different approach is used to define the variable contributing area. Here some land surface parameter of catchment which is assumed to be closed related to the infiltration is considered i.e. land use, rock permeability and slope steepness. The rock type is considered to be used instead of soil type due to the lack of information of soil physical properties such as soil texture. However the approach of using rock type to measure the surface permeability is also used by Seyhan (1976). The spatial distribution of saturation area is always vary depends on the land surface condition of the catchment and rainfall distribution.

For characterizing the area contribution of particular land surface parameter, the following procedure is performed. Firstly, the current land surface parameter is overlaid with rainfall map to obtain the N number of unit contributing area. Moreover, the total contributing area for land surface parameter is calculated by using the following equation

$$Ls = \sum_{i=1}^{N} Sc_i \left( \frac{I_i A_i}{\max(I_i A_i)} \right) \tag{6.7}$$

where, Ls is total land surface contributing area for particular catchment area. $Sc_i$, is relative score to runoff. $I_i$ is rainfall intensity and $A_i$ is area. The subscript i denotes the unit contributing area. The geographic information system (GIS) analysis is employed for extracting those of hydrological characteristics for every catchment area.

The relative score of land use, rock type and slope steepness is proposed for Hokkaido region such as shown in Table 6.1, 6.2 and 6.3 respectively. Table 6.1 shows a reclassification rock types based on their permeability. The rock type that relatively impermeable is assumed to produce more runoff and assigned with higher score than those high permeability rock. The rock type reclassification due to its relative permeability is following the guidance provided by Lewis et al. (2006). The reclassification of land use which is shown in Table 6.2 is mainly based on relative vegetation cover, that dense vegetation such as forest assume to produce less runoff than sparse or un-vegetated area such as bare land or transportation land. In this case forest has relatively lower score than bare land or transportation land. Similar logic is used for assigning the score for surface slope such as shown in Table 6.3, that steep slope which is assumed to produce more runoff has higher score than gentle slope

**Table 6.1**. *Score of rock type according to their relative surface permeability*

| Rock Type | Score |
|---|---|
| Phorphyry, Granite, Gabbro, Serpentine, Diabase, Hornfield, Gneiss, Crystaline Schist | 5 |
| Ryolitic rock, Andesitic rock, Basaltic Rock, Pumice, Volcanic Breccia, Tuff Breccia | 4 |
| Rock Tuff, Volcanic ash, Volcanic clastic materials, Clay | 3 |
| Alteration sandstone and mudstone, sandstone, mudstone, quartzite rock, slate, loam | 2 |
| Gravel, Sand, Clastic, Peat | 1 |

**Table 6.2**. *Score of land use type according to their relative vegetation cover*

| Land use type | Score |
|---|---|
| Bare land, transportation | 5 |
| Settlement | 4 |
| Other agricultural land | 3 |
| Other land (mixed garden) | 2 |
| Forest, beach, golf course, paddy field | 1 |

**Table 6.3**. *Score of slope class according to their relative steepness*

| Slope class | Score |
|---|---|
| > 40% | 5 |
| 25 - 40% | 4 |
| 15 – 25% | 3 |
| 8 – 15% | 2 |
| < 8% | 1 |

### 6.3.3. Morphometrical Characterization

Parts of rainwater that is not infiltrated into soil layer then running off hill slope and finally reach the channel. In this case, the morphometry of the catchments and their network structure modulate the velocity of the water flowing through the channel and eventually influence the timing of flood response to rainfall input. The morphometrical parameters that have been considered in this study are describing the basin shape (i.e. circularity ratio, elongation ratio basin mean width), the basin topography (i.e. basin relief, relief ratio and melton's rudgeddness number) and the stream network structure (i.e. drainage density and bifurcation ratio). The summary of those morphometrical parameters are shown in Table 6.4. (Seyhan, 1976; Perucha and Angilieri, 2010).

**Table 6.4**. *The morphometrical parameters used in this study.*

| Morphometrical characteristics of catchment | Equation | Purpose | |
|---|---|---|---|
| Circularity ratio (dimensionless) | $Rc = 4\pi A / P^2$ | To measure the degree of circularity of the catchment. Rc > 0.5 the catchment shape tends to circle, Rc < 0.5 tends to be non-circular | (6.8) |
| Elongation Ratio (dimensionless) | $\mathrm{Re} = 1.129(\sqrt{A} / L)$ | To measure the shape of the catchment, related to main channel length. Re = 1 the shape of catchment is circular, Re < 1 the shape of catchment is about an ellipse with main channel tends to be parallel with major axis, Re > 1 the shape of catchment is about an ellipse with main channel tends to be parallel with minor axis. | (6.9) |
| Basin Mean width (L) | $Wm = A / L$ | To measure the average width of catchment | (6.10) |
| Basin relief (L) | $Hr = H - h$ | To measure the height difference between outlet and maximum height in the catchment perimeter | (6.11) |
| Relief Ratio (dimensionless) | $Rr = Hr / L$ | To measure the average gradient of catchment | (6.12) |
| Melton's Ruggedness Number (dimensionless) | $MRN = Hr / \sqrt{A}$ | To measure the average topographical roughness of catchment | (6.13) |
| Drainage Density ($L/L^2$) | $Dd = L_{ct} / A$ | To measure the density of stream network of the catchment | (6.14) |
| Weighted Bifurcation Ratio (dimensionless) | $Wrb = \frac{\sum_{i=1}^{n} Rb_{i/i+1}(N_i + N_{i+1})}{\sum_{i=1}^{n} N_i}$ while $Rb_{i/i+1} = N_i / N_{i+1}$ | To measure the degree of bifurcation of stream network. Highly bifurcated means that the lower stream receives more water from the upper stream network. | (6.15) |

Note: An area of the catchment; P: perimeter of the catchment; L: straight length of the channel; H,h: maximum and minimum height; $L_{ct}$: total stream length; $L_{cp}$: main stream length; N: number of stream segment of given order.

### 6.3.4. Catchments Meteorology Characterization

The extreme rainfall event as the input for flash flood is characterized. Here the rainfall is not only described by their intensity but also its variability. The index of rainfall location that is quantifies the location of storms independent of intrastorm spatial variability of precipitation had been used in this study (Smith et al., 2004). This index shows the gridded rainfall centroid ratio i.e.:

$$I_{pcp} = C_{pcp} / C_{bsn} \tag{6.16}$$

The $C_{pcp}$ is calculated by the following equation:

$$C_{pcp} = \sum_{i=1}^{N} P_i A_i L_i \Big/ \sum_{i=1}^{N} P_i A_i \tag{6.17}$$

The $C_{bsn}$ is the catchment centroid that is calculated by the same way as Equation 6.16 except that $P_i = 1$. $L_i$ is the Euclidean distance between location of grid-i and location of the outlet. $A_i$ is area of grid. N is total number of grid within the catchment. When the $I_{pcp} < 1$ means that the heavier rainfall is generally located at the area closer to the catchment's outlet. The value near to 1 indicates that that rainfall is concentrated near to the catchment's outlet. In addition, if the value is more than 1, it is imply that the heavier rainfall is away from the outlet.

### 6.3.5. Multiple regression analysis

The reason of the use multiple regression analysis in this study is that most of the phenomena in hydrology are the product of multiple causal (Seyhan, 1976). A multiple regression can draw the effect of causals (independent variables) upon the phenomenon (dependent variable) by providing equation for estimating the individual values of phenomenon from the given values of causals. In this study the phenomenon is flash flood severity. The flash flood severity of certain catchment area is explained by some hydro-morpho-meteorological variables, according to the following equation (Rogerson, 2006):

$$\hat{y} = a + b_1 x_1 + b_2 x_2 + \ldots + b_p x_p \tag{6.18}$$

where is the predicted flash flood severity, $x_1$, $x_2$,…,$x_p$ are hydro-morpho-meteorological variables with p variables and a, $b_1$, $b_2$,…,$b_p$ are the regression coefficients.

For selecting which variables that significantly influence the flash flood severity, a step-wise multiple regression analysis is applied. Here, the variable that is most highly correlated with dependent variable is entered first. Then, the other variable is added. The significance of the earlier added variable is re-checked every time the new variable is added and will be removed if they are not still significant (Rogerson, 2006).

## 6.4. RESULTS AND DISCUSSIONS

### 6.4.1. Flash flood severity analysis

The 16 gauged catchments are selected for flash flood severity analysis. The catchments have the area ranging from 16.1–200.8 $km^2$ and their distribution is shown in Figure 6.1b. The gauged catchments that have relatively long period rainfall and discharge records are selected.

The length of records (N) is ranging from 7 – 12 years that mainly observed during 1998 to 2010 periods. The highest discharge within June to October in each year that has time to peak discharge less than 12 hours is identified and selected as the flash flood event. Those of flash flood events are mostly took place in August or September. The FI is calculated for every flash flood events. The flood severity analysis of the 16 catchments as the average of FI is summarized in Table 6.5. The calculation results shows that for RK average, RM average and FI average are ranging from 0.32 to 0.68; 0.33 to 0.59 and 0.35 to 0.58 respectively.

**Table 6.5.** *Summary of FI calculation in 16 catchments.*

| River Name | Catchment code | Average RK | Average RM | FI average | Year period | N |
|---|---|---|---|---|---|---|
| Upper Toyohira | S1690 | 0.56 | 0.47 | 0.52 | 2001-2010 | 10 |
| Shirakawa | S1930 | 0.45 | 0.48 | 0.47 | 2001-2010 | 8 |
| Wattsu | S1670 | 0.33 | 0.36 | 0.35 | 2001-2009 | 9 |
| Makomanaigawa | S1910 | 0.42 | 0.41 | 0.41 | 2001-2010 | 9 |
| Shimamatsugawa | S1890 | 0.4 | 0.58 | 0.49 | 2001-2010 | 9 |
| Shirai | S1840 | 0.41 | 0.59 | 0.5 | 2001-2010 | 10 |
| Chuusibetsu | R2080 | 0.36 | 0.59 | 0.48 | 1998-2009 | 12 |
| Pirikabetsu | R2070 | 0.57 | 0.51 | 0.54 | 1998-2008 | 11 |
| Shiribeshitoshibetsugawa | R2010 | 0.43 | 0.34 | 0.38 | 1998-2008 | 11 |
| Rubeshinai | T4100 | 0.4 | 0.47 | 0.44 | 1998-2009 | 12 |
| Upper Ishikari | T4010 | 0.6 | 0.56 | 0.58 | 1998-2009 | 12 |
| Beiegawa | T4210 | 0.68 | 0.43 | 0.44 | 1998-2009 | 11 |
| Bebetsugawa | T4240 | 0.32 | 0.38 | 0.35 | 1998-2009 | 12 |
| Upper Teshio | U4130 | 0.43 | 0.38 | 0.41 | 1998-2007 | 10 |
| Teshio | U4010 | 0.5 | 0.33 | 0.41 | 1998-2009 | 12 |
| Ushisubetsugawa | T4300 | 0.5 | 0.59 | 0.54 | 2002-2008 | 7 |

### 6.4.2. Morphometrical characteristics

The morphometrical characteristics of 16 catchments are presented in Table 6.6. The logical relationship between morphometrical characteristics values with FI is evaluated. For example more circular shape of catchments (Rc approaching to 1) should correspond to higher FI, because time concentration of rainfall become flood is almost similar from every part of catchment. Similarly higher drainage density should be positive relation with FI since the rainfall become easier to be collected by stream network and eventually become flood. Among eight morphometrical parameter evaluated in this study, there are only 5 parameters found which have logical relationship with the FI average, i.e. Circularity ratio (Rc), Elongation ratio (Re), Form factor (Ff), Basin mean width (Wm), Relief ratio (Rr) and Melton's Ruggedness Number (MRN) such as shown in Figure 6.2.

The results suggest that the morphometrical parameters of catchment that influence the flash flood are mainly related to the shape and topographical characteristics. The stream network characteristics such as drainage density and bifurcation ratio seems does not show a prominent influence.

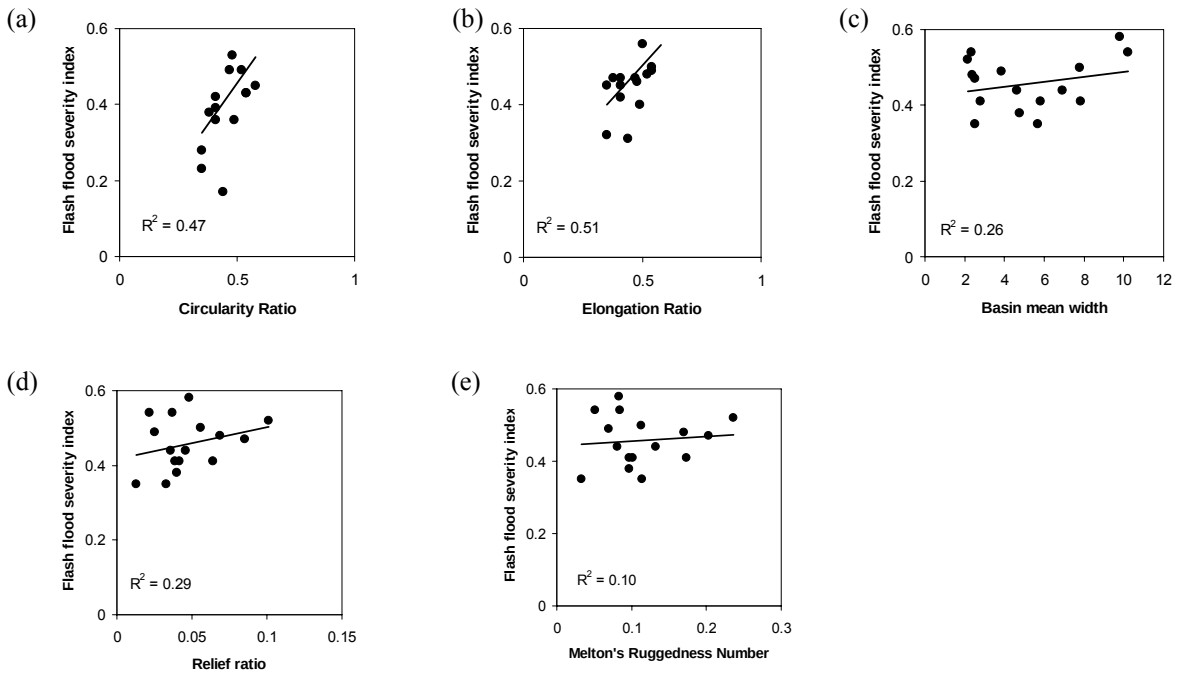


**Figure 6.2.** *Relationships between FI and (a) circularity ratio; (b)form factor; (c) basin width; (d) relief ratio and (e) Melton's ruggedness number for 16 catchment areas in Ishikari basin and its surrounding area.*

**Table 6.6.** *Morphometrical parameters determined in 16 catchments (no unit means dimensionless parameters).*

| River name | Catchment code | P (km) | A ($km^2$) | Rc | Re | S | Wm (km) | Hr (m) | Rr | MRN | Dd ($km/km^2$) | WRb |
|---|---|---|---|---|---|---|---|---|---|---|---|---|
| Upper Toyohira | S1690 | 20.83 | 17.05 | 0.49 | 0.48 | 1.23 | 2.17 | 973 | 0.101 | 0.236 | 2.15 | 4.81 |
| Shirakawa | S1930 | 23.93 | 22.27 | 0.49 | 0.47 | 1.27 | 2.51 | 956 | 0.085 | 0.203 | 2.04 | 6.04 |
| Wattsu | S1670 | 32.90 | 24.19 | 0.28 | 0.45 | 1.28 | 2.52 | 163 | 0.013 | 0.033 | 2.36 | 5.90 |
| Makomanaigawa | S1910 | 33.06 | 31.35 | 0.36 | 0.42 | 1.34 | 2.78 | 969 | 0.064 | 0.173 | 2.32 | 5.37 |
| Shimamatsugawa | S1890 | 42.63 | 52.09 | 0.36 | 0.40 | 1.49 | 3.83 | 503 | 0.025 | 0.070 | 2.41 | 5.68 |
| Shirai | S1840 | 42.60 | 91.40 | 0.63 | 0.56 | 1.64 | 7.78 | 1076 | 0.056 | 0.113 | 2.10 | 5.60 |
| Chuusibetsu | R2080 | 19.60 | 16.10 | 0.53 | 0.46 | 1.45 | 2.37 | 683 | 0.069 | 0.170 | 2.04 | 5.10 |
| Pirikabetsu | R2070 | 22.80 | 17.80 | 0.43 | 0.50 | 1.25 | 2.32 | 354 | 0.037 | 0.084 | 2.18 | 5.00 |
| Shiribeshitoshibetsugawa | R2010 | 39.90 | 48.50 | 0.38 | 0.47 | 1.65 | 4.77 | 674 | 0.040 | 0.097 | 2.07 | 5.60 |
| Rubeshinai | T4100 | 29.70 | 45.40 | 0.65 | 0.65 | 1.78 | 6.91 | 544 | 0.046 | 0.081 | 2.08 | 5.90 |
| Upper Ishikari | T4010 | 56.30 | 113.00 | 0.45 | 0.65 | 1.61 | 9.79 | 885 | 0.048 | 0.083 | 2.16 | 5.70 |
| Beiegawa | T4210 | 97.40 | 131.50 | 0.17 | 0.31 | 1.47 | 4.63 | 1509 | 0.036 | 0.132 | 2.56 | 5.90 |
| Bebetsugawa | T4240 | 103.60 | 200.80 | 0.23 | 0.32 | 1.40 | 5.69 | 1617 | 0.033 | 0.114 | 2.30 | 6.40 |
| Upper Teshio | U4130 | 46.90 | 74.30 | 0.42 | 0.47 | 1.60 | 5.80 | 870 | 0.042 | 0.101 | 1.89 | 5.70 |
| Teshio | U4010 | 65.70 | 133.60 | 0.39 | 0.45 | 1.70 | 7.84 | 1122 | 0.039 | 0.097 | 1.89 | 6.20 |
| Ushisubetsugawa | T4300 | 75.00 | 190.30 | 0.43 | 0.49 | 1.71 | 10.23 | 699 | 0.022 | 0.051 | 2.15 | 5.80 |

Note: P=perimeter, A=area, Rc=circularity ratio, Re=elongation ratio, S=channel sinuosity, Wm=basin mean width, Hr=basin relief, Rr= relief ratio
MRN=Melton's ruggedness number, Dd=drainage density, WRb=weighted bifurcation ratio.

### 6.4.3. Hydrological characteristics

The initial soil moisture condition analysis has been performed for five catchment areas i.e. Shirai catchment (S1840), Bebetsugawa catchment (T4240), Beiegawa catchment (T4210), Ushisubetsugawa catchment (T4300), and Upper Ishikari catchment (T4010), by making the scatter plot between total rainfall and total loss rainfall for every flood events which the results are shown in Figure 6.3.

The black dots in the scatter plot represent the flood events during the month in the year that the biggest flash flood events were occurred. The white dots represent the biggest flash flood event in every year during period 1998 – 2009. The size of circle shows the relative FI.

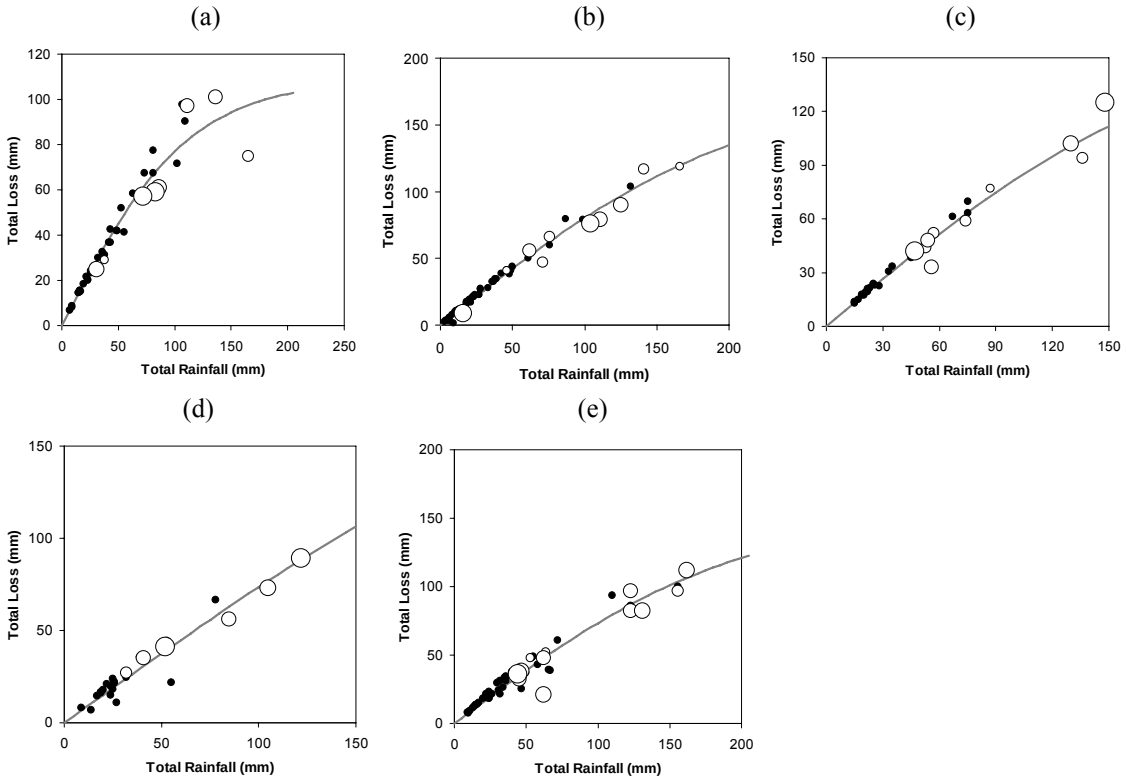


**Figure 6.3.** *Scatter plot between Total Rainfall and Total Loss Rainfall for all rainfall events at the months that the biggest flash flood event are taken place during 1998 – 2009 (black dots) for (a) Shirai catchment; (b) Bebetsugawa catchment; (c) Beiegawa catchment;(d) Ushisubetsugawa catchment; and (e)Upper Ishikari catchment. The white dots are flash flood events. The size of circle shows the relative FI.*

The regression line using tangent hyperbolic model is generated as shown by grey line in the scatter plot. Here, some flash flood events are considered occurred in relatively dry soil moisture initial condition if their plots are located at the upper side of regression line, otherwise they consider occurred in relatively wet soil moisture condition if located at lower side of regression line. The figure confirms that most of the biggest flash floods are occurred in the relatively wet soil moisture initial condition. It is suggested that the flash flood is mostly generated due to saturation excess of rainfall. However, the severity of flash flood does not directly correspond to the total rainfall and total loss rainfall.

Next the variable contributing area i.e. land use, surface permeability and slope, during the flash flood events related to their FI are evaluated. In this analysis the flash flood events that occurred in those five catchments is plotted together into a scatter plot. The flash flood is categorized based on the initial soil moisture condition (i.e. wet and dry initial condition) and basin shape (circular and non-circular). Figure 6.4, 6.5 and 6.6 shows the scatter plot between FI and variable contributing area related to land use, surface permeability and slope conditions by considering initial soil moisture and basin shape.

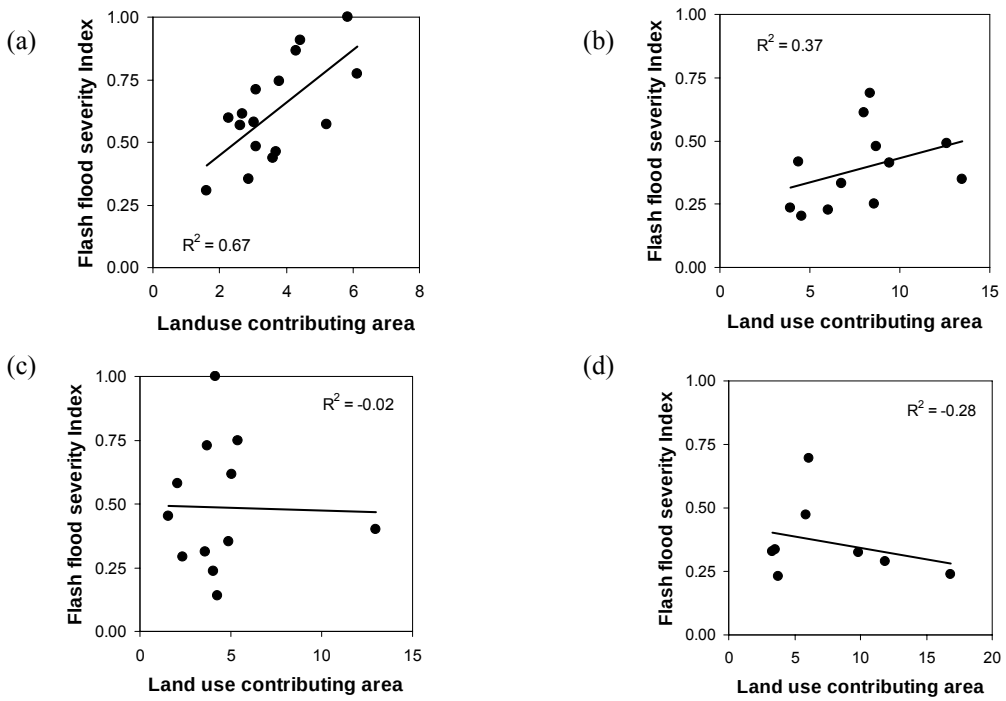


**Figure 6.4.** *Relationships between FI and land use contributing area in the situation of relatively wet soil moisture condition (a and b) and relatively dry soil moisture condition (c –d) which are occurred in relatively circular (a and c) and non-circular (b and d) catchment shape.*

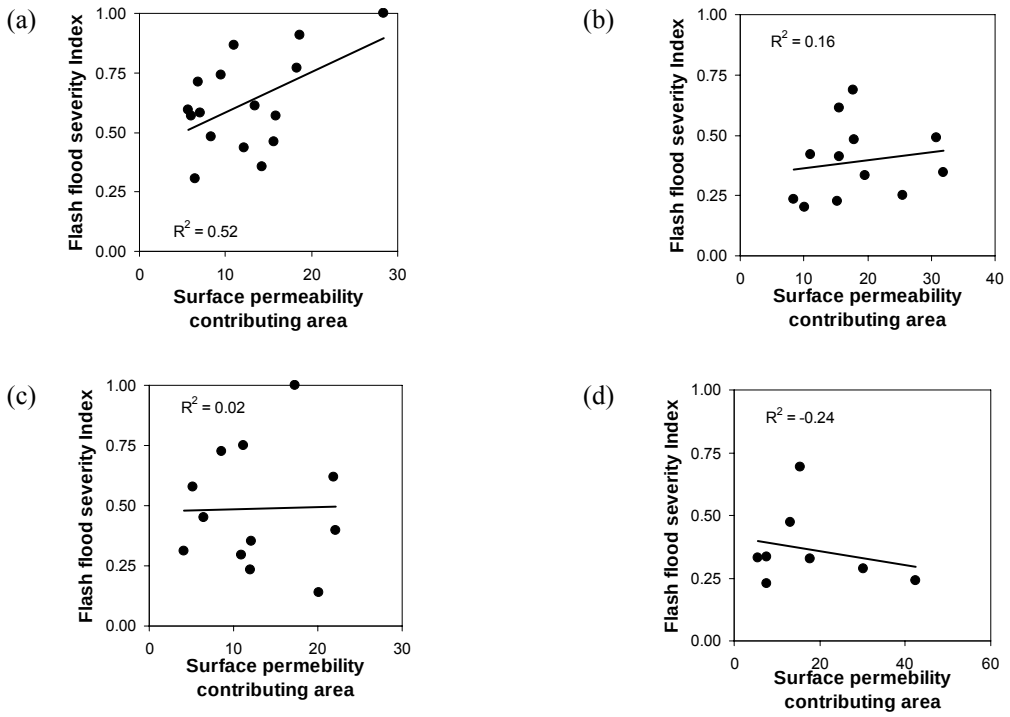


**Figure 6.5.** *Same as figure 6.2 but for rock permeability contributing area*

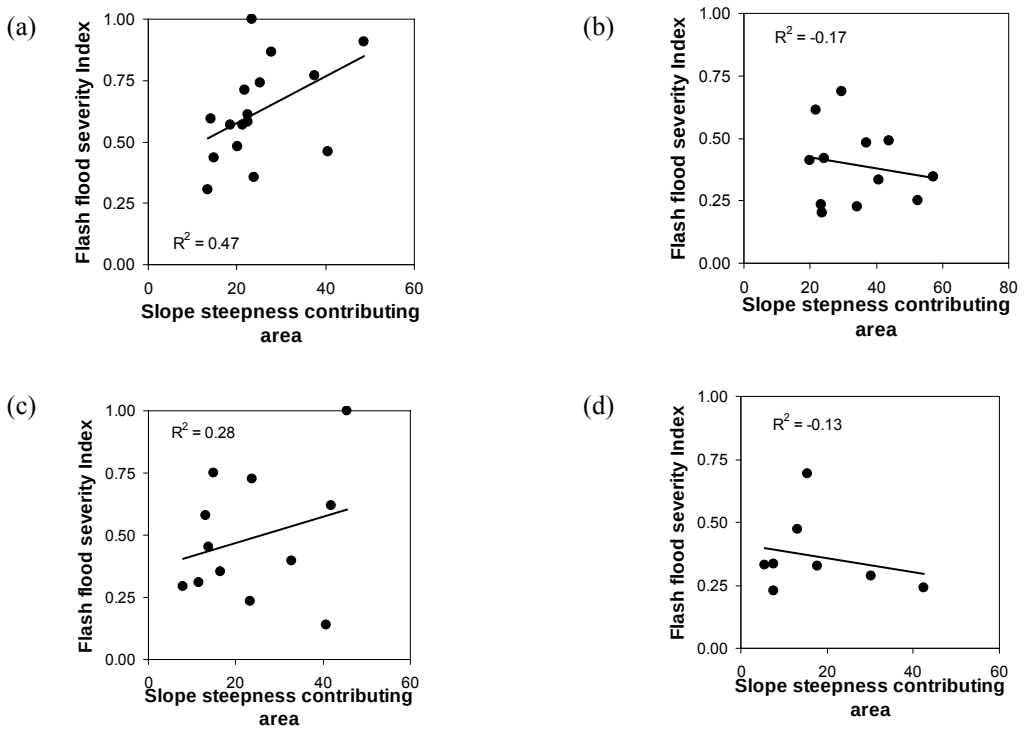


**Figure 6.6.** *Same as figure 6.2 but for slope contributing area.*

Those figures demonstrate that especially for initially wet soil moisture condition the most of the catchments show reasonably strong relationship between FI and variable contributing

area. It is readily explained due to land surface condition is more sensitive to rainfall and directly response to generate runoff. In case of initially dry moisture condition, there is an infiltration process needed, therefore the catchment is less sensitive to rainfall. In this situation the uncertainty of rainfall generation is higher. The results suggest that the accurate identification of initial soil moisture condition is important increase the predictability of flash flood event.

By narrowing the evaluation of variable contributing area vs. FI in the initially wet soil moisture condition, the results indicated that stronger relationship is shown for the circular basin than the non-circular basin shape. One of the possible reasons is that in the circular basin, the distance for all part of the catchments to the outlet is almost the same; therefore the time concentration is mainly as the function of the basin surface is condition, without considering delay time to the outlet.

### 6.4.4. Meteorological characteristics

Based on the previously flash flood events that have been identified for each year, their corresponding rainfall events are collected. Instead of using FI average, here the FI values that derived from single event to be related to two rainfall parameters i.e. rainfall intensity and rainfall location index are used. The rainfall intensity is calculated as areal average of the catchment. Similar with hydrological characterization, the meteorological characteristic identification was focused on five catchments.

Figure 6.7a and 6.7b respectively shows the scatter plot between FI vs. rainfall intensity and rainfall location index. The relationship between rainfall intensity and FI in the initially wet soil moisture condition shows a consistent relation since higher intensity corresponds to severe flash flood. It is readily explained that the higher intensity the possibility in exceeding infiltration rate is also higher. In the situation that initially dry soil moisture, some inconsistent relationship between rainfall intensity and FI is shown.

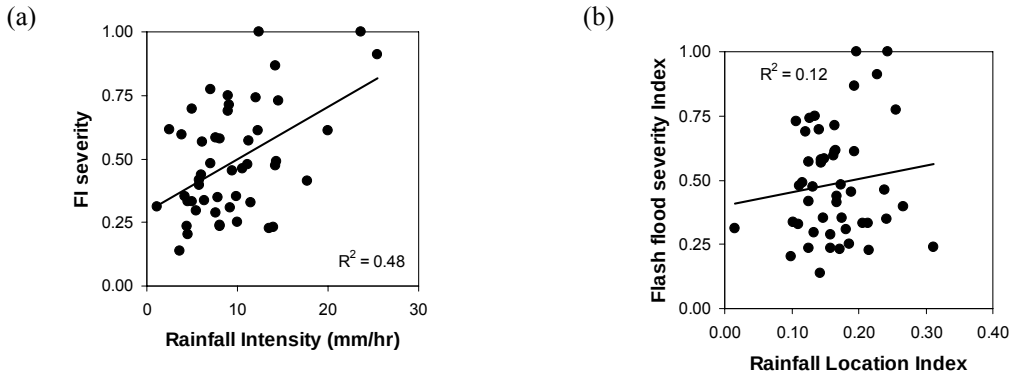


**Figure 6.7.** *Scatter plot of FI vs. (a) rainfall intensity and (b) rainfall location index.*

For the relationship between FI and rainfall location index, the results demonstrate inconsistent for both initially dry and wet soil moisture conditions. One of the possible reasons is that the rain gauge distribution is not dense enough, therefore the interpolated rainfall is failed to capture the local variability of the rainfall.

### 6.4.5. Flash flood severity index development and implementation.

Based on the above identification results of hydrological, morphometrical and meteorological characteristics, the flash flood severity model is developed. Firstly the statistical relationship between FI and morphometrical characteristic is generated. According to the step-wise regression analysis, the most prominent morphometrical factors that influence the $FI_{morphometry}$ in the Ishikari river basin are elongation ratio (Re), relief ration (Rr) and Melton's ruggedness number (MRN) which is described by following model

$$FI_{morphometry} = 0.889Re - 5.026Rr + 2.387MRN \quad (r^2=0.98) \qquad (6.19)$$

Secondly, the statistical relationship between FI and hydrological characteristic (i.e. variable contributing factors) is also analyzed by using step-wise regression analysis. Here, the model is assumed to be valid in the situation of initially wet soil moisture condition. The catchments shape i.e. circularity ratio, is considered during model development, therefore there are two models (based on catchment shape) which is specifically applied on ungauged catchments,

$$FI_{circular} = 0.164LUSE \quad (r^2=0.98) \qquad (6.20)$$

$$FI_{non\text{-}circular} = 0.046LUSE \quad (r^2=0.85) \qquad (6.21)$$

Those models suggest that among the land surface characteristics of catchment, the land use contributing area (LUSE) is the most prominent factor that influences the FI index.

Lastly, the statistical relationship between FI and meteorological factors is defined. Here both of rainfall characteristics are used in the step-wise regression analysis, however only rainfall intensity factor (RAIN) that most influence the FI, which is expressed in the following model

$$FI_{meteorology} = 0.045RAIN \quad (r^2=0.81) \qquad (6.22)$$

The developed flash flood severity index model is implemented in some mountainous catchments in Toyohira basin during 23 August 2010 heavy rainfall event. The hydrological and

morphometrical parameters which are significantly influence the flash flood i.e. land use contributing area (LUSE), elongation ratio (Re), relief ratio (Rr) and Melton's ruggedness number (MRN) are extracted in those 42 sub-catchments and the above model is applied to the data.

Figure 6.8a and 6.8b show the flash flood severity index distribution as a function of meteorological factor (rainfall intensity) and hydrological factor (land use contributing area) respectively. The warm color represents relatively high potential severity of flash flood. For the implementation of both empirical models, MTSAT based rainfall estimation is coupled into the models. Figure 6.8d shows the MTSAT based rainfall from 23 August 2010 at 20:00 UTC which is used to estimate the FI. Comparison of Figure 6.8a with Figure 6.8d indicate that the FI pattern resemble the rainfall intensity distribution. It is because the FI is a linear function rainfall. However the pattern similarity of rainfall intensity is not found by FI as a function of land use contributing factor. It is because the land use modulates the rainfall become runoff. Figure 6.8c show the FI as the function of morphometrical factors. Since rainfall is not considered here, this map show the potential of flash flood severity being occurred in particular catchment, rather than the actual flash flood severity such as demonstrate by Figure 6.8a and 6.8b.

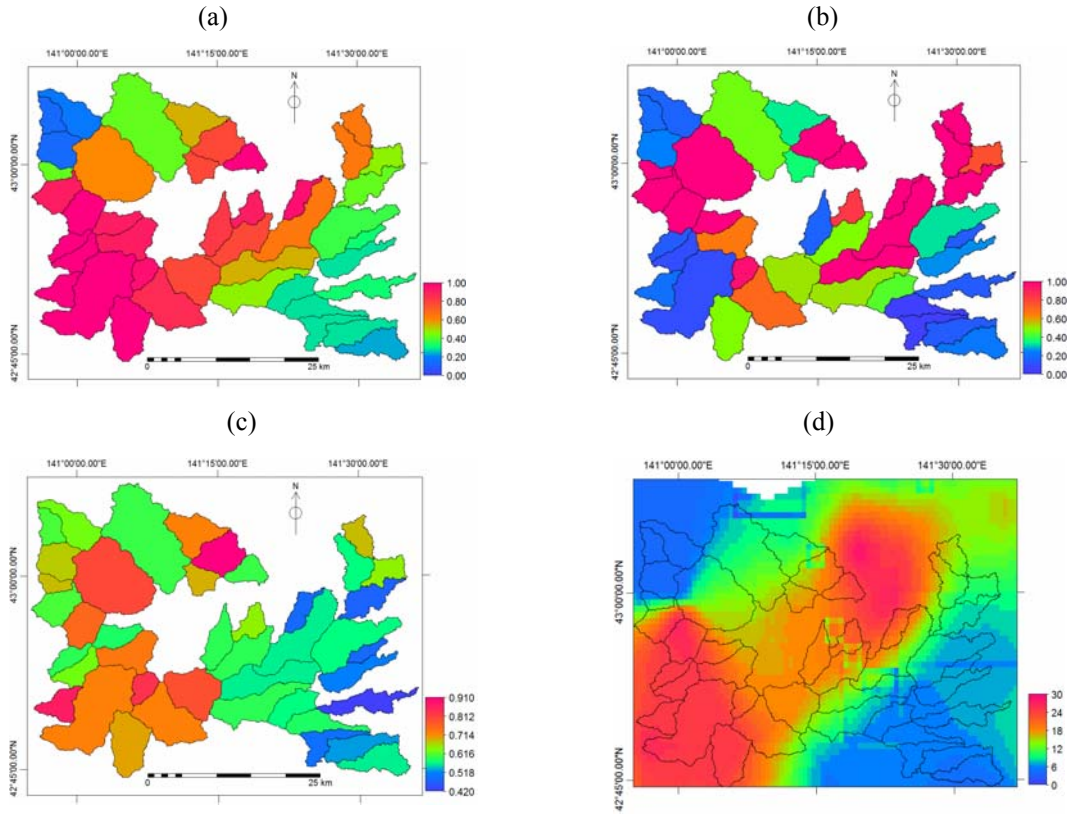


**Figure 6.8.** *Flash flood severity index distribution map as a function of (a) meteorological factor (rainfall); (b) hydrological factor (land use) and (c) morphometrical factors (elongation ratio, relief ratio and Melton's ruggedness number) in sub-catchments of Toyohira basin and its surrounding area. (d) MTSAT based estimated rainfall for 23 August 2010 at 20:00 UTC.*

A catchment area that might be potentially low risk of flash flood severity can be changed into high risk due to severe rainfall occurred in the current catchment. Otherwise a catchmet area that suffers from high intensity rainfall is not always producing severe flood because the rainfall influence is diminished by hydrological condition of catchment.

The limitation of the use of empirical model of flash flood severity index, particularly using meteorological and hydrological factor is that the range of sample events which used to develop the model should sufficient enough to cover any possible extreme event that may occur in the current region. Otherwise the estimated FI become saturated, when the meteorological and hydrological factor value exceeds the range and the result may be overestimated.

## 6.5. SUMMARY AND CONCLUSIONS

The flash flood severity index has been analyzed in 16 gauged catchments in western Hokkaido region according hydrograph analysis. The biggest flash flood event that occurred in those catchments for each year is identified during 1998 – 2010 summer periods. Flash flood severity index is identified for each flash flood events. The regression analysis to find the relationship between flash flood severity and hydrology, morphometry and meteorology of the catchment has been performed.

The regression analysis between FI and morphometrical parameters at 16 catchments indicates that not all morphometrical parameters show logical relationship with flash flood severity index. The FI is mainly closely related to the shape factors (i.e. circularity ratio and elongation ratio) and the topographical factors (i.e. basin mean wide, relief ratio and Melton's ruggedness number). Particularly for hydrological and meteorological characterization, the analysis has been focused on five catchments area. The initial soil moisture condition has been evaluated by using scatter plot of total rainfall vs. total loss rainfall for all flood events during the months that the biggest flash floods took place during 1998 – 2010 summer periods. The result shows that initial soil moisture condition was reasonably influencing the relationship between variable contributing areas with flash flood severity index. Moderately strong relationship between the variable contributing area and flash flood severity index is shown in situation of relatively wet soil moisture initial condition. In the relatively dry soil moisture condition, it was difficult to find pattern between variable contributing area and flash flood severity index. This result suggests that the accurate identification of initial soil moisture condition is important increase the predictability of flash flood event. For the meteorological characterization, two rainfall properties has been evaluated i.e. rainfall intensity and rainfall location index. However

the results show that only rainfall intensity demonstrates strong relationship with flash flood severity index. The implementation of the empirical models at Toyohira basin shows that FI as the function of morphometrical factors can provide flash flood potential information. Moreover, FI as the function of hydrological and meteorological factors demonstrate more dynamic pattern since they correspond to rainfall distribution.

# Chapter 7. PHYSICAL BASED RAINFALL-RUNOFF MODEL FOR FLASH FLOODS ESTIMATION

This chapter is based on: Suseno, Dwi Prabowo Yuga, T. J. Yamada, 2013, **The use of Geostationary Satellite Based Rainfall Estimation Combined With Land Surface Model for Regional Flash Flood Assessment**, to be presented on The 6th conference of The Asia Pacific Association of Hydrology and Water Resources, Seoul, Korea

## Abstract

An understanding of hydrological behavior especially related to extreme event such as flash flood is vital for flood mitigation and management. This study aims to assess the flash floods in a regional scale by implementing the Minimal Advance Treatments of Surface Interaction and Runoff (MATSIRO). MATSIRO is originally designed for global scale hydrological study and using various data forcing both atmospheric and land surface forcing. In this study, they are downscaled into regional scale. In order to make the model more applicable particularly to the region that the availability of meteorological data is lacking, the use of remote sensing to acquire some data input has been focused. Several remote sensing sensors such as Moderate Resolution Imaging Spectroradiometer (MODIS) and Clouds and the Earth's Radiant Energy System (CERES) sensors had been utilized to derive several distributed parameter such as leaf area index (LAI), ground albedo, downward radiation (shortwave and longwave) and land cover. Moreover, digital elevation model (DEM) obtained by Shuttle Radar Topographic Mission (SRTM) was implemented to quantify some topographic and river flow parameters. Specifically for the rainfall forcing, it is generated from the Multifunctional Transport Satellite (MTSAT) based rainfall estimation which is downscaled by using local observed rainfall (Automated Meteorological Data Acquisition System/AMeDAS). The river flow simulations were run over Ishikari river basin in 1-km grid resolution by using three rainfall data forcing i.e. AMeDAS rainfall, MTSAT based estimated rainfall and Ministry of Land, Infrastructure and Transport (MLIT) rainfall. A comparison of estimated peak discharge resulted by those simulations with observed stream flow is performed and evaluated. The river flow simulations demonstrate that the MLIT rainfall based estimated discharge is the best in predicting peak discharge. However, MTSAT downscaled demonstrate more advantage as input forcing in the MATSIRO because the performance is about comparable with the relatively dense rain gauge network such as the MLIT.


Key Words: MATSIRO, rainfall estimation, flash flood assessment, river flow simulation

## 7.1. INTRODUCTION

An understanding of hydrological behavior of a catchment area especially related to extreme event such as flash flood is vital for flood mitigation and management. Some studies related to flash flood study for mitigation has been conducted such as risk estimation (Yousef et al., 2010), early detection (Alfieri et al, 2012) and severity (Bashkar et al, 2000; Kim and Choi, 2011; 2012). Due to the importance of flash flood information such as their risk and early warning, such information should be provided all over the region, particularly those vulnerable to flash flood. The magnitude of peak discharge and its time to peak discharge during flash flood event are considered as the important parameters that should be provided for mitigating their disastrous effect. Those information usually are derived by analyzing the discharge that measured by water level recorder instrument installed at the catchment's outlet. However, this effort mainly hampered due to the shortage of data. It is because not all catchments are equipped with discharge measurement instrument. Missing of data is often to be happened due to the river gauges have damaged by severe flash flood. As an alternative way for obtaining such hydrological data, instead of using direct measurement, the rainfall-runoff model is utilized to get simulated discharge.

The rainfall observation network data is commonly employed as the input data for the rainfall-runoff model. However it has disadvantage due to sparse and uneven distribution in space. The limitation of fund, accessibility of the site and the purpose of network is considered as constraint for developing high density and well configuration of rain gauge network (Haile, 2011). Radar can be used to obtain the spatial distribution of rainfall, however this method is considered too expensive. The high mountainous range that can block the radar signal is also considered as another restriction. The geostationary based rainfall estimation gives an opportunity for providing continuous rainfall information particularly for the ungauged catchments (Kinoti et al, 2010, Suseno and Yamada, 2013a). The geostationary satellite image which is blended with microwave satellite based rainfall measurement is preferable instead of the use of microwave satellite based rainfall measurement solely. It is because the geostationary satellite has advantage for capturing global coverage with continuous acquisition time which is very useful for monitoring purpose. The geostationary based rainfall estimation can be coupled with a rainfall-runoff model for predicting the flood discharge produce by a catchment (Wardah et al., 2008).

Hapuarachchi et al. (2011) conducted a review of advances in flash flood forecasting and notify that the physically based hydrological model particularly the distributed model give more plausible results when compared with the results of conceptual, statistical and neural network model. This study intends to conduct a flash flood assessment based on a physically based

hydrological model called the Minimal Advance Treatments of Surface Interaction and Runoff (MATSIRO). The term 'advance' in this model is related to the physically based that used by model and term 'minimal' means that the water and energy exchange between land and atmosphere represented by model had been treated by simple manner (Takata et al., 2003). MATSIRO uses physical process to draw the hydro-meteorological characteristics of a region which is expressed by the energy balance model and the water balance model. The energy balance model is calculated based on those two models, the surface energy flux and land surface interaction among main hydrological components (i.e. precipitation, evapotranspiration, moisture storage and surface flow) can be comprehensively evaluated. The recent implementation of MATSIRO deals with its application for global (1°×1° grid size) and nation wide hydrological study such as in Japan country with 10 km grid size (Pokhrel, 2011). In this study, the MATSIRO was applied for flash floods assessment, for a regional scale, in approximately 1 km by 1 km grid size.

More attentions have been paid in this study for acquiring some input data into MATSIRO by using remote sensing techniques in order it can be applied to overcome the data shortage problem. Rainfall estimation by using Multi-purpose Transport Satellite (MTSAT) (Suseno and Yamada, 2013) is applied as forcing data into MATSIRO model. Some input parameters that generated by remote sensing data is also utilized, such the use of digital elevation model from Shuttle Radar Topographic Mission Digital Elevation Model (SRTM-DEM) and Moderate Resolution Imaging Spectroradiometer (MODIS) sensors to derived surface topography data, stream network and land cover.

The objectives of this study are (i) to generate some data forcing by using remote sensing and to apply into MATSIRO and (ii) to perform a river flow simulation using MATSIRO and compare estimated discharge obtained from the model with the observed discharge. The estimated discharge is derived by using both observed rainfall and satellite based rainfall estimation.

## 7.2. THE STUDY AREA AND DATASETS

The study area is Ishikari river basin, Hokkaido Island, Japan (see grey area in Figure 7.1). The time period during 2010 was examined for MATSIRO data forcing preparation process. The MODIS sensors had been used to derive several distributed parameters such as leaf area index (LAI), ground albedo and land cover. MODIS has high spectral resolution (36 spectral bands) with various spatial resolutions (250m, 500m and 1km) depend on the channel.

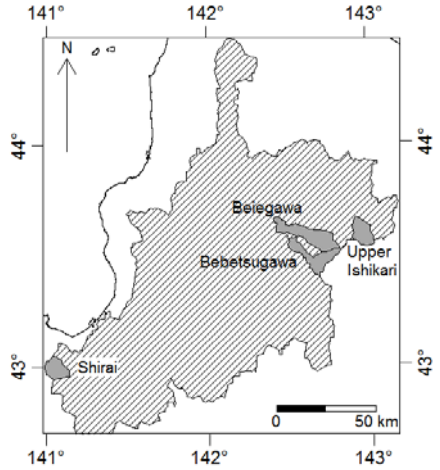


**Figure 7.1.** *Ishikari river basin, Hokkaido bounded as grey area. The yellow and pink color represents the catchment area of Shirai and Bebetsugawa river accordingly.*

The downward radiation (infrared and visible) was derived from Cloud and Earth's Radiant Energy System (CERES) sensors. Both MODIS and CERES are the name of remote sensing sensors that mounted at two polar orbit satellites platform namely Terra and Aqua. The 3 arc second (approximately 90 m) SRTM-DEM was used to derive some topographic parameters in MATSIRO such as surface slope, standard deviation of altitude in grid cells, flow direction and river sequence map. The SRTM finished grade product can be downloaded freely from http://srtm.usgs.gov.

Automated Meteorological Data Acquisition System (AMeDAS) data was mainly used to derive atmospheric data forcing for MATSIRO such as rainfall, wind velocity, atmospheric temperature, atmospheric humidity and atmospheric pressure. Especially for the rainfall, this study is also using rain observation derived by Ministry of Land, Infrastructure and Transport (MLIT) observation network. Particularly for the mountainous region, the MLIT's observation network is considered relatively denser than the AMeDAS observation network. The cloud coverage is acquired from Japan Meteorological Agency (JMA) meso scale model. Particularly for rainfall data, in this study estimated rainfall from Multi-functional Transport Satellite (MTSAT) that statistically downscaling using AMeDAS rainfall measurement are utilized. A statistical downscaling for rainfall data was conducted mainly for June–September of 2010.

Lastly a soil texture map was employed as the base map for several soil physical attributes that used in MATSIRO. This map is derived from Food and Agriculture Organization (FAO) digital soil map of the word, which is delivered in vector format in 1:5,000,000 scales. Table 7.1 shows the summary of data used in the MATSIRO land surface model and the preprocessing method utilized to generate those data.

**Tabel 7.1.** *Atmospheric and land surface parameters source and preprocessing.*

| Parameters | Source | Spatial resolution | Temporal Resolution | Data Preprocessing |
|---|---|---|---|---|
| Atmospheric parameters | | | | |
| Precipitation (Rainfall and Snowfall) | AMeDAS observation | Point based interpolated into 1-km | 1 hour | Spatial interpolation |
| | MLIT observation | Point based interpolated into 1-km | 1 hour | Spatial interpolation |
| | Remote sensing (MTSAT based estimation) | 5 km | | Spatial interpolation and statistical downscaling |
| Wind | AMeDAS observation | Point based interpolated into 1-km | 1 hour | Spatial interpolation |
| Atmospheric Temperature | AMeDAS observation | Point based interpolated into 1-km | 1 hour | Spatial interpolation |
| Atmospheric Pressure | AMeDAS observation | Point based interpolated into 1-km | 1 hour | Spatial interpolation |
| Atmospheric Relative Humidity | AMeDAS observation | Point based interpolated into 1-km | 1 hour | Spatial interpolation |
| Cloud cover | JMA Mesoscale Model | 25 km | 3 hour | Spatial Resampling |
| Shortwave downward radiation | Remote sensing (CERES) | 20 km | ~12 hour | Spatial Resampling |
| Longwave downward radiation | Remote sensing (CERES) | 20 km | ~12 hour | Spatial Resampling |
| Land surface parameters | | | | |
| Land use | Remote Sensing (MODIS) | 1 km | yearly | Georeferencing and spatial resampling |
| Surface slope | Remote Sensing (SRTM-DEM) | 90 m | - | Spatial aggregation and DEM processing |
| Standard deviation of surface topography | Remote Sensing (SRTM-DEM) | 90 m | - | Spatial aggregation and DEM processing |
| Flow direction | Remote Sensing (SRTM-DEM) | 90 m | - | Spatial aggregation and DEM processing |
| Flow accumulation | Remote Sensing (SRTM-DEM) | 90 m | - | Spatial aggregation and DEM processing |
| Surface Albedo | Remote Sensing (MODIS) | 1 km | 16 days | Georeferencing |
| Leaf Area Index | Remote Sensing (MODIS) | 1 km | 8 days | Georeferencing |
| Soil texture | FAO digital soil map of the world | Vector based at 1:5,000,000 scale | - | Georeferencing and spatial resampling |

## 7.3. DESCRIPTION OF THE MATSIRO LAND SURFACE MODEL

MATSIRO simulates the energy balance that solved separately at the ground surface and canopy surface and the energy and water exchange between ground surface and the atmosphere (Takata et al., 2003). In the purpose of simulating the energy balance as well as their exchange with the water, the process is treated in two component in the MATSIRO namely LNDFLX for determining parameters and calculating surface fluxes, and LNDSTP for treating the ground process.

The LNDFLX read some external parameters which is prescribed as horizontal distributions (map) such as land cover type (LC), soil type (SOIL), leaf area index (LAI), ground albedo (GALB), surface mean slope (SLOPE) and standard deviation of altitude in a grid cell (ELEVSTD). The input variables such as precipitation wind velocity (U), atmospheric temperature (T), humidity (Q), pressure (P) and downward radiation (RD) variable are set. Next, the albedo (ALB), the aerodynamic resistance, the surface evaporation resistance and the stomatal resistance are evaluated using radiative transfer in canopy, the turbulent transfer and the photosynthesis. The input variable are utilized for diagnosed the surface fluxes (the sensible and latent heat fluxes, the upward radiation and the heat conduction into snow) and prognosticated the surface energy balance (surface skin and canopy temperature).

Finally, in the LNDSTP, the canopy water budged, the snow amount, the runoff amount and the soil temperature and moisture are calculated from precipitation (rainfall and snowfall) using the fluxes obtained by LNDFLX as the upper boundary condition. The time step of the LNDSTP and LNDFLX integration that used in this study is 1-hour interval. The relationship among atmospheric and land surface parameter as well as the calculation flow used in MATSIRO is summarized in a flow chart as show in Figure 7.2.

More specifically, this study is deal with the runoff component generated by the MATSIRO. Here, the runoff is generated by considering four different mechanisms: (i) ground water runoff (base runoff); (ii) saturation excess runoff (Dunne mechanism); (iii) infiltration excess run off (Horton mechanism) and; (iv) overflow of surface soil layer (Takata et. al., 2003; Pokhrel, 2011). To estimate the first three types, MATSIRO implement a simplified TOPMODEL by Beven and Kirkby (1979). In MATSIRO the topographic parameter is treated in a subgrid as the slope based length ($L_s$) that defined as follow:

$$L_s = 2\sqrt{3}\sigma_z \big/ \tan\beta_s \tag{7.1}$$

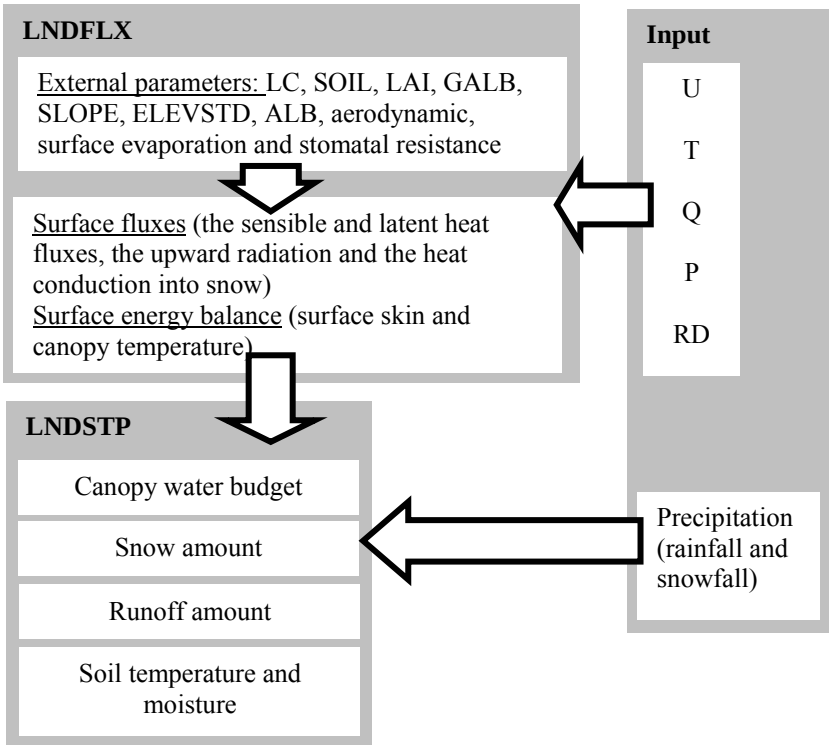


**Figure 7.2.** *The structure and calculation flow in the MATSIRO (reproduced from Takata et. al., 2003).*

where $\beta_s$ is uniform slope angle and $\sigma_z$ is standard deviation of sub grid topography in the grid box. By using that simplified slope based length, the water table depth z(x) at a point distant from valley by a distance x is calculated as (with the assumption uniform recharge rate at the water table)

$$z(x) = \bar{z}_{WT} - \frac{1}{f_{atn}}\left(\ln\frac{x}{L_s} + 1\right) \tag{7.2}$$

where $\bar{z}_{WT}$ is the mean water depth of the grid, $f_{atn}$ is the reduction factor of hydraulic conductivity. The mean water table itself is diagnosed from vertical distribution of soil moisture.

The ground water runoff $RO_b$ (base runoff) is calculated using

$$RO_b = \frac{K_0 \tan\beta_s}{f_{atn} L_s}\exp(1 - f_{atn}\bar{z}_{WT}) \tag{7.3}$$

where $K_0$ is saturation hydraulic conductivity at the surface. Here it assumed that the base runoff is equal to recharge. A quasi equilibrium assumption i.e. groundwater runoff at a point in a slope is equal to accumulated groundwater recharge in the upper area. By this assumption a concept of saturated area fraction ($A_{sat}$) is introduced. In the low topographic condition such as lower part of slope, the water table depth becomes shallower and reaches ground surface, therefore runoff is generated. $A_{sat}$ is expressed as:

$$A_{sat} = 1 - \exp(f_{atn}\bar{z}_{WT} - 1) \tag{7.4}$$

In the saturation excess runoff, $RO_s$ is assigned as the runoff produced by precipitation over the saturated area around the river channel, at it is estimated as (Pokhrel, 2011):

$$RO_s = (\mathrm{Pr}_c^{**} + \mathrm{Pr}_l^{**})A_{sat} \tag{7.5}$$

where $\mathrm{Pr}_c^{**}$ and $\mathrm{Pr}_l^{**}$ are the effective convective precipitation after interception loss and effective stratiform precipitation after interception loss respectively.

Infiltration excess runoff occurred when the rainfall intensity exceeds the infiltration capacity of the soil (Beven and Kirkby, 1979). In the MATSIRO the infiltration capacity is assumed equal to saturated hydraulic conductivity. The infiltration excess run off, ROi, is calculated separately for convective and statiform rainfall by considering their proportion in the grid as follow (Pokhrel, 2011):

$$\begin{aligned} RO_i^c &= \max(\mathrm{Pr}_c^{**}/A_c + \mathrm{Pr}_l^{**} - K_0)(1 - A_{sat}) \\ RO_i^{nc} &= \max(\mathrm{Pr}_l^{**} - K_0)(1 - A_{sat}) \\ RO_i &= A_c RO_i^c + (1 - A_c)RO_i^{nc} \end{aligned} \tag{7.6}$$

where, $RO_i^c$ is infiltration excess runoff in areas with convective precipitation; $RO_i^{nc}$ is infiltration excess runoff in areas with stratiform precipitation; $RO_i$ is total infiltration excess runoff; $A_c$ is fraction f grid area over which precipitation input is convective (default is 10 in MATSIRO).

Finally overflow of surface soil layer $RO_o$ is calculated, which is occurs when moisture flux input to the surface soil layer is higher that its conductivity or if soil layer is oversaturated in the numerical solution, which not theoretically possible (Pokhrel, 2011). $RO_o$ is calculated as:

$$RO_o = \max(w - w_{sat} - w_{str})\rho_w \Delta z_g / \Delta t_L \tag{7.7}$$

where w is moisture content of the surface soil layer, $w_{sat}$ is soil moisture capacity (porosity) of the surface soil layer; $w_{str}$ is surface storage capacity, $\rho_w$ is density of the water, $\Delta z_g$ is thickness of the surface soil layer and $\Delta t_L$ is calculation time step.

The produced runoff then routes through river network by using Total Runoff Integration Pathways (TRIP) (Oki et al., 1998). By this process a river flow accumulation is generated for every time steps, therefore the estimated river flow (discharge) can be observed in any position in the region, particularly in the outlet of the catchment.

## 7.4. METHOD

### 7.4.1. DEM processing for the topographic and river network parameters extraction.

As previously explained that MATSIRO uses some topographical parameter such as surface slope and standard deviation of altitude in a grid cell. Those parameters are extracted from DEM analysis of SRTM-DEM data. Suppose the surface function of DEM is defined as z=f(x,y), where x and y is the grid location of the elevation z. The first derivative in x and y direction is respectively defined as fx=df/dx and fy=df/dy. The slope angle is calculated by following formula:

$$\beta_s = Arc\tan\left(\sqrt{f_x^{\,2} + f_y^{\,2}}\right) \tag{7.8}$$

The standard deviation of subgrid topography in the grid box is calculated using standard deviation function during aggregation process from 90m×90m into 1km×1km grid size.

Another contribution of SRTM-DEM information into MATSIRO is related to runoff routing processes that made possible by implementing the Total Runoff Integration Pathways (TRIP) (Oki et al, 1998). TRIP is a river channel network that shows the lateral water movement overland following the path of the river channels. TRIP is determined by implementing flow direction calculation procedure DEM. Since the original TRIP was prepared for global scale (1°×1°), therefore to fulfill the study purpose that need more detailed data, the flow direction calculation procedure is performed to the SRTM DEM. This calculation process to derived flow directions and flow accumulation map was facilitated by Integrated Land and Water Information System (ILWIS) (Maathuis and Wang, 2008).

### 7.4.2. Land surface parameters data handling

MODIS data has been utilized for acquiring land surface parameters in MATSIRO. There are several MODIS-based data products that are relevant as the MATSIRO data input such as Leaf Area Index (MCD15A3), surface albedo (MCD43B3) and Land cover type (MCD12Q1). Since those of data are mainly delivered in Hierarchical Data Format (HDF) which is not compatible with the MATSIRO, data format conversion had been conducted. The principle of the conversion was made the data became raw binary format, which is flexible to convert into another data type. The HDF was converted into raw binary format by using HEG tool. The HEG tool is a Java application to convert HDF Earth Observation System (HDF-EOS) to Geographic Information System (GIS) format such as GeoTIFF, native (or raw) binary format, and HDF-EOS grid format. The conversion of raw binary format to MATSIRO data input format had been facilitated by the GTOOL.

MATSIRO uses soil texture as the primary key to store some physical properties of soil such as soil heat capacity, soil heat conductivity, porosity, saturation hydraulic conductivity, saturation hydraulic potential and exponent parameter of moisture retention curve (Takata et al, 2003). Here, the texture soil map had been obtained from Digital Soil Map of The World. This is a vector data set that is prepared based on the FAO-UNESCO soil map of the world at 1: 5,000,000 scales.

### 7.4.3. Atmospheric data forcing preparation and statistical downscaling

Several atmospheric data forcing for MATSIRO such as precipitation, wind velocity, atmospheric temperature, atmospheric humidity, atmospheric pressure, downward radiation (infrared and visible), and cloud coverage had been acquired from various data sources. Precipitation, wind velocity, atmospheric temperature, atmospheric humidity and atmospheric pressure are acquired from AMeDAS observation network. Those of data had been prepared by conducting spatial interpolation of the corresponding value based on the observation point location. The longwave and shortwave downward radiation (infrared and visible) was derived from CERES sensors.

The rainfall data forcing, specifically during June to September 2010 period, was derived by estimating from MTSAT data. A statistical model by utilizing the MTSAT 10.8 μm channel data had been implemented for estimating rainfall. A cloud type classification based on MTSAT split window had also been developed and implemented for the purpose of Cumulonimbus (Cb) cloud detection (Suseno and Yamada, 2012b). The atmospheric environmental conditions i.e.

atmospheric vertical instability and the availability of precipitable water vapor that sustain the Cb cloud generation had been taken into account during rainfall estimation process. Particularly for the convective rain, the statistical model had been combined with precipitable water and atmospheric vertical instability. Since the estimated rainfall output was preserving the native resolution of MTSAT image (approximately 5 km grid), a statistical downscaling method was conducted to convert the data into 1 km grid size. Here the estimated rainfall by MTSAT satellite is downscaled with the observed rainfall (MTSAT downscaled hereinafter).

The downscaling process aims to combine the advantage of those two rainfall data capture systems. Rain gauge observation is the only source of rainfall data that is obtained through direct measurement, however it has limitation due to lack of distribution particularly for remote area. Satellite observation is indirect measurement in nature, but it has very good spatial coverage. By merging the benefit of those systems, the combined result is expected to be improved in accuracy, coverage and resolution (Vila et al, 2009). The discrepancy between satellite based rainfall estimation and direct observation by rain gauge should be reduced during downscaling process through bias correction. The bias correction is based on: (i) additive; and (ii) multiplicative method which is applied for each station in hourly basis. The additive bias correction ($rr^{+}$) and multiplicative bias correction ($rr^{*}$) are respectively defined in equation 7.9 and 7.10 as following (Vila et al, 2009):

$$rr^{+} = rr_{sat} + \overline{(rr_{obs}^{i} - rr_{sat}^{i})} \tag{7.9}$$

$$rr^{*} = rr_{sat} \times \overline{\left( \frac{rr_{obs}^{i}}{rr_{sat}^{i}} \right)} \tag{7.10}$$

The first term in both equations is satellite based rainfall estimation. The second term in equation 7.9 and 7.10 represent respectively the mean bias (represented by the bar) both additive bias and multiplicative bias between the observed and estimated rainfall for each station (denoted by superscript i). The procedure of performing statistical downscaling is as following. The observed rainfall is interpolated using inverse distance weight method in 1-km grid size, with the limiting distance about 10 km. The satellite based rainfall is disaggregated from 5-km into 1-km grid resolution. Next, the difference between additive or multiplicative was calculated. The mean of both additive bias and multiplicative bias for each station was performed by applying 3×3 summation filter, divided by number of grid containing bias value. The downscaled bias corrected rainfall was calculated using equation 3 and 4 for the additive and multiplicative accordingly. One particular bias correction method was selected for each point grid based on the minimum difference between that bias corrected rainfall and observed rainfall. For the grid point outside the limiting distance of interpolation, the original estimated rainfall was assigned.

**Table 7.2.** *Summary of river flow simulation using MATSIRO*

| Simulation name | Time duration | Rainfall data forcing |
|---|---|---|
| Simulation I | 1 Jan – 31 Dec 2010 | AMeDAS rainfall observation |
| Simulation II | 1 Jun – 30 Sep 2010 | MTSAT downscalled |
| Simulation III | 1 Jun – 30 Sep 2010 | MLIT rainfall observation |

### 7.4.4. River flow simulation schemes

Three simulations are performed to estimate the river flow by using MATSIRO which is summarized in Table 7.2. First simulation is conducted by using rainfall data forcing from AMeDAS observation during period of 1 Jan – 31 Dec 2010. By this simulation the land surface hydrological conditions is calculated and updated. The first simulation generated so called 'restart file', which is describe the initial condition of the land surface hydrological conditions for each time steps. Next, by using current restart file the second simulation is conducted. This simulation is making use the advantage of restart file that the simulation is not necessarily started from 1 Jan 2010, therefore the second simulation is started from 1 June to 30 Sep 2010 by MTSAT downscaled as the rainfall forcing. The third simulation is similar with the second but the rainfall input is using MLIT rainfall observation. The estimated river flow derived from those simulations then compared with observed discharge for August 2010. The estimated river flow is extracted from river flow distribution at the outlet of a catchment.

## 7.5. RESULTS AND DISCUSSIONS

### 7.5.1. The MATSIRO data forcing acquisition and preparation using remote sensing and GIS

Figure 7.3 shows some examples of land surface parameter used by MATSIRO that derived from remote sensing and GIS analysis. Figure 7.3a depicts the river sequence map that acquired from DEM analysis. This map is used for accumulating the runoff through river network using TRIP module. Figure 7.3b and 7.3c shows LAI map and land cover map which are acquired from MODIS sensors. Both maps are utilized to represent the canopy surface in MATSIRO. Some vegetation properties such as vegetation height and plant physiological parameters are linked to the land cover map through look up table. Considering that vegetation cover is dynamic, the use of remote sensing information is very useful since it can be easily updated to the recent vegetation condition. The look up table method is also use to link some physical soil properties such as soil porosity, hydraulic conductivity, soil heat capacity and conductivity etc into the soil map shown in Figure 7.3d.

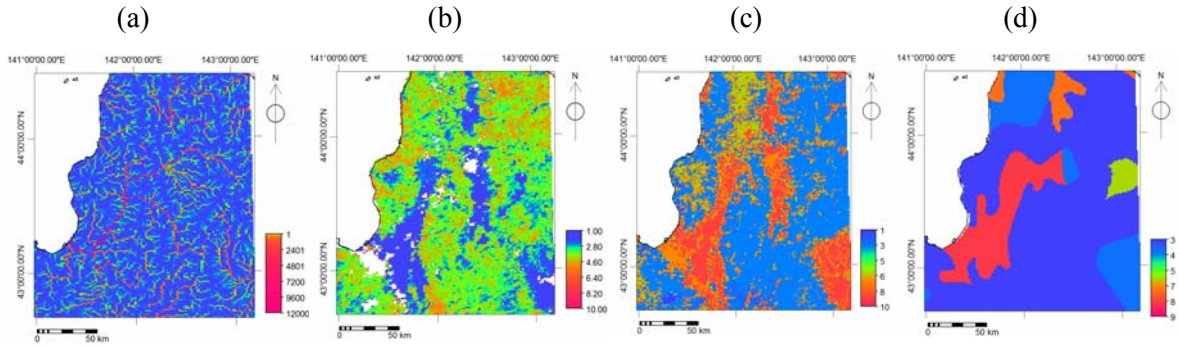


**Figure 7.3.** *Some examples of land surface parameter map of Ishikari river basin (a) river sequence; (b) LAI; (c) land use and (d) soil texture.*

Some snapshoot of atmospheric parameter that derived from both direct observation (AMeDAS) and remote sensing is presented in Figure 7.4. The first four maps are the atmospheric parameters that derived though spatial interpolation from point data value observed by AMeDAS network. Figure 7.4e and 7.4f portray the longwave and shortwave downward radiation respectively acquired from CERES sensors. Since the original resolution of CERES is 20 km, a spatial resampling is performed to disaggregate the data into 1 km grid size. Figure 7.4g shows the percentage of cloud coverage derived from JMA meso scale model.

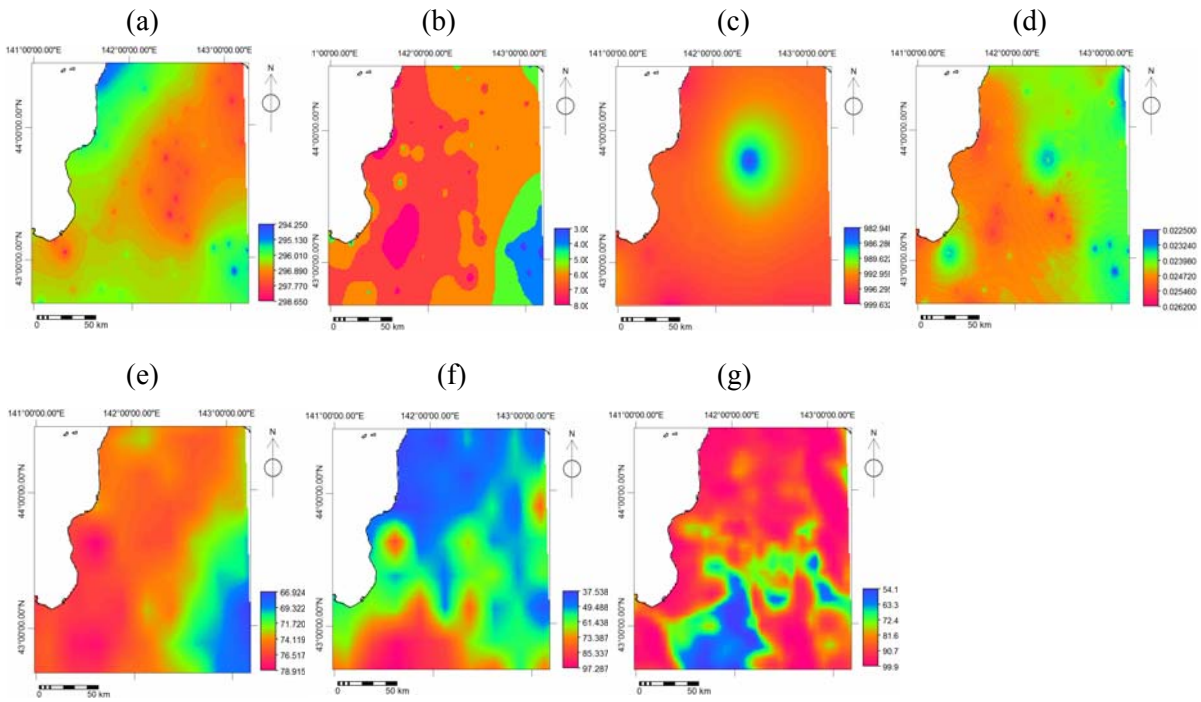


**Figure 7.4.** *Some examples of screen shoot of atmospheric parameter maps of Ishikari river basin from 1 August 2010 at 00UTC: (a) air temperature; (b) surface wind speed; (c) atmospheric pressure; (d) atmospheric humidity; (e) longwave downward radiation; (f) shortwave downward radiation and (f) cloud coverage.*

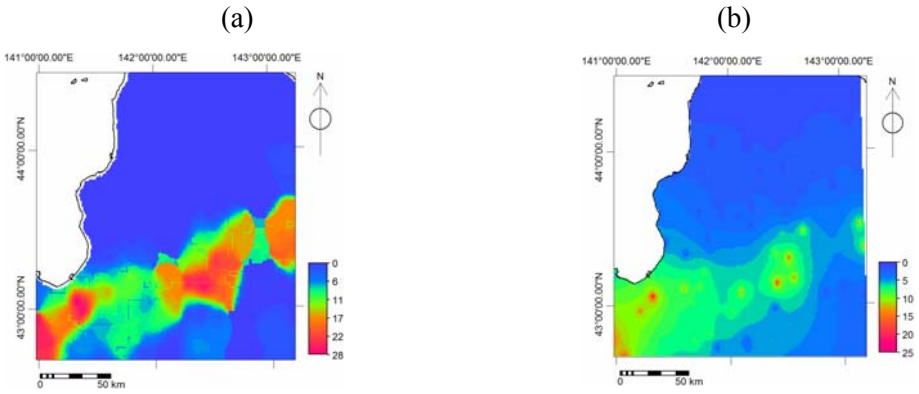


**Figure 7.5.** *Example of rainfall forcing for MATSIRO from 23 August 2010 at 20UTC (a) MTSAT downscaled rainfall estimation; (b) interpolated AMeDAS rainfall observation.*

A statistical downscaling is applied for MTSAT rainfall estimation by merging it with AMeDAS observed rainfall. Figure 7.5a and 7.5b show a comparison instantaneous rainfall between MTSAT downscaled and interpolated observed rainfall during the heavy rainfall event on 23 and 24 August 2010 over Ishikari river basin. Those figures demonstrate that the observed rainfall tends to show the storm as an isolated shower due to the limitation of spatial distribution of rain gauge. This is overcome by the MTSAT rainfall estimation which can show more continuous distribution of rainfall. Both estimated and observed rainfall is extracted by using two catchments area in Ishikari basin i.e. Shirai river and Bebetsugawa river. The location of both catchments is depicted in Figure 7.1.

The area average of rainfall from MTSAT downscaled and observed rainfall from both AMeDAS and MLIT is calculated for Shirai and Bebetsugawa catchment area. Graphical comparison is conducted by plotting them in a scatter plot as shown in Figure 7.6. By considering that figure in detail, Figure 7.6a, 7.6b and 7.6c successively shows the scatter plot of MTSAT downscaled vs. AMeDAS rainfall, MTSAT downscaled vs. MLIT rainfall, and AMeDAS rainfall vs. MLIT rainfall for Shirai catchment. The similar scatter plots are created for Bebetsugawa catchment such as shown in Figure 7.6d, 7.6e and 7.6f. Those figures indicate that the best relationship is shown by MTSAT downscaled vs. MLIT rainfall compared to others. If it is assumed that MLIT rainfall is showing more accurate rainfall distribution due to the denser network than the others, those scatter plots suggest that the use of MTSAT downscaled is showing reasonably better in representing rainfall than if only using AMeDAS rainfall. It suggest that it is more recommended to use of MTSAT estimated rainfall downscaled by AMeDAS especially in the mountainous ungauge region instead of using only AMeDAS observation.

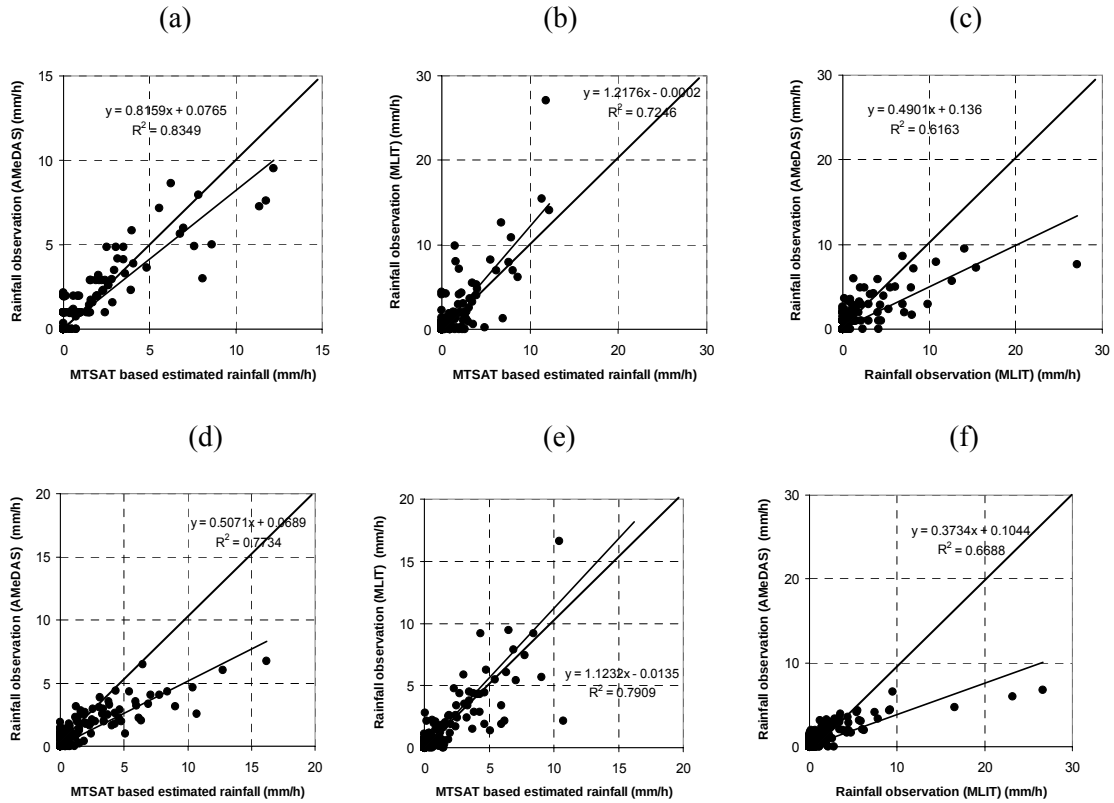


***Figure 7.6.*** *Scatter plot of catchment average hourly rainfall; (a and d) MTSAT based rainfall estimation vs. observed rainfall by AMeDAS, (b and e) MTSAT based rainfall estimation vs. observed rainfall by MLIT, and (c and f) observed rainfall by AMeDAS vs. observed rainfall by MLIT from August 2010 for (a - c) Shirai river catchment and (d - f) Bebetsugawa river catchment.*

### 7.5.2. Comparison of river flow simulation results vs. observed river flow

The comparison of hourly estimated river discharge as the result of river flow simulations using MATSIRO with the observed discharge is presented in two ways i.e. graphical comparison and statistical performance by measuring correlation, bias and root mean square (RMS).

The first graphical comparison is performed by making scatterplot of simulated discharge vs. observed discharge is shown in Figure 7.7. Figure 7.7a, 7.7b and 7.7c show respectively the scatter plot of Simulation I discharge vs. observed discharge, Simulation II vs. observed discharge, and Simulation III vs. observed discharge for Shirai River during August 2010. Figure 7.7d, 7.7e, 7.7f , Figure 7.7g, 7.7h, 7.7i and Figure 7.7j, 7.7k, 7.7l demonstrate the similar figure but for Bebetsugawa River, Upper Ishikari River and Beiegawa River respectively. Those results shows that the correlation of estimate discharge using MTSAT downscaled vs. observed discharge and MLIT rainfall based discharge vs. observed discharge have almost similar strength, which are stronger than AMeDAS rainfall based discharge vs. observed discharge.

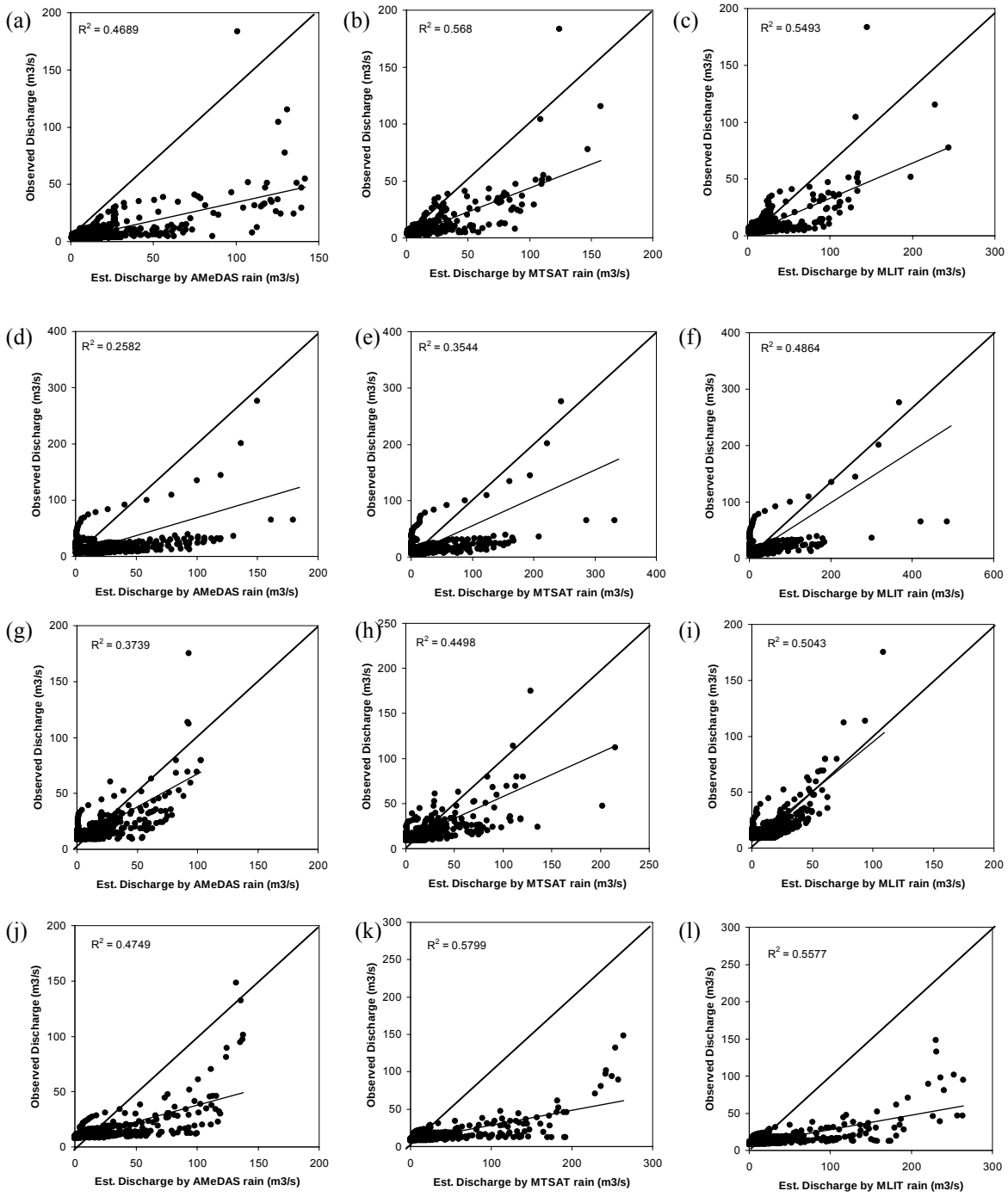


**Figure 7.7.** *Scatter plot of hourly river discharge: (a) estimated discharge by MTSAT rain vs. observed discharge; (b) estimated discharge by AMeDAS rain vs. observed discharge for Shirai River; (c) estimated discharge by MLIT rain vs. observed discharge for Shirai River. Panels (d, e and f), panels (g,h,i) and panel (j,k,l)are respectively the same for Bebetsugawa River, Upper Ishikari River and Beiegawa river.*

This result suggest that the use of MTSAT downscaled as rainfall forcing in MATSIRO is more recommended than that the use of AMeDAS rainfall data forcing.

The second graphical comparisons between simulated discharge vs. observed discharge are shown as line graph in Figure 7.8a to 7.8d which represent the comparison result for Shirai river, Upper Ishikari River, Beiegawa River respectively and Bebetsugawa River respectively. From those graphical comparison it clearly shows that the simulated discharge are mostly overestimated. However, to show more clearly about the river flow simulation during flash flood event, Figure 7.9a to 7.9d shows the comparison peak discharge hydrograph during heavy rainfall event from 23 and 24 August 2010 for Shirai River, Upper Ishikari River, Beiegawa River respectively and Bebetsugawa River respectively. These flood events are considered as flash flood due to short time to peak discharge and relatively high peak discharge. The river flow simulations results demonstrate that estimated discharge using MLIT rainfall is the best for predicting peak discharge compared with the others, especially in Shirai River and Bebetsugawa river. This is readily explained due to MLIT has relatively dense rainfall network compared with AMeDAS, therefore they can represent rainfall distribution better than others. The second best is shown by estimated discharge using MTSAT downscaled and the last is by estimated discharge using AMeDAS rainfall. This result actually is consistent with the previous result, therefore for providing flash flood information in ungauged catchment the use of MTSAT downscaled as rainfall forcing is better than only the use of AMeDAS rainfall. When it is assumed that the sparse distribution of rainfall network is common situation in many places, the MTSAT downscaled demonstrate more advantage as input forcing in a physically based model than if only using the interpolated sparse rainfall observation. It is because MTSAT is basically good in representing rainfall distribution, but less accurate in predicting its amount. This limitation then improved by conducting bias adjustment using observed rainfall even though they are acquired using sparse station distribution.

The above mentioned graphical comparison then confirmed by statistical performance calculation result such as shown by Table 7.3. From the bold-faced numbers that show the best statistic suggests that the simulated discharge using MTSAT downscaled is reasonably comparable with the MLIT rainfall based simulated discharge and they are much better than the use of only AMeDAS rainfall as input forcing. This statistical performance results confirm that the use of MTSAT downscaled as rainfall forcing in MATSIRO is more recommended than that the use of AMeDAS rainfall data forcing.

(a)

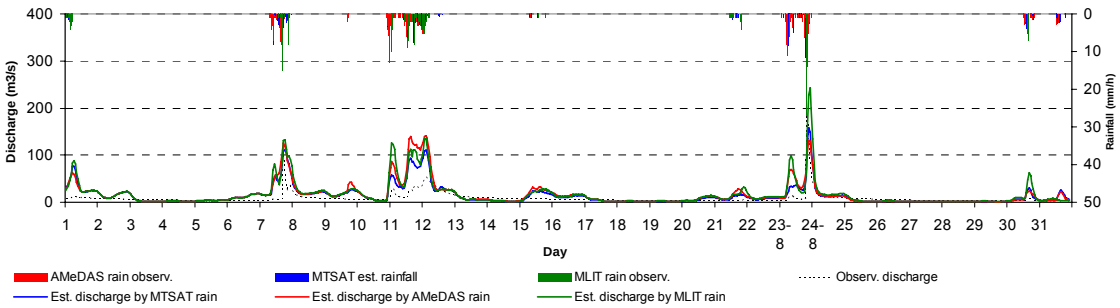


(b)

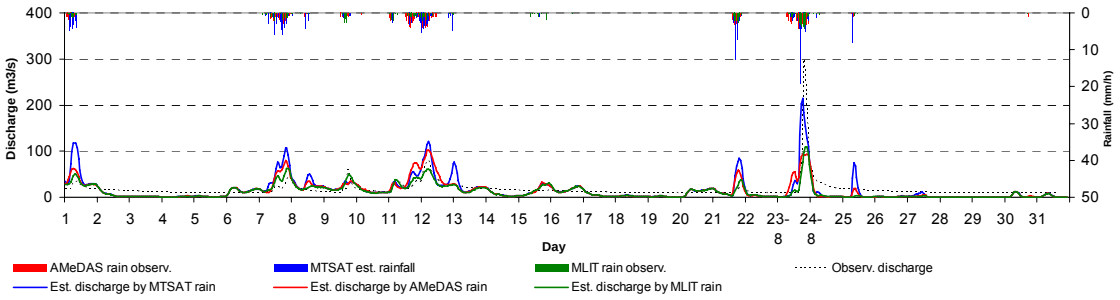


(c)

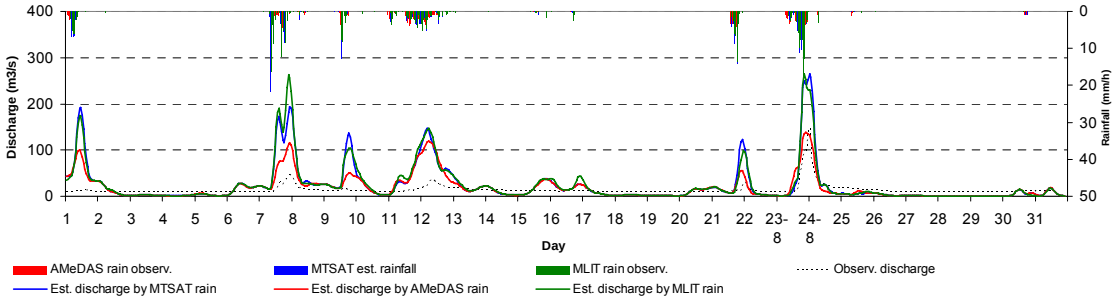


(d)

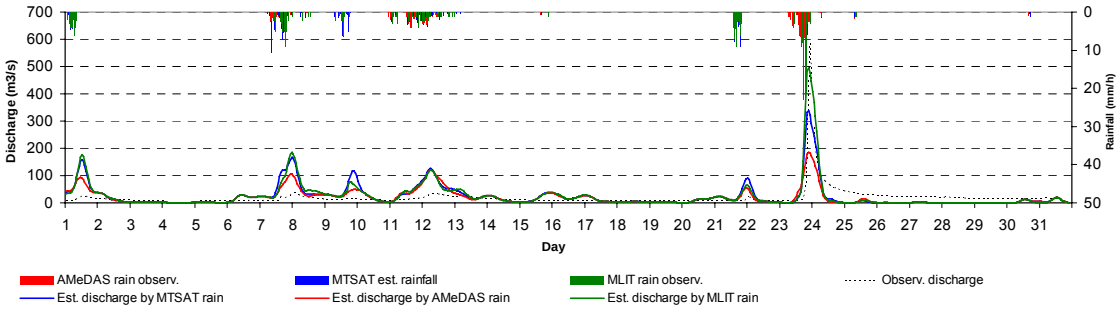


**Figure 7.8.** *Graphical comparison between river flow simulation results vs. observed discharge for (a) Shirai river,(b) Upper Ishikari River, (c) Beiegawa river and (d) Bebetsugawa River.*

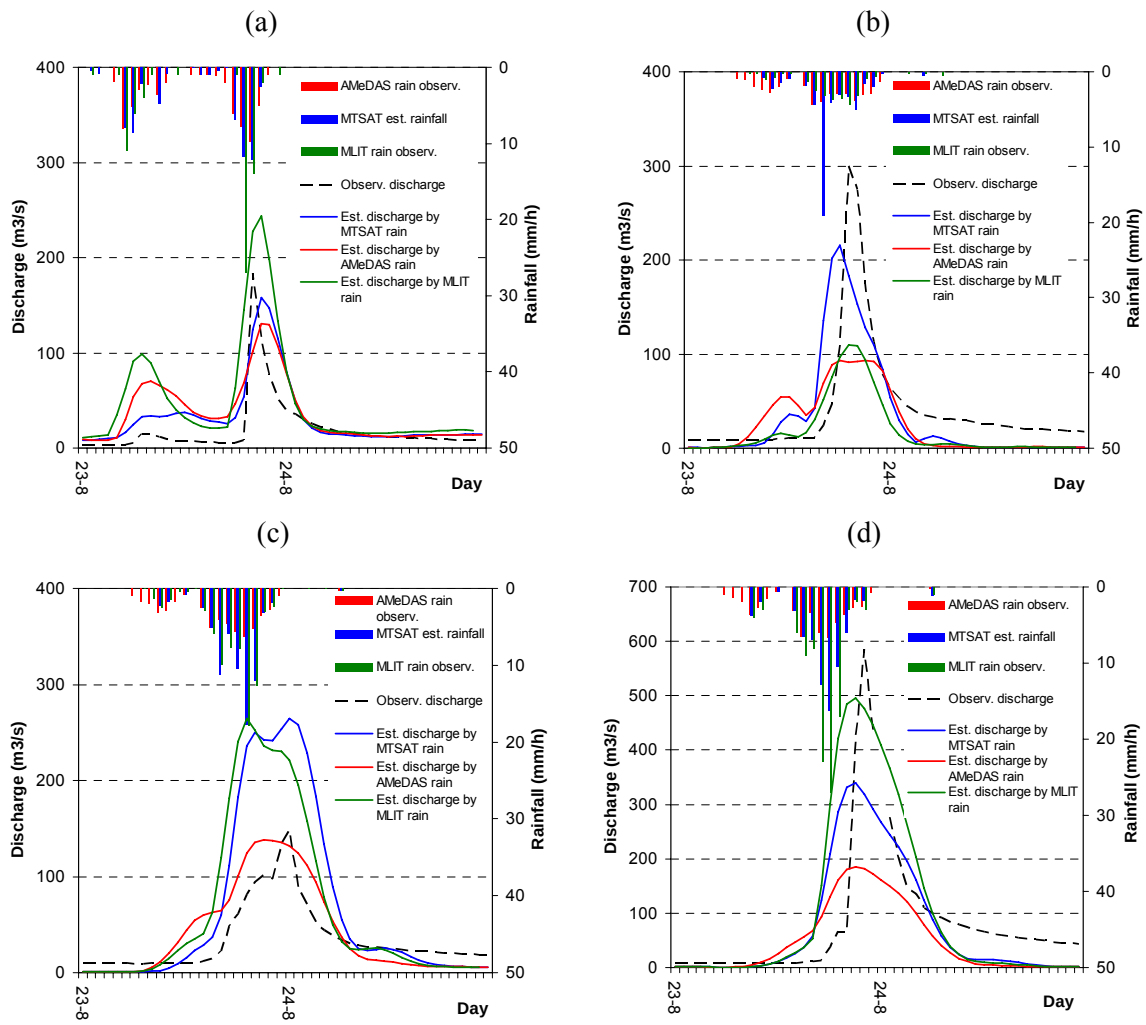


**Figure 7.9.** *Peak discharge during heavy rainfall event from 23 and 24 August 2010 at the catchment's outlet of (a) Shirai river, (b)Upper Ishikari river, (c) Beiegawa river and (d) Bebetsugawa river.*

**Tabel 7.3.** *Comparison of the performance of simulated river discharge vs. observed discharge.*

| Catchment's Name | Est. Disc. From AMeDAS (Simulation I) | | | Est. Disc. From MTSAT based rainfall (downscaled) (Simulation II) | | | Est. Disc. From MLIT (Simulation III) | | |
|---|---|---|---|---|---|---|---|---|---|
| | Cor | Bias ($m^3/s$) | RMS ($m^3/s$) | Cor | Bias ($m^3/s$) | RMS ($m^3/s$) | Cor | Bias ($m^3/s$) | RMS ($m^3/s$) |
| Shirai | 0.68 | 8.7 | 20.8 | **0.75** | **6.5** | **15.5** | 0.74 | 9.8 | 22.8 |
| Upper Ishikari | 0.61 | -2.7 | 16.9 | 0.67 | **-0.7** | 19 | **0.71** | -4.9 | **14.1** |
| Beiegawa | 0.69 | **5.3** | **20.9** | **0.76** | 11.1 | 36.7 | 0.75 | 11.7 | 37.9 |
| Bebetsugawa | 0.51 | **2.1** | **32.1** | 0.60 | 7.1 | 36.9 | **0.70** | 8.4 | 41.3 |

## 7.6. SUMMARY AND CONCLUSIONS

A river flow simulation has been conducted by using MATSIRO land surface model in Ishikari River basin. Input data forcing used is a combination between direct observation from AMeDAS network and remote sensing derived data. Some meteorological parameter such as rainfall, wind speed, air temperature, atmospheric pressure and atmospheric humidity was spatially interpolated based on their point value from corresponding observation station location. The other parameters such as longwave and shortwave downward radiation were derived from CERES sensor and cloud coverage has been acquired from JMA mesoscale model. Satellite remote sensing data such as MODIS and SRTM-DEM were utilized to extract several land surface parameters (e.g LAI, land cover, surface albedo), topographical parameters (e.g. surface slope, standard deviation of altitude in grid cells) and river network parameter (e.g. river sequence and flow direction). Soil texture map was derived from digital soil map of the word published by FAO. A statistical downscaling procedure has been applied to MTSAT satellite based rainfall estimation by merging them with interpolated observed rainfall.

Three simulations are performed to estimate the river flow by using MATSIRO. First simulation is conducted by using rainfall data forcing from AMeDAS observation during period of 1 Jan – 31 Dec 2010. The second simulation is started from 1 June to 30 Sep 2010 by using rainfall forcing from downscaled MTSAT rainfall estimation. The third simulation is started from 1 June to 30 Sep 2010 by using rainfall forcing from MLIT observation. The estimated river flow derived from observed rainfall and estimated rainfall then compared with observe discharge for August 2010. The river flow simulations results demonstrate that estimated discharge using MLIT rainfall is the best for predicting peak discharge compared with the others. However, MTSAT downscaled demonstrate more advantage as input forcing in a physically based model because the accuracy is about comparable with the relatively dense rain gauge network such as the MLIT. Moreover, the sparse rain gauges are commonly found in many places rather that the dense raingauge network and this situation has been proved that can be overcome by merge them with the MTSAT rainfall estimation.

# Chapter 8. SUMMARY, CONCLUSIONS AND RECOMMENDATIONS

## 8.1. SUMMARY AND CONCLUSIONS

This chapter introduces the main results and conclusions which are drawn in relation to the key objectives of this study. They are summarized as following:

**Key objective 1**: *To develop and evaluate the geostationary satellite based rainfall estimation by considering not only cloud top temperature but also cloud type (i.e. Cb cloud type) and atmospheric environmental conditions sustaining the convective cloud development (i.e. precipitable water vapor and atmospheric vertical instability).*

**The basic approach of rainfall estimation using geostationary satellite.**

In this chapter, the main approach of geostationary satellite based rainfall estimation is by developing statistical relationship between cloud top temperature depicted by MTSAT IR1 datasets ($T_{IR1}$) and rain rate observed by TRMM 2A12 datasets (RR). The rainfall is estimated as a function of cloud top temperature depicted by MTSAT 10.8μm channel. Validation is performed by compare it performance both temporally and spatially to TRMM Multi Precipitation Analysis (TMPA).

In the temporal validation, TMPA shows relatively better performance than $T_{IR1}$ and RR based rainfall estimation. This condition is likely related to the probability of good collocation images that may be occurred during rainfall estimation process. TMPA has higher probability to have good collocation because it uses several PMW data compared with $T_{IR1}$ and RR based rainfall estimation that only use one PMW data. According to bias score, it shows that $T_{IR1}$ and RR based rainfall estimation have a tendency to be overestimated and TMPA tend to be slightly underestimated. It indicates that potential precipitating cloud is more frequently detected in $T_{IR1}$ and RR based rainfall estimation than TMPA. There are many potential precipitating cloud detected by MTSAT images which are not producing rain. The temporal validation concludes that TMPA has better performance than $T_{IR1}$ and RR based rainfall estimation in terms of temporal validation. The spatial validation is performed by calculating the average of spatial correlation of $T_{IR1}$ and RR based rainfall estimation and TMPA. The result shows that $T_{IR1}$ and RR based rainfall estimation demonstrates better spatial representation of convective rainfall than TMPA.

**Incorporating cloud type information into rainfall estimation.**

For the convective cloud situation, there is an assumption that lower cloud top temperature is associated with heavier rainfall. However this assumption is reasonable for convective cloud type such as Cumulonimbus (Cb) but poor for other cloud type such as Cirrus (Ci) that cold but light or no rain and stratiform clouds that warm but wet (Kuligowski, 2003). In order to fulfill this assumption a cloud type information is necessary to be integrated in the geostationary satellite based rainfall estimation approach. A new 2D-THR cloud-classification algorithm has been developed; it was trained using MAX classification results for Japan and its surrounding area. The cloud-type classification boundary was defined by adjusting the threshold value of the distribution of mean centre of the cloud-type clusters in the $T_{IR1}$ and $\Delta T_{IR1-IR2}$ scatter plot. Images for northern summer (JJAS) 2009 were used for developing the 2D-THR; therefore, this diagram is typically suitable for classifying clouds during the summer. Inter-comparison of the JMA image and 2D-THR for the same period also proves good visual agreement between the two.

The cloud percentages for JMA and 2D-THR during JJAS 2009 over tropical and subtropical regions were spatially correlated. The results showed that the geographical distribution of the frequency of occurrence of each cloud type is moderately represented by 2D-THR. It suggests that 2D-THR can be reasonably applied for tropical and subtropical regions. Integrating the cloud type classification especially by separating Cb cloud type from other cloud types can improve the $T_{IR1}$ and RR relationship as well as rainfall estimation, which is indicated by increasing correlation coefficient and the gradient of regression line. Moreover, underestimating rainfall intensity can be avoided by applying $T_{IR1}$ and RR relationship that uses Cb cloud type only rather than using all cloud types.

**The role of atmospheric environmental condition for rainfall estimation.**

The use of a single statistical model for the estimation of rainfall is limited due to the variety of physical processes associated with rainfall generation, which eventually influence the relationship between cloud top temperature and rainfall rates. In this part of study, PWV and atmospheric vertical instability, which are both related to the development of deep convective cloud, were investigated. The objectives of the study were to assess how a combination of total PWV and atmospheric vertical instability conditions improves TIR-based rainfall estimations using a statistical model by focusing on Cb cloud systems and to validate the estimated rainfall by comparison with observed rainfall during convective storm rainfall events. In order to get right positition of cloud top temperature relative to the location of the real rain, a parallax correction must be performed on the MTSAT images (both $T_{IR1}$ and $T_{IR2}$). The principle of this algorithm is

to relocate the apparent position of the cloud on the Earth based on the cloud height at its correct geographical location, relative to the MTSAT satellite height and position.

Eight modified exponential models were developed according 28 convective systems over the land area of Japan during the period of June–September 2010 and June–August 2011, which were discriminated based on predefined atmospheric environmental situations: i.e., models that considered only PWV and SSI, namely PWV1 (GPS-PWV ≥ 58 mm), PWV2 (GPS-PWV < 58 mm), SSI1 (SSI ≤ +2), and SSI2 (SSI > +2), and models that combined GPS-PWV and SSI, namely CMB1 (GPS-PWV ≥ 58 mm and SSI ≤ +2), CMB2 (GPS-PWV < 58 mm and SSI ≤ +2), CMB3 (GPS-PWV ≥ 58 mm and SSI > +2), and CMB4 (GPS-PWV < 58 mm and SSI > +2). One model, namely ORG, which did not consider GPS-PWV and SSI, was also generated.

By applying parallax correction for the MTSAT images proves that the image without the parallax correction fails to capture relatively high rainfall rates that should correspond with lower cloud top temperatures. It suggest that parallax correction is essential step should be performed before using the geostationary satellite for rainfall estimation. The cross-correlation analysis of estimated rainfall and observed rainfall indicates that there is a 1-hour time lag between estimated and observed rainfall, which implies that the rainfall detected by satellite could be observed as real rainfall by a rain gauge after 1 hour.

Compared with the observed rainfall, MTSAT rainfall estimations did not represent local strong rainfall events very well, even though in the wider spatial domain, they provided a reasonable representation of the spatial distribution of rainfall. For rainfall >30 mm $h^{-1}$, MTSAT rainfall estimations fail to represent such high rainfall rates.

By considering the atmospheric environmental information, particularly the combination of SSI and PWV, it could enhance the estimated rainfall when compared with the model without considering any atmospheric environmental conditions. In terms of bias and RMSE, the use of atmospheric environmental conditions for rainfall estimation does not produce a meaningful improvement when compared to the model that does not consider any atmospheric environmental conditions. However, the model that considers the combination of total PWV and atmospheric vertical instability demonstrates a reasonable improvement in terms of correlation. This improvement in performance in terms of correlation supported the observation that combinations of parameters are more sensitive in detecting high rainfall rates produced by low cloud top temperatures. The results of an inter-comparison between the MTSAT rainfall estimation and the TRMM 3B42 data product indicate that the TRMM 3B42 data product was more scattered than

MTSAT rainfall estimations indicates by the lower correlations than those for the MTSAT rainfall estimations. The bias and RMSE of TRMM 3B42 are generally larger than the MTSAT rainfall estimations. These results suggest that MTSAT rainfall estimations perform better than the TRMM 3B42 data product.

**Key objective 2:** *To characterize rainfall severity using geostationary based rainfall estimation through regional frequency analysis of long-term histrorical maximum rainfall.*

**Geostationary satellite based rainfall severity assessment.**

This chapter deals with the use of observed rainfall long-term historical data for generating regional frequency distribution which is eventually coupled with near-real time geostationary satellite based rainfall estimation for characterizing storm severity. The appropriate extreme frequency distribution is used to assess the return period and combined with the remote sensing rainfall estimation to monitor the distribution of extreme rainfall event severity. The long-term rainfall record from point measurement by rain gauge is used to describe the frequency distribution of the location of gauge stations. The Hosking and Wallis Regional frequency analysis (HW-RFA) is used to estimate the regional frequency distribution over a defined region.

The distribution of 1-hour long-term average maximum rainfall in Hokkaido region seems to be influenced by the topography since the western part has higher maximum rainfall than the eastern part which is clearly divided by the mountain ridges. These sub-regions are considered as 'the region' for RFA. The heterogeneity measure confirms that both sub-regions are acceptably homogeneous. The Z-statistics analysis confirms that the GNO/PE3 distribution is suitable for both region western and eastern part of Hokkaido Island.

The RFA result indicates that GNO/LN3 distribution is suitable to describe the frequency distribution of maximum rainfall event in two sub regions in Hokkaido Island. For the heavy rainfall event on 23 August 2010 at 20:30 UTC, it shows that the maximum return period for MTSAT estimated rainfall and AMeDAS interpolated rainfall is 5 year and 3 year which corresponds with the maximum estimated rainfall. This comparison demonstrates that that the return period information shown by MTSAT rainfall is comparable with AMeDAS rainfall return period. For assessing the return period of an extreme event in the area that observed rainfall is lacking, the use of geostationary satellite based is proved useful to overcome such problem.

**Key objective 3:** *To develop and evaluate a statistical empirical model of flash flood severity as a function of hydrolocigal, morphometrical and meteorological condition of the catchments. The meteorological condition is represented by the geostationary satellite based rainfall estimation*.

**Empirical regression based approach combined with rainfall estimation for flash flood severity assessment**

In this chapter, the flash floods risk is identified based on the potential of flash floods occurrence in particular catchments area. The catchments that potential in producing flash floods are represented by their relative flash flood severity. Flash floods are considered severe when they have relative high magnitude and high rising hydrograph gradient. Flash floods as the output of a catchment system are determined by meteorological, hydrological factor such as slope, land use, geology and by hydraulic processes related to the morphology of stream. Because flash floods are resulted as the response of the catchments to the rainfall that is controlled by the hydrological and morphologic factors, thus they can be used as the proxies to determined flash flood severity.

The regression analysis between FI and morphometrical parameters at 16 catchments indicates that it closely related to the shape factors (i.e. circularity ratio and elongation ratio) and the topographical factors (i.e. basin mean wide, relief ratio and Melton's ruggedness number). Particularly for hydrological and meteorological characterization, the analysis has been focused on five catchments area. The initial soil moisture condition has been evaluated by using scatter plot of total rainfall vs. total loss rainfall for all flood events during the months that the biggest flash floods took place during 1998 – 2010 summer periods. The result shows that initial soil moisture condition was reasonably influencing the relationship between variable contributing areas with flash flood severity index. Moderately strong relationship between the variable contributing area and flash flood severity index is shown in situation of relatively wet soil moisture initial condition. In the relatively dry soil moisture condition, it was difficult to find pattern between variable contributing area and flash flood severity index. This result suggests that the accurate identification of initial soil moisture condition is important increase the predictability of flash flood event. For the meteorological characterization, two rainfall properties has been evaluated i.e. rainfall intensity and rainfall location index. However the results show that only rainfall intensity demonstrates strong relationship with flash flood severity index. The implementation of the empirical models at Toyohira basin shows that FI as the function of morphometrical factors can provide flash flood potential information. Moreover, FI as the function of hydrological and meteorological factors demonstrate more dynamic pattern since they are related to rainfall intensity distribution.

**Key objective 4:** *To evaluate the performance of the geostationary satellite based rainfall estimation compared with the other sources of rainfall as the forcing for flash flood simulation using land surface model.*

**Physical based approach driven by rainfall estimation for flash flood estimation**

In this chapter the flash floods are assessed by implementing a land surface model called the Minimal Advance Treatments of Surface Interaction and Runoff (MATSIRO). MATSIRO uses physical process to draw the hydrometeorological characteristics of a region which is expressed by the energy balance model and the water balance model. Based on those two models, the surface energy flux and land surface interaction among main hydrological components (i.e. precipitation, evapotranspiration, moisture storage and surface flow) can be comprehensively evaluated. Rainfall estimation by using MTSAT satellite is applied as forcing data into MATSIRO model along with some parameters that generated by remote sensing data such as topography, river network, and vegetation characteristics. Since the estimated rainfall output was preserving the native resolution of MTSAT image (approximately 5 km grid), a statistical downscaling method was conducted to convert the data into 1 km grid size. Here the rainfall estimation from satellite is merged with the observed rainfall. The downscaling process aims to combine the advantage of those two rainfall data capture systems.

The area average of rainfall from both downscaled and observed is calculated and plotted into a scatter plot for two catchments area namely Shirai and Bebetsugawa river. Those data demonstrate strong relationship, even though the MTSAT downscaled tends to have higher rainfall amount compare with the observed rainfall. One of the reason is because the MTSAT downscaling is more homogenous in showing high rainfall distribution over the catchment than the observed rainfall that show more locally.

Three simulations are performed to estimate the river flow by using MATSIRO. First simulation is conducted by using rainfall data forcing from AMeDAS observation during period of 1 Jan – 31 Dec 2010. The second simulation is started from 1 June to 30 Sep 2010 by using rainfall forcing from downscaled MTSAT rainfall estimation. The third simulation is started from 1 June to 30 Sep 2010 by using rainfall forcing from MLIT observation. The estimated river flow derived from observed rainfall and estimated rainfall then compared with observe discharge for August 2010. The river flow simulations results demonstrate that estimated discharge using MLIT rainfall is the best for predicting peak discharge compared with the others. However, MTSAT downscaled demonstrate more advantage as input forcing in a physically based model because the accuracy is about comparable with the relatively dense rain gauge network such as the

MLIT. Moreover, the sparse rain gauges are commonly found in many places rather that the dense raingauge network and this situation has been proved that can be overcome by merge them with the MTSAT rainfall estimation.

## 8.2. RECOMMENDATIONS

As the recommendation for future study, some issues are addresses for future development of the application of geostationary satellite based rainfall estimation and rainfall-runoff model for flash flood assessment which briefly describes as follow:

1. For the rainfall estimation using MTSAT IR1 image, the recommendations are:
   a. Add more storm cases (spatially and temporally) for BT and RR statistical relationship development.
   b. Conduct a comparison study of the use several atmospheric vertical instability such as K-index (KINT), Lifted Index (LIFT) and Convective Available Potential Energy (CAPE) for BT and RR statistical relationship development.

2. For the physical based model for flash flood simulation, it is recommended to investigate the use remote sensing based soil moisture for prescribing more realistic moisture status in MATSIRO.

3. For the empirical based model flash flood severity assessment, it is suggested to use more sample flash flood events in more various background of land surface condition. Include some flash flood hazard prevention as land surface characteristics.

4. Apply and evaluated the framework methodology (both satellite based rainfall estimation and flash flood assessment) in a tropical region which is the occurrence of convective rainfall caused by Cb cloud is more frequent and prone to flash floods hazard.

# REFERENCES

Alfieri, L., J. Thielen, F. Pappenbeger, Ensemble hydro-meteorological simulation for flash flood early detection in Southern Switzerland, *J. Hydrol*., DOI:10.1016/j.hydrol.2011.12.038, 2012.

Awadallah, A. G., M. ElGamal, A. ElMostafa, H. ElBadry, Developing intensity-duration-frequency curves in scarce data region: An approach using regional analysis and satellite data, *Engineering, 3*, 215 – 226, DOI: 10.4236/eng.2011.33025, 2011.

Baskar, N. R., M. N. French, G. K. Kiyamah, Characterization of flash flood in Eastern Kentucky, *J. of Hydrologic Eng, 5,* 327 – 331, 2000.

Beven, K. J., and M. J. Kirkby, A physically based, contributing area model of basin hydrology, *Hydrol. Sci. J.,* 43 - 69, 1979.

Bolle, H. J., Validation of thin cirrus and low cloud cover over snow by means of maximum likelihood method. *Advance Space Research, 5*, 169–175, 1985.

Choi, Y.-S., and Hoi, H.C., Validation of cloud property retrievals from MTSAT-1R imagery using MODIS observations. *Int. J. Remote Sensing, 30*, 5935–5958, 2009.

Conway, E. D., *An introduction to satellite image interpretation*, The John Hopkins University Press, 1997.

Dawod, G. M., M. N. Mirza, K. A. Al-Ghamdi, GIS-based spatial mapping of flash flood hazard in Makkah City, Saudi Arabia. DOI:10.4236/jgis.2011.33019, 2011.

Dingman, L. S., *Physical Hydrology*, Prentice Hall, 2002.

Doswell III, C. A, Flash flood production convective storms: Current understanding and research, *Join workshop on Natural Hazard*, Barcelona, Spain, 8-11 June 1993, 1993.

Doswell III, C. A., H. E. Brooks, R. A. Maddox, Flash flood forecasting: An ingredient based methodology, *Wea. Forecast ,11*, 560– 581, 1996.

Ebert, E. E., *Forecast Verification-Issues, Methods and FAQ*, [http://www.bom.gov.au/bmrc/wefor/staff/eee/verif/verif_web_page.html], accessed: 28 August, 2007.

Ebert, E. E., and M. J. Manton, Performance of Satellite Rainfall Estimation Algorithm during TOGA COARE, *J. Atmos. Sci.,* 55, 1537 - 1557, 1998.

Edreny, Theodore A., N. Imbeah, Generating robust rainfall intensity-duration-frequency estimates with short record satellite data, *J. Hydrol., 371*, 182 – 191, 2009.

Feidas, H. N., C. Cartalis, A.P. Cracknell, Use of Meteosat imagery to define clouds linked with floods in Greece. *Int. J. Remote Sensing*, *21*, 1047–1072. 2000.

Feidas, H., and C. Cartalis, Monitoring mesoscale convective cloud systems associated with heavy storms using Meteosat imagery. *J. Appl. Meteor*., *40*, 491–512, 2001.

Geogarkakos, K. P., On the design of national, real-time warning system with capability for site specific, flash flood forecasts, *Bull. Amer. Meteor. Soc.*, *67*, 1233 – 1239, 1986.

Grimes, D. I. F., E. Pardo-Iguzquiza, R. Bonifacio., Optimal areal rainfall estimation using raingauges and satellite data, *J. Hydrol*., *222*, 93 – 108, 1999.

Haile, A. T., T. Rientjes, A. Gieske, M. Gebremichael, Multispectral remote sensing for rainfall detection and estimation at the source of the Blue Nile river. *Int. J. Appl. Earth Obs. Geoinfo*., *12S*, S76-S82, 2010.

Haile, A. T., Rainfall variability and estimation for hydrologic modeling, *PhD dissertation*, *University of Twente*, 2011.

Hamada, A. and N. Nishi, Development of a cloud-top height estimation method by geostationary satellite split-window measurement trained with CloudSat data, *J. Appl. Meteor. Clim*., *49*, 2035-2049, 2010.

Hapuarachchi, H. A. P., Q. J. Wang and T. C. Pagano, A review of advances in flash flood forecasting, *Hydrol. Process*., *25*, 2771 – 2784, 2011.

Heinemann, T., A. Lattanzio, F. Roveda., *The Eumetsat Multi-sensor Precipitation Estimate (MPE)*,[http://www.eumetsat.int/groups/ops/documents/document/mpe_introduction_ipwg_2002.pdf], Retrieved: 20 April 2008.

Hosking, J.R.M., J. R. Wallis, *Regional Frequency Analysis*, Cambridge University Press, 1997.

Huffman, G. J., R. F. Adler, D. T. Bolvin, G. Gu, E. J. Nelkin, K. P. Bowman, Y. Hong, E. F. Stocker, D. B. Wolff, The TRMM Multi-satellite Precipitation Analysis (TMPA): quasi-global, multiyear, combined-sensor precipitation estimates at fine scales. *J. Hydromet.*, *8*, 112-130, 2007.

Inoue, T., An instantaneous delineation of convective rainfall areas using split window data of NOAA-7 AVHRR, *Japan of Meteorological Society*, *65*, 469 – 480, 1987.

Inoue, T., Features of clouds over the Tropical Pacific during Northern Hemisphere Winter derived from split window measurements, *Japan of Meteorological Society*, *67*, 621 – 637, 1989.

Inoue, T. and K. Aonashi, A comparison of cloud and rainfall information from instantaneous visible and infrared scanner and precipitation radar observations over a frontal zone in East Asia during June 1998, *J. of Appl. Meteorol.*, *39*, 2292 – 2301, 2000.

Iwabuchi, T., C. Roken, L. Mervart, M. Kanzaki, Nowcasting and weather forecasting, Real time estimation of ZTD in GEONET, Japan, *Location*, *1*, 44- 49, 2006.

Jensen, J. R., *Introductory Digital Image Processing: a remote sensing perspective*, Pearson Prentice Hall, 2005.

Japan Meteorological Agency (JMA), *Analysis and use of meteorological satellite images*. [http://rammb.cira.colostate.edu/wmovl/VRL/Texts/general_texts.htm], accessed: 11 April 2011, 2002.

Japan Meteorological Agency (JMA), *Information about the use of the northwestern Pacific Ocean cloud cover grid point (in Japanese)*, Japan Meteorological Agency, 2007.

Japan Meteorological Agency (JMA), Daily weather map of Japan, *Tenki*, Vol. 57(1), 34-35, 2010.

Kerkmann, J., *Meteorological use of The Seviri IR 3.9 channel*, [http://oiswww.eumetsat.org/WEBOPS/msg_interpretation/PowerPoints/Channels/Channel_IR39.ppt], accessed: 13 April 2011, 2004.

Kidd, C., V. Levizzani, Status of satellite precipitation retrievals, *Hydrol. Earth Syst. Sci.*,*15* 1109–1116, 2011.

Kim, E. S., H. I. Choi, Assessment of vulnerability to extreme flash floods in design storm, *Int. J. Environ. Res. Publich Health*, *8*, 2907– 2922, 2011.

Kim, E. S., H. I. Choi, Estimation of the relative severity of floods in small ungauged catchments for preliminary observation on Flash flood preparedness: A case study in Korea, *Int. J. Environ. Res. Publich Health*, *9*, 1507– 1522, 2012.

Kinoti, J.., Z. Su, T. Woldai, B. Maathuis, Estimation of spatial-temporal rainfall distribution using remote sensing techniques: A case study of Makanya catchment, Tanzania, *Int. J. of App. Earth Obsv. and Geoinfo, 12S* ,S90 – S99, 2010.

Kochi University, *GMS/GOES9/MTSAT Data Archive for Research and Education*, [http://weather.is.kochi-u.ac.jp/archive-e.html], accessed: August 2011, 2011.

Kuligowski, R., *Remote Sensing in Hydrology*, [http://www.weather.gov/iao/InternationalHydrologyCourseCD1/1029/wmo_bk.ppt], accessed: 4 November 2007, 2003.

Kure, S. and T. Yamada, A study of the non-linearity of runoff phenomena and estimation of effective rainfall, Proceedings of the 2nd Asia Pacific Association of Hydrology and Water Resources Conference,2,76-85, 2004

Lensky, I. M. and D. Rosenfeld, A night rain delineation algorithm for infrared satellite data based on microphysical considerations, *J. of Appl. Meteorol*., *42*, 1218 – 1226, 2003.

Lensky, I. M. and D. Rosenfeld, Clouds-Aerosols-Precipitation Satellite Analysis Tool (CAPSAT). *Atmospheric Chemistry and Physics*, *8*, 6739–6753, 2008.

Levizani, V. R. Amorati, F. Meneguzzo, A review of satellite based rainfall estimation methods, *MUSIC-Multiple Sensor Precipitation Measurements, Integration, Calibration and Flood Forecasting*, EU, 2002.

Lewis, M. A., C. S. Cheney, B. E. ODochartaigh, Guide to Permeability Indices, *British Geological Survey Open Report*, CR/06/160N, 2006

Liu, Y., Xia, J., Shi, C. X., and Hong, Y., An improved cloud classification algorithm for China's FY-2C multi-channel images using artificial neural network, *Sensor*, *9*, 5558–5579, 2009.

Maathuis, B. H. P., A.S.M Gieske, V. Resios, B.V. Leeuwen, C.M. Mannaerts, J.H.M Hendrikse, Meteosat-8 From temperature to rainfall, *ISPRS Commission VII Mid-term symposium Remote sensing: from pixel to processes*, *Enschede*, *The Netherlands*, 2006.

Maathuis, B. H. P., and L. Wang, Digital Elevation Model based Hydro-processing, *Geocarto International*, *21*, 21 – 26, 2008.

Misra, J.K. and O.P. Sharma, Cloud top temperature based precipitation intensity estimation using INSAT-1D data, *Int. J. Remote Sensing*, *22*, 969 – 985, 2001.

NRC, *Flash Flood Forecasting Over Complex Terrain With an Assessment of the Sulphur Mountain NEXRAD in Southern California*, The National Academies Press, 2005.

Norbiato, D., M. Borga, M. Sangati, F. Zanon, Regional frequency analysis of extreme precipitation in the eastern Italian alps and the August 29, 2003 flash flood, *J. Hydrol. 345*, 149 – 166, 2003.

Norbiato, D., M. Borga, S. D. Esposti, E. Gaume, S. Anquetin, Flash flood warning based on rainfall threshold and soil moisture condition: An assessment for gauged and ungauged basins, *J. Hydrol. 362*, 274 – 290, 20038.

Oki, T. Y. and C. Sud, Design of Total Runoff Integrating Pathways (TRIP)-A global river channel network, *Earth Interactions*, 2, 1 – 36, 1998.

Perucha, L. P., Y. E. Angilieri, Morphometric characterization of del Molle Basin applied to the evaluation of flash flood hazard, Inglesia Department, San Juan, Argentina, *Qua. Int*. DOI: 10.1016/j.quaint.2010.08.007, 2010.

Pokhrel, Y. N., Study of the global terrestrial water cycle using a land surface model with representation of human impacts, *PhD dissertation*, *Univ. of Tokyo*, 2011.

Rogerson, P. A., *Statistical Method for Geography*, SAGE Publications, 2006.

Saito, K., T. Fujita, Y. Yamada, J. Ishida, Y. Kumagai, K. Aranami, S. Ohmori, R. Nagasawa, S. Kumagai, C. Muroi, T. Kato, H. Eito, Y. Yamazaki, The operational JMA nonhydrostatic mesoscale model, *Mon. Wea. Rev*, *134*, 1266 – 1298, 2006.

Saunders, R. W., An improved method for detecting clear sky and cloudy radiances form AVHRR data, *Int. J. Remote Sensing*, *9*, 123 – 150, 1988.

SCTV, Liputan 6, from www.liputan6.com, 2008.

Seyhan. E., *Calculation of runoff from basin physiography*, Geografisch Institut Rijksuniversiteit Utrech, 1976.

Shi, C., Wenjian, Z., Wei, G., and Liyang, Z., Study on cloud classifications by using AVHRR, GMS-5 and Terra/MODIS satellite data, [http://cimss.ssec.wisc.edu/itwg/itsc14/proceedings/A06_shi.pdf], accessed: 25 Jan 2011, 2005.

Smith, M. B., V. I. Koren, Z. Zhang, S. M. Reed, J. J. Pan, F. Moreda, Runoff response to spatial variability in precipitation: an analysis of observed data, *J. Hydrol*., *298*, 267– 286, 2004.

Sorooshian, S., K.-L. Hsu, X. Gao, H. V. Gupta, B. Imam, D. Braithwaite, Evaluation of PERSIANN system satellite-based estimates of tropical rainfall, *Bull. Amer. Meteor. Soc.*, *81*, 2035 – 2046, 2000.

Suseno, D. P. Y., and T. J. Yamada, Geostationary Satellite Based Rainfall Estimation and Validation: A Case Study of Java Island, Indonesia, *J. of Japan Soc. of Civil Eng*., *55*, I_175–I_180, 2011a.

Suseno, D. P. Y., and T. J. Yamada, The Use of Cloud Type Classification To Improve Geostationary Based Rainfall Estimation, *9th International Symposium on Southeast Asian Water Environment*, Dec 1st-3rd 2011 Bangkok City, Thailand, 2011b.

Suseno, D. P. Y., and T. J. Yamada, The use of geostationary based rainfall estimation for characterizing storm severity, *J. of Japan Soc. of Civil Eng.*, *68*, I_175– I_180, 2012a.

Suseno, D. P. Y., and T. J. Yamada, Two-dimensional, threshold-based cloud type classification using MTSAT data, *Remote Sensing Letters*, *3*, 737 – 746, 2012b.

Suseno, D. P. Y., and T. J. Yamada, The role of GPS precipitable water vapor and atmospheric vertical stability index in the statistically-based rainfall estimation using MTSAT data, submitted to J. of Hydrometerol. (accepted), 2013a.

Suseno, D. P. Y., and T. J. Yamada, The use of Geostationary Satellite Based Rainfall Estimation Combined With Land Surface Model for Regional Flash Flood Assessment, to be presented on *The 6th conference of The Asia Pacific Association of Hydrology and Water Resources*, Seoul, Korea, 2013b.

Takata, K., S. Emori, T. Watanabe, Development of the minimal advance treatments of surface interaction and runoff, *Global and Planetary Change*, *38*, 209 – 222, 2003.

Takeuchi W., T. Nemoto, T. Kaneko and T. Yasuoka, Development of MTSAT data processing, distribution and visualization system on WWW, *Asian Journal of Geoinformatics*, *10*, 29–33. 2010.

Vicente, G. A., R.A. Scofield, W. P. Menzel, The Operational GOES Infrared Rainfall Estimation Technique, *Bull. Amer. Meteor. Soc*, *79*, 1883 – 1898, 1998.

Vicente, G. A., J. C. Devenport and R. A. Scofield, The role of orographic and parallax correction on real time high resolution satellite rainfall rate distribution. *Int. J. Remote Sensing*., *23*, 221 - 230, 2002

Viessman, W, T. R. Harbaugh, J. W. Knapp, *Introduction to Hydrology*, Intext Educational Publishers, 1972

Vila, D. A., L. G. Goncalves, D. L. Toll, J. B. Rozante, Statistical Evaluation of Combined Daily Gauge Observation and Rainfall Satellite Estimates over Continental South America, *J. of Hydrometeorol*,*10*, 533 – 543, 2009.

Wardah, T., S.H. Abu Bakar, A. Bardosy, M. Maznorian, Use of geostationary meteorological satellite images in convective rain estimation for flash-flood forecasting. *J. Hydrol*., *356*, 283-298, 2008.

Yamada, T. J., J. Sasaki, N. Matsuoka, Climatology of line-shaped rainbands over northern Japan in boreal summer between 1990 and 2010, *Atmos. Sci. Let, 13*, 133-138, 2012.

Yousef, A. M., B. Pradhan, A. M. Hassan, Flash flood risk estimation along the St. Katherine road, southern Sinai, Egypt using GIS based morphometry and satellite imagery, *Environ. Earth Sci*, DOI: 10.1007/s12665-010-0551-1, 2010.

# APPENDICES

**Appendix 1.** Program source code for creating cloud height map from MTSAT

Compiler: FreeBASIC

```
'program to classify cloud height using IR1 and IR2 or MTSAT (ASCII format)
'reference:
'Hamada, A. and N. Nishi, 2010: Development of a cloud-top height estimation method by
'geostationary satellite split-window measurement trained with CloudSat data,
'J. Appl. Meteor. Clim., 49, 2035-2049
'=================================================================="
' usage: cloudhgt IR1filename.asc IR2filename.asc"
' example: cloudhgt MTS211070100IR1.asc MTS211070100IR2.asc"
' output: hgt11070100.asc"
' prepared by: Dwi Prabowo YS"
'     Nov, 22, 2011"
'=================================================================="
dim twodim(20,24)
'open the IR1 image
open command$(1) for input as #1
'open the IR2 image
open command$(2) for input as #2
open "2dheight.dat" for input as #4

'open the IRclear image
open "ir1clear.asc" for input as #7

'open the land-sea map
open "landsea.asc" for input as #8

'open a file to save the output
fileout1$ = mid$(command$(2),5,8)
open "cloudelev.asc" for output as #3

'open the two dimenstional threshold for cloud height classification
'based on Hamada et. al.
for i = 1 to 20
   for j = 1 to 24
      input #4, twodim(i,j)
   next j
next i

'open the header of IR1 image
input #1, h11$
input #1, h12$
input #1, h13$
input #1, h14$
input #1, h15$
input #1, h16$

'open the header of IR2 image
input #2, h21$
input #2, h22$
input #2, h23$
input #2, h24$
input #2, h25$
input #2, h26$

'open the header of IR1clear image
input #7, h31$
input #7, h32$
input #7, h33$
input #7, h34$
input #7, h35$
input #7, h36$

'open the header of  landsea image
input #8, h41$
input #8, h42$
input #8, h43$
input #8, h44$
input #8, h45$
input #8, h46$

'write the header of output
PRINT #3, h11$
PRINT #3, h12$
PRINT #3, h13$
```

```
PRINT #3, h14$
PRINT #3, h15$
PRINT #3, h16$

nrow=cvi(mid$(h11$, 7,3))
ncol=cvi(mid$(h12$, 7,3))

for i = 1 to nrow
   for j = 1 to ncol
     input #1, ir1
         input #2, ir2
         input #7, ir1clear
         input #8, landsea

         delta = ir1clear - ir1
         if(((landsea=1) and (delta > 20)) or ((landsea=0) and (delta > 7))) then
             cloudland = 1
         else
             cloudland = 0
     end if

         select case ir1
            case is < 190.00
                  ir1kelas = 1
            case 190.01 to 195.00
                  ir1kelas = 2
            case 195.01 to 200.00
                  ir1kelas = 3
            case 200.01 to 205.00
                  ir1kelas = 4
             case 205.01 to 210.00
                  ir1kelas = 5
            case 210.01 to 215.00
                  ir1kelas = 6
             case 215.01 to 220.00
                  ir1kelas = 7
            case 220.01 to 225.00
                  ir1kelas = 8
            case 225.01 to 230.00
                  ir1kelas = 9
             case 230.01 to 235.00
                  ir1kelas = 10
             case 235.01 to 240.00
                  ir1kelas = 11
            case 240.01 to 245.00
                  ir1kelas = 12
             case 245.01 to 250.00
                  ir1kelas = 13
             case 250.01 to 255.00
                  ir1kelas = 14
             case 255.01 to 260.00
                  ir1kelas = 15
            case 260.01 to 265.00
                  ir1kelas = 16
             case 265.01 to 270.00
                  ir1kelas = 17
             case 270.01 to 275.00
                  ir1kelas = 18
             case 275.01 to 280.00
                  ir1kelas = 19
            case 280.01 to 285.00
                  ir1kelas = 20
             case 285.01 to 290.00
                  ir1kelas = 21
             case 290.01 to 295.00
                  ir1kelas = 22
             case 295.01 to 300.00
                  ir1kelas = 23
            case 300.01 to 305.00
                  ir1kelas = 24
        end select

         btdif12 = ir1 - ir2

        select case btdif12
            case -2.00 to -1.5
                  btd12kelas = 1
            case -1.51 to -1.00
                 btd12kelas = 2
             case -1.01 to -0.5
                btd12kelas = 3
            case -0.51 to 0
                btd12kelas = 4
           case 0.01 to 0.50
                btd12kelas = 5
            case 0.51 to 1.00
                btd12kelas = 6
```

```
            case 1.01 to 1.50
                btd12kelas = 7
            case 1.51 to 2.00
                btd12kelas = 8
            case 2.01 to 2.50
                btd12kelas = 9
            case 2.51 to 3.00
                btd12kelas = 10
            case 3.01 to 3.50
                btd12kelas = 11
            case 3.51 to 4.00
                btd12kelas = 12
            case 4.01 to 4.50
                btd12kelas = 13
            case 4.51 to 5.00
                btd12kelas = 14
            case 5.01 to 5.50
                btd12kelas = 15
            case 5.51 to 6.00
                btd12kelas = 16
            case 6.01 to 6.50
                btd12kelas = 17
            case 6.51 to 7.00
                btd12kelas = 18
            case 7.01 to 7.50
                btd12kelas = 19
            case 7.51 to 20.00
                btd12kelas = 20
            end select
            cloudheight = twodim(btd12kelas,ir1kelas)
        if cloudland = 1 then
            cloudclass2 = cloudheight
        else
            cloudclass2 = 0
    end if
        print #3, cloudclass2;
  next j
  print #3,
  next i
print "process complete..."
close
end
```

## Content of 2dheight.dat file

| | | | | | | | | | | | | | | | | | | | | | | | |
|---|---|---|---|---|---|---|---|---|---|---|---|---|---|---|---|---|---|---|---|---|---|---|---|
| 0 | 0 | 0 | 0 | 0 | 16 | 15 | 14 | 14 | 14 | 0 | 0 | 0 | 0 | 0 | 0 | 0 | 0 | 0 | 0 | 0 | 0 | 0 | 0 |
| 0 | 17 | 17 | 16 | 16 | 16 | 15 | 14 | 14 | 14 | 13 | 13 | 0 | 0 | 0 | 0 | 0 | 0 | 0 | 0 | 0 | 0 | 0 | 0 |
| 0 | 17 | 17 | 16 | 16 | 16 | 15 | 14 | 14 | 14 | 13 | 13 | 12 | 11 | 10 | 9 | 0 | 0 | 0 | 0 | 0 | 0 | 0 | 0 |
| 18 | 17 | 17 | 16 | 16 | 16 | 15 | 15 | 14 | 14 | 13 | 13 | 12 | 11 | 10 | 9 | 8 | 8 | 8 | 8 | 8 | 0 | 8 | 0 |
| 18 | 18 | 17 | 16 | 16 | 16 | 15 | 15 | 14 | 14 | 13 | 13 | 12 | 11 | 10 | 9 | 8 | 8 | 8 | 8 | 8 | 8 | 8 | 0 |
| 0 | 18 | 17 | 16 | 16 | 16 | 15 | 15 | 14 | 14 | 14 | 13 | 12 | 12 | 11 | 9 | 9 | 8 | 8 | 8 | 8 | 8 | 8 | 8 |
| 0 | 0 | 17 | 17 | 16 | 16 | 15 | 15 | 15 | 14 | 14 | 13 | 13 | 12 | 11 | 10 | 9 | 8 | 8 | 8 | 8 | 8 | 8 | 0 |
| 0 | 0 | 0 | 0 | 16 | 16 | 15 | 15 | 15 | 14 | 14 | 13 | 13 | 12 | 11 | 10 | 9 | 8 | 8 | 8 | 8 | 8 | 8 | 0 |
| 0 | 0 | 0 | 0 | 0 | 16 | 16 | 15 | 15 | 15 | 14 | 14 | 13 | 13 | 12 | 11 | 10 | 9 | 8 | 8 | 8 | 8 | 8 | 0 |
| 0 | 0 | 0 | 0 | 0 | 16 | 16 | 16 | 15 | 15 | 15 | 14 | 14 | 13 | 12 | 12 | 11 | 10 | 9 | 8 | 8 | 8 | 8 | 0 |
| 0 | 0 | 0 | 0 | 0 | 0 | 16 | 16 | 16 | 15 | 15 | 14 | 14 | 13 | 13 | 12 | 11 | 10 | 9 | 8 | 8 | 8 | 8 | 0 |
| 0 | 0 | 0 | 0 | 0 | 0 | 0 | 0 | 16 | 15 | 15 | 15 | 14 | 14 | 13 | 12 | 12 | 11 | 10 | 8 | 8 | 8 | 8 | 0 |
| 0 | 0 | 0 | 0 | 0 | 0 | 0 | 0 | 16 | 15 | 15 | 15 | 15 | 14 | 14 | 13 | 12 | 11 | 10 | 8 | 8 | 8 | 0 | 0 |
| 0 | 0 | 0 | 0 | 0 | 0 | 0 | 0 | 0 | 15 | 15 | 15 | 15 | 15 | 14 | 13 | 12 | 11 | 9 | 8 | 8 | 8 | 0 | 0 |
| 0 | 0 | 0 | 0 | 0 | 0 | 0 | 0 | 0 | 0 | 15 | 15 | 15 | 15 | 14 | 14 | 13 | 11 | 9 | 8 | 8 | 8 | 0 | 0 |
| 0 | 0 | 0 | 0 | 0 | 0 | 0 | 0 | 0 | 0 | 0 | 15 | 15 | 15 | 15 | 14 | 13 | 10 | 8 | 8 | 8 | 0 | 0 | 0 |
| 0 | 0 | 0 | 0 | 0 | 0 | 0 | 0 | 0 | 0 | 0 | 0 | 0 | 0 | 15 | 14 | 13 | 9 | 8 | 8 | 0 | 0 | 0 | 0 |
| 0 | 0 | 0 | 0 | 0 | 0 | 0 | 0 | 0 | 0 | 0 | 0 | 0 | 0 | 0 | 0 | 0 | 8 | 0 | 0 | 0 | 0 | 0 | 0 |
| 0 | 0 | 0 | 0 | 0 | 0 | 0 | 0 | 0 | 0 | 0 | 0 | 0 | 0 | 0 | 0 | 0 | 0 | 0 | 0 | 0 | 0 | 0 | 0 |

**Appendix 2.** Program source code for converting ASCII grid (row and column format) into XYZ format

## Compiler: FreeBASIC

```
'program to convert ASCII grid (row column format) into xyz format
'for ir1, ir2 and ir3 MTSAT image
' Prepapred by: Dwi Prabowo YS
'==========================================================
cls
dim cols, rows as integer
dim xll, yll, cell as single
dim xinit, yinit, xpos, ypos as single
open "ir1x.asc" for input as #1
open "ir2x.asc" for input as #2
open "cloudelev.asc" for input as #3
open "ir1x.dat" for output as #4
open "ir2x.dat" for output as #5
open "elev.dat" for output as #6
input #1, h11$
input #1, h12$
input #1, h13$
input #1, h14$
input #1, h15$
input #1, h16$

input #2, h21$
input #2, h22$
input #2, h23$
input #2, h24$
input #2, h25$
input #2, h26$

input #3, h31$
input #3, h32$
input #3, h33$
input #3, h34$
input #3, h35$
input #3, h36$
cols = val(mid$(h11$, 7, 4))
rows = val(mid$(h12$, 7, 4))
xll = val(mid$(h13$, 11, 8))
yll = val(mid$(h14$, 11, 8))
cell = val(mid$(h15$, 10, 6))
xinit = xll + (0.5*0.0334)
yinit = (yll + (cint(rows * cell))) - 0.0366

print cols, rows
print xinit, yinit
print cell

print "process is progress..."

for i= 1 to rows
   ypos = yinit - (cell*(i-1))
   line input #1, a1$
   line input #2, a2$
   line input #3, a3$
   k = 1
   for j = 1 to cols
      xpos = xinit + (cell*(j-1))
      cellval1 = val(mid$(a1$,k,8))
         cellval2 = val(mid$(a2$,k,8))
         cellval3 = val(mid$(a3$,k,8))

      write #4, xpos, ypos, cellval1
         write #5, xpos, ypos, cellval2
         write #6, xpos, ypos, cellval3

      k = (j*8)+1
   next j
next i
close
end
```

**Appendix 3.** Program source code for conducting parallax correction of MTSAT images (IR1 and IR2). The parallax subroutine is downloaded from:
ftp://ftp.eumetsat.int/pub/MET/out/marianne/parallax_tables/parallax.f90

Compiler: FOTRAN95

```
program parallax_ver1
      implicit none
      !declare variables
      character(len=20) :: file
      integer :: status, ierror
      real :: x1, y1, z, z1
      real :: x2, y2, temp1, temp2
      real :: satlat1, satlon1, satheight1
      real :: xcor,ycor

      !MTSAT 1R parameters
      satlat1 = 0.0
      satlon1 = 140.0
      satheight1 = 35800

      !MTSAT 1R parameters
      !satlat1 = 0.0
      !satlon1 = 145.0
      !satheight1 = 35800

      open (unit=8, file='elev.dat', status='old', iostat=ierror)
      open (unit=7, file='ir1x.dat', status='old', iostat=ierror)
      open (unit=9, file='ir2x.dat', status='old', iostat=ierror)
      open (unit=10, file='ir1cor.dat', status='replace', iostat=ierror)
      open (unit=11, file='ir2cor.dat', status='replace', iostat=ierror)

      readloop: do
      read (7,*,iostat=status) x1, y1, temp1
      read (9,*,iostat=status) x1, y1, temp2
      read (8,*,iostat=status) x2, y2, z1
      if (status /=0) exit
      !z1=z/1000
      call parallax(satheight1,satlat1,satlon1,z1,y1, x1, ycor, xcor)
      write (10,*) xcor, ycor, temp1
      write (11,*) xcor, ycor, temp2
      end do readloop
      end program

      SUBROUTINE parallax (sheight,slat,slon,height,lat,lon,lat1,lon1)
!     Subroutine does a parallax correction for something seen at some
!     height in a position lat/lon by the satellite given by satheight,
!     satlat, satlon
!     The new coordinates are returned in latcorr and loncorr
!     Input:
!     satheight (REAL): height of the satellite in km
!     satlat (REAL): subsatellite latitude (deg, N is positive)
!     satlon (REAL): subsatellite longitude (deg, E is positive)
!     height (REAL): height of the cloud (km)
!     lat (REAL): latitude of the satellite pixel (N is positive)
!     lon (REAL): longitude of the satellite pixel (E is positive)
!     Output:
!     latcorr (REAL): corrected latitude accounting for parallax shift (N positive)
!     loncorr (REAL): corrected longitude accounting for parallax shift (E positive)
!     from: ftp://ftp.eumetsat.int/pub/MET/out/marianne/parallax_tables/parallax.f90
!     7 feb 2011
      IMPLICIT NONE
      REAL :: sheight,slat,slon
      REAL :: lat,lon,height
      REAL :: latcorr,loncorr
      REAL :: lat1,lon1
      REAL(KIND=8) :: dpi
      REAL(KIND=8) :: rd_eq
      REAL(KIND=8) :: rd_pole
      REAL(KIND=8) :: rd_ratio
      REAL(KIND=8) :: mean_rd
      REAL(KIND=8) :: dheight
      REAL(KIND=8) :: alat,alon
      REAL(KIND=8) :: asatlat,asatlon
```

```
      REAL(KIND=8) :: satlat_gd,satlon_gd
      REAL(KIND=8) :: xsat,ysat,zsat
      REAL(KIND=8) :: xsurf,ysurf,zsurf
      REAL(KIND=8) :: alat_gd
      REAL(KIND=8) :: rd_surf
      REAL(KIND=8) :: rd_ratio_local
      REAL(KIND=8) :: xdiff,ydiff,zdiff
      REAL(KIND=8) :: xfact,zen
      REAL(KIND=8) :: e1,e2,e3
      REAL(KIND=8) :: corr
      REAL(KIND=8) :: xcorr,ycorr,zcorr

      dpi = 3.14159265

!     varius earth radius information
      rd_eq = 6378.077
      dheight = sheight
      rd_pole = 6356.577
      rd_ratio = rd_eq/rd_pole
      mean_rd = 0.5*(rd_eq+rd_pole)
      zdiff = 0.0

!     angle conversion to radians
      asatlat = slat * dpi/180.0
      asatlon = slon * dpi/180.0
      alat = lat*dpi/180.0
      alon = lon*dpi/180.0

!     cartesian coordinates for the satellite
!     satlat_geod is the geodetic satellite latitude
      satlat_gd = ATAN(TAN(asatlat)*rd_ratio**2)
      xsat = dheight * DCOS(satlat_gd) * DSIN(asatlon)
      ysat = dheight * DSIN(satlat_gd)
      zsat = dheight * DCOS(satlat_gd) * DCOS(asatlon)

!     cartesian coordinates of the surface point
      alat_gd = ATAN(TAN(alat)*rd_ratio**2)
      rd_surf=rd_eq/SQRT(COS(alat_gd)**2+rd_ratio**2*DSIN(alat_gd)**2)
      xsurf = rd_surf * DCOS(alat_gd) * DSIN(alon)
      ysurf = rd_surf * DSIN(alat_gd)
      zsurf = rd_surf * DCOS(alat_gd) * DCOS(alon)

!     compute new radius ratio depending on height
      rd_ratio_local = ((rd_eq+height)/(rd_pole+height))**2

!     Satellite minus surface location
      xdiff = xsat - xsurf
      ydiff = ysat - ysurf
      zdiff = zsat - zdiff

!     compute local zenith angle
      xfact = SQRT(xdiff**2 + ydiff**2 + zdiff**2)
      zen = (xdiff*xsurf+ydiff*ysurf+zdiff*zsurf)/(mean_rd*xfact)
      zen = ACOS(zen)
      zen = zen*180.0/dpi

!     equation to solve for the line of sight at height Z
      e1 = xdiff**2 + rd_ratio_local*ydiff**2 + zdiff**2
      e2 = 2.0 * (xsurf*xdiff + rd_ratio_local*ysurf*ydiff +zsurf*zdiff)
      e3 =xsurf**2+zsurf**2 + rd_ratio_local*ysurf**2 -(rd_eq+height)**2

      corr = (SQRT(e2**2 - 4.0*e1*e3) - e2)/2.0/e1

!     corrected surface coordinates
      xcorr = xsurf + corr*xdiff
      ycorr = ysurf + corr*ydiff
      zcorr = zsurf + corr*zdiff

!     convert back to latitude and longitude
      lat1 = ATAN(ycorr/SQRT(xcorr**2 + zcorr**2))
      lat1 = ATAN(TAN(lat1)/rd_ratio**2) * 180.0/dpi
      lon1 = ATAN2(xcorr,zcorr) * 180.0/dpi

      RETURN
      end subroutine
```

**Appendix 4.** Typical of ILWIS script for performing cloud classification using parallax corrected MTSAT image.

```
//copy the data into the process folder
copy c:\MTSATrainest062010\MTSAT1R201006220630IR1  c:\MTSATproses\IR1
copy c:\MTSATrainest062010\MTSAT1R201006220630IR1.HDR  c:\MTSATproses\IR1.HDR
copy c:\MTSATrainest062010\MTSAT1R201006220630IR2  c:\MTSATproses\IR2
copy c:\MTSATrainest062010\MTSAT1R201006220630IR2.HDR  c:\MTSATproses\IR2.HDR
copy c:\MTSATrainest062010\MTSAT1R201006220630IR3  c:\MTSATproses\IR3
copy c:\MTSATrainest062010\MTSAT1R201006220630IR3.HDR  c:\MTSATproses\IR3.HDR
copy c:\MTSATrainest062010\MTSAT1R201006220630IR4  c:\MTSATproses\IR4
copy c:\MTSATrainest062010\MTSAT1R201006220630IR4.HDR  c:\MTSATproses\IR4.HDR

//import the MTSAT image from ENVI HDR format into ILWIS format
!gdal_translate.exe '-of' ILWIS 'IR1' 'xtemp1'
!gdal_translate.exe '-of' ILWIS 'IR2' 'xtemp2'
!gdal_translate.exe '-of' ILWIS 'IR3' 'xtemp3'
!gdal_translate.exe '-of' ILWIS 'IR4' 'xtemp4'
ir1x {dom=value.dom, vr=0.00:500.00:0.01} := xtemp1/100
ir2x {dom=value.dom, vr=0.00:500.00:0.01} := xtemp2/100
ir3x {dom=value.dom, vr=0.00:500.00:0.01} := xtemp3/100
ir4x {dom=value.dom, vr=0.00:500.00:0.01} := xtemp4/100
setgrf ir*.mpr mtsatjp.grf
del xtemp*.* -force

//Export the MTSAT images into Arc/INFO ASCII format
export ArcInfoNAS(ir1x.mpr,ir1x)
export ArcInfoNAS(ir2x.mpr,ir2x)
export ArcInfoNAS(ir3x.mpr,ir3x)
export ArcInfoNAS(ir4x.mpr,ir4x)

//calculating the cloud height map (using code in Appendix 1)
!cloudhgt1 'ir1x.asc' 'ir2x.asc'

//convert the MTSAT images from ASCII format (row and column) into XYZ format
//(using code in Appendix 2)
!ir2xyz
//convert the cloud height image from ASCII format (row and column) into XYZ format
!elev2xyz

//conducting parallax correction of MTSAT images using code in Appendix 3
!MTSAT1Rcor

//Import the corrected MTSAT image from text table format into ILWIS table format
ircor.tbt:=table(ircor.dat,Space,Convert,none,X(value.dom),Y(value.dom),Z1(value.dom),Z2(v
alue.dom),Z3(value.dom),Z4(value.dom))

//creating point map of the corrected MTSAT from the imported table
ir1cor.mpp:=PointMapFromTable(ircor,mtsatjp,Z1)
ir2cor.mpp:=PointMapFromTable(ircor,mtsatjp,Z2)
ir3cor.mpp:=PointMapFromTable(ircor,mtsatjp,Z3)
ir4cor.mpp:=PointMapFromTable(ircor,mtsatjp,Z4)

//point to raster conversion of MTSAT corrected image
tempo1.mpr{dom=value;vr=::0.01} := MapRasterizePoint(ir1cor,mtsat12sec.grf,1)
setvr tempo1.mpr value 180.00:400.00:0.01 -force
ir1cor.mpr{dom=value;vr=::0.01} := MapAggregateMin(tempo1,10,group)
tempo2.mpr {dom=value;vr=::0.01}:= MapRasterizePoint(ir2cor,mtsat12sec.grf,1)
setvr tempo2.mpr value 180.00:400.00:0.01 -force
ir2cor.mpr{dom=value;vr=::0.01} := MapAggregateMin(tempo2,10,group)
tempo3.mpr{dom=value;vr=::0.01} := MapRasterizePoint(ir3cor,mtsat12sec.grf,1)
setvr tempo3.mpr value 180.00:400.00:0.01 -force
ir3cor.mpr{dom=value;vr=::0.01} := MapAggregateMin(tempo3,10,group)
tempo4.mpr {dom=value;vr=::0.01}:= MapRasterizePoint(ir4cor,mtsat12sec.grf,1)
setvr tempo4.mpr value 180.00:400.00:0.01 -force
ir4cor.mpr{dom=value;vr=::0.01} := MapAggregateMin(tempo4,10,group)
setgrf ir*.mpr mtsatjp.grf -force
del tempo1.* -force
del tempo2.* -force
del tempo3.* -force
del tempo4.* -force

//---------------------------cloud classification----------------------------------------
// IR slicing
ir1_cls.mpr{dom=cls_IR1.dom} = MapSlicing(ir1cor,cls_IR1.dom)
```

```
btd12:=ir1cor-ir2cor

//BTD slicing
btd_cls.mpr{dom=cls_BTD12.dom} = MapSlicing(btd12,cls_BTD12.dom)

//cloud detection
delta:=max_jja_smoth - ir1cor
cloudy_land:=iff((landsea=1) and (delta > 20),1,?)
cloudy_sea:=iff((landsea=0) and (delta >7),1,?)
cloudy := iff((cloudy_land =1) or (cloudy_sea = 1), 1,?)

//joining IR and BTD using 2D crossing table
xtemp4 :=clsMTSAT[btd_cls,ir1_cls]
xtemp5.mpr{dom=cloud_cls}:=ifundef(xtemp4,"7: Clear")
cloud_cls_cor.mpr{dom=cloud_cls}:=iff(cloudy=1,xtemp5,"7: Clear")
del xtemp*.* -force
del cloudy_land.* -force
del cloudy_sea.* -force

//copy the results from process folder into the corresponding result folder
copy ir1cor.mpr c:\MTSATrainest062010\ircor\ir1cor2010062206.mpr
copy ir1cor.mp# c:\MTSATrainest062010\ircor\ir1cor2010062206.mp#
copy ir2cor.mpr c:\MTSATrainest062010\ircor\ir2cor2010062206.mpr
copy ir2cor.mp# c:\MTSATrainest062010\ircor\ir2cor2010062206.mp#
copy ir3cor.mpr c:\MTSATrainest062010\ircor\ir3cor2010062206.mpr
copy ir3cor.mp# c:\MTSATrainest062010\ircor\ir3cor2010062206.mp#
copy ir4cor.mpr c:\MTSATrainest062010\ircor\ir4cor2010062206.mpr
copy ir4cor.mp# c:\MTSATrainest062010\ircor\ir4cor2010062206.mp#
copy cloud_cls_cor.mpr c:\MTSATrainest062010\cloudclass\cls2010062206.mpr
copy cloud_cls_cor.mp# c:\MTSATrainest062010\cloudclass\cls2010062206.mp#
```

**Appendix 5.** Program source code for picking up grid value of binary map (e.g. an output map from MATSIRO simulation) and saving the result in a text file.

Compiler: FOTRAN95

```
program read_binary_data
      implicit none
c     to pick up grid values from binary maps in certain row and column
c     prepared by: Dwi Prabowo YS
c     ************************************

      integer :: status, ierror, access
      integer :: col,row, row1, readrow1, readcol1
      integer,parameter :: maxcol=265
      integer,parameter :: maxrow=219
      real :: data1(maxcol, maxrow)
      real :: data2(maxcol, maxrow)
      real :: datain, dataout
      character :: ifilename*80
      character :: readcol*80
      character :: readrow*80
c
      call getarg(1,ifilename)
      call getarg(2,readcol)
      call getarg(3,readrow)
      open(unit=7, file=ifilename,access='direct',recl=maxcol*4)
      open(unit=8, file='extvalue.txt', access='append', iostat=ierror)
      row1=maxrow
      readloop: do row=1,maxrow
        read(7,rec=row) (data1(col,row),col=1,maxcol)
      enddo readloop
c
      row1=maxrow
      do row=1,maxrow
        do col=1,maxcol
        datain = data1(col,row)
        call native_4byte_real(datain,dataout)
        data2(col,row1) = dataout
c        write(6,*) data2(col,row1)
        enddo
        row1=row1-1
      enddo
      read (readcol,*) readcol1
      read (readrow,*) readrow1
      write(*,*) data2(readcol1,readrow1)
      write(8,*) data2(readcol1,readrow1)
      end program read_binary_data

      !subroutine for converting byte order from big endian to
      !little endian and vice versa (from: www.cgd.ucar.edu/cas/software/endian.html)
      subroutine native_4byte_real( realIn, realOut )
      IMPLICIT NONE
      REAL, INTENT(IN)       :: realIn
      ! a single 32 bit, 4 byte
      ! REAL data element
      REAL, INTENT(OUT)                            :: realOut
      ! a single 32 bit, 4 byte
      ! REAL data element, with
      ! reverse byte order to
      ! that of realIn
      ! Local variables (generic 32 bit INTEGER spaces):
      INTEGER                                      :: i_element
      INTEGER                                      :: i_element_br
      ! Transfer 32 bits of realIn to generic 32 bit INTEGER space:
      i_element = TRANSFER( realIn, 0 )
      ! Reverse order of 4 bytes in 32 bit INTEGER space:
      CALL MVBITS( i_element, 24, 8, i_element_br, 0  )
      CALL MVBITS( i_element, 16, 8, i_element_br, 8  )
      CALL MVBITS( i_element,  8, 8, i_element_br, 16 )
      CALL MVBITS( i_element,  0, 8, i_element_br, 24 )
      ! Transfer reversed order bytes to 32 bit REAL space (realOut):
      realOut = TRANSFER( i_element_br, 0.0 )
      return
      END subroutine
```

**Appendix 6.** The URL of free data and tools used in the study.

## Satellite images

| Name of Satellite images | URL |
|---|---|
| MTSAT | From IIS/Tokyo University: http://webgms.iis.u-tokyo.ac.jp/IIS/4KM/index.php<br>From Kochi University: http://weather.is.kochi-u.ac.jp/archive-e.html |
| TRMM 2A12 | http://mirador.gsfc.nasa.gov/cgi-bin/mirador/presentNavigation.pl?tree=project&dataset=2A12%20%28Version%20007%29:%20Hydrometeor%20Profile%20%28TMI%29&project=TRMM&dataGroup=Orbital&version=007 |
| TRMM 3B42 | http://mirador.gsfc.nasa.gov/cgi-bin/mirador/presentNavigation.pl?tree=project&dataset=3B42:%203-Hour%200.25%20x%200.25%20degree%20merged%20TRMM%20and%20other%20satellite%20estimates&project=TRMM&dataGroup=Gridded&version=007 |
| MODIS products | https://lpdaac.usgs.gov/products/modis_data_products_table |
| CERES products | http://ceres.larc.nasa.gov/compare_products.php |
| SRTM DEM (about 90m) | https://lta.cr.usgs.gov/SRTM2 |
| ASTER DEM (about 30m) | http://gdem.ersdac.jspacesystems.or.jp/ |

## Ancillary spatial data

| Name of spatial data | URL |
|---|---|
| FAO Digital soil map of the world | http://www.fao.org/geonetwork/srv/en/metadata.show?id=14116 |
| JMA numerical weather analysis | http://database.rish.kyoto-u.ac.jp/arch/jmadata/data/gpv/original |
| National land numerical information download service (soil type, geology, land use, coast line, river network, etc) | http://nlftp.mlit.go.jp/ksj-e/jpgis/jpgis_datalist.html |

## Hydro-meteorological data

| Name of Hydro-meteorological data | URL |
|---|---|
| MLIT rainfall and discharge data | www1.river.go.jp |

## Some free tools for data analysis

| Name of tool | Functionality | URL |
|---|---|---|
| ILWIS | Remote sensing digital image processing and GIS | www.ilwis.org<br>ILWIS source code can be accessed from:<br>http://52north.org/communities/ilwis |
| HEGTool | Windows/Linux based for converting HDF into GIS data formats | http://newsroom.gsfc.nasa.gov/sdptoolkit/HEG/HEGDownload.html |
| OrbitView | Displaying and converting TRMM data into GIS format | http://disc.sci.gsfc.nasa.gov/TRMM/additional/precipitation/additional/tools/trmm_ov.shtml<br>Japanese version:<br>http://www.astroarts.co.jp/products/orbitviewer/ |
| MYSTAT | Statistical analysis software (free version available for student) | http://www.systat.com/MystatProducts.aspx |
| FreeBASIC | Free Windows/Linux based BASIC programming compiler | http://www.freebasic.net/ |
| Force | Windows based FORTRAN77/90 integrated development environment | http://lepsch.blogspot.jp/ |
| Parallax correction (FORTRAN sub routine) | To perform geostationary image parallax correction base on Vicente et. al. (2002) procedure | ftp://ftp.eumetsat.int/pub/MET/out/marianne/parallax_tables/parallax.f90 |
| Regional Frequency Analysis (FORTRAN source code) | To perform regional frequency analysis of extreme event based on Hosking and Wallis (1997) procedure | http://lib.stat.cmu.edu/general/lmoments<br>documentation of the program:<br>http://lib.stat.cmu.edu/general/lmoments.pdf |

Note: Due to transient nature of URL the link may be changing in the future.

# CURRICULUM VITAE

Home address: Indonesia
Current address: Hokkaido University International House Kita 8, Kita 8, Nishi 11, 1-4-101, Sapporo

Name: Dwi Prabowo Yuga Suseno
Date of birth: 04/11/1975

Educational background

| | |
|---|---|
| 01/07/1993 | Senior High School, Kebumen, Central Java, Indonesia (graduated). |
| 01/08/1993 | Department of Cartography and Remote Sensing, Faculty of Geography, Gadjah Mada University, Yogyakarta, Indonesia (enrolled). |
| 31/08/1998 | -same as above- (graduated). |
| 01/08/2007 | Master's Program (double degree), Geoinformation for Spatial Planning and Risk Management, Gadjah Mada University, Yogyakarta, Indonesia and International Institute for Geoinformation Science and Earth Observation (ITC), Enschede, The Netherlands (enrolled). |
| 29/04/2009 | -same as above- (graduated). |
| 01/10/2010 | Doctoral Program, Division of Field Engineering for Environment, Graduate School of Engineering, Hokkaido University (enrolled). |
| 25/09/2013 | -same as above- (graduated). |

Professional background

| | |
|---|---|
| 01/09/1998 | Forest Fire Prevention Management Project, Japan International Corporation Agency (JICA), Bogor, Indonesia (joined). |
| 01/09/1998 | Early Warning System Expert Assistant, same as above (assigned). |
| 31/08/1999 | –same as above– (resigned). |
| 01/09/1999 | Forest Watch Indonesia, Bogor, Indonesia (joined). |
| 01/09/1999 | Remote Sensing and Geographic Information System (GIS) specialist, same as above (assigned). |
| 26/12/2001 | –same as above– (resigned). |
| 27/12/2001 | Watershed management office of Indragiri-Rokan, Ministry of Forestry Republic of Indonesia, Pekanbaru, Riau, Indonesia (joined). |
| 27/12/2001 | Government officer staff (assigned until now). |

Research background

01/08/2007～ 29/04/2009

Geoinformation for Spatial Planning and Risk Management,Gadjah Mada University, Yogyakarta, Indonesia and International Institute for Geoinformation Science and Earth Observation (ITC),"Geostationary satellite based rainfall estimation for hazard studies and validation, A case study of Java Island, Indonesia" involved in during Master's program.

01/10/2010～ present

Division of Field Engineering for Environment, Graduate School of Engineering, Hokkaido University, " The use geostationary satellite based rainfall estimation and rainfall-runoff modelling for regional flash flood assessment" involved in during Doctoral program.

Prize

I certify that the above are true records.

Date: 19/6/2013

(Dwi Prabowo Yuga Suseno)

# LIST OF PUBLICATIONS

Dissertation submitted for the degree

I. Title: The use geostationary satellite based rainfall estimation and rainfall-runoff modelling for regional flash flood assessment.

Peer reviewed papers:

1. Suseno, Dwi Prabowo Yuga, T. J. Yamada, 2011, Geostationary Satellite Based Rainfall Estimation and Validation: A Case Study of Java Island, Indonesia, Journal of Japan Society of Civil Engineers, Ser. B1 (Hydraulic Engineering), Volume 67, Issue 4, pp. I_43-I_48
2. Suseno, Dwi Prabowo Yuga, T. J. Yamada, 2011, The Use of Cloud Type Classification To Improve Geostationary Based Rainfall Estimation. 9th International Symposium on Southeast Asian Water Environment, Dec 1st - 3rd 2011 Bangkok City, Thailand.
3. Suseno, Dwi Prabowo Yuga, T. J. Yamada, 2012, The use of geostationary based rainfall estimation for characterizing strom severity, Journal of Japan Society of Civil Engineers, Ser. B1 (Hydraulic Engineering), Volume 68, Issue 4, pp. I_175-I_180
4. Suseno, Dwi Prabowo Yuga, T. J. Yamada, 2012, Two-dimensional threshold-based cloud-type classification using MTSAT data, Remote Sensing Letters, Vol. 3, No. 8, pp. 737 - 746
5. Suseno, Dwi Prabowo Yuga, T. J. Yamada, 2013, The role of GPS precipitable water vapor and atmospheric stability index on the statistically-based rainfall estimation using MTSAT data, Submitted to Journal of Hydrometeorology (accepted).

Oral presentation on conference:

1. Suseno, Dwi Prabowo Yuga, T. J. Yamada, 2011,Geostationary satellite based rainfall estimation and validation and its future development, The 67th Japan Society of Civil Engineers Local Conference, Feb 2011, Tomakomai, Japan.
2. Suseno, Dwi Prabowo Yuga, T. J. Yamada, 2011, Characterizing storm severity by using geostationary satellite rainfall, Proceedings of 2011 Annual conference, Japan Society of Hydrology and Water Resources, Aug 30th - Sep 1st , 2011, Kyoto, Japan
3. Suseno, Dwi Prabowo Yuga, T. J. Yamada, 2013, The Use of MTSAT and atmospheric environmental condition datasets for storm rainfall estimation. The 1st International Doctoral Symposium in Structural and Hydraulic Engineering, Feb 7th -9th 2013, Sapporo, Japan.

Poster Presentation:

1. Suseno, Dwi Prabowo Yuga, T. J. Yamada, 2011, The Use of Cloud Type Classification To Improve Geostationary Satellite Based Rainfall Estimation, Japan Geoscience Union Meeting 2011, Tokyo, Japan.
2. Suseno, Dwi Prabowo Yuga, T. J. Yamada, 2012, Flash flood severity assessment using Hydro-morpho-climatic approach, Hokkaido University and Chungbuk National University Joint Symposium, Sapporo, Japan.

Co-author for peer reviewed papers:

1. Wada, Takuya, T. J. Yamada, Dwi Prabowo Yuga Suseno, 2012, Formation and environment of a line-shaped rainfall system observed in Niigata-Fukushima Heavy Rainfall in July 2011 (in Japanese), Journal of Japan Society of Civil Engineers, Ser. B1 (Hydraulic Engineering), Volume 68, Issue 4, pp. I_397-I_402
2. Yamato, Watanabe, T. J. Yamada, Dwi Prabowo Yuga Suseno, 2013, The Cloud Climatology Over Southeastern Asian Regions By Using MTSAT Cloud Classification (in Japanese), Journal of Japan Society of Civil Engineers, Ser. B1 (Hydraulic Engineering), Volume 69, Issue 4, pp. I_301-I_306